MARMARA UNIVERSITY
INSTITUTE FOR GRADUATE STUDIES
IN PURE AND APPLIED SCIENCES

MEASUREMENT OF GLUON JET CROSS SECTION IN CMS DETECTOR IN PROTON-PROTON COLLISIONS AT $\sqrt{s} = 13$ TeV

İSMAİL OKAN ATAKİŞİ

Ph.D. THESIS
Department of Physics

Thesis Supervisor
Prof. Dr. Mithat KAYA

İSTANBUL, 2023

MARMARA UNIVERSITY
INSTITUTE FOR GRADUATE STUDIES IN PURE AND APPLIED SCIENCES

MEASUREMENT OF GLUON JET CROSS SECTION IN CMS DETECTOR IN PROTON-PROTON COLLISIONS AT $\sqrt{s} = 13$ TeV

İSMAİL OKAN ATAKİŞİ

Ph.D. THESIS

Department of Physics

Thesis Supervisor

Prof. Dr. Mithat KAYA

İSTANBUL, 2023

PREFACE

Words may not be enough to express my gratitude to my supervisor Prof. Dr. Mithat KAYA for his guidance and confidence in me. His grasp of information and his management of situations will always serve as models for me. I'm also grateful to Prof. Dr. Mikko VOUTILAINEN for his endless knowledge of jet physics. To be able to collaborate with him at CERN, HIP, and remotely made me feel fortunate. Additionally, I feel grateful to my thesis committee members Prof. Dr. Erhan GÜLMEZ and Prof. Dr. Özgür DELİCE for their patience and constructive feedback.

I should also extend my gratitude to Dr. Sevgi TEKTEN, a close friend of mine, for her tolerance when working with me during challenging times. Also, I would like to express my special thanks to colleges at CMS in the JME DQM group for their advice, and mates at Marmara University for their moral support.

Lastly, I want to thank my family for always being there for me and for sharing my belief that science and education are the foundations of progress.

Finally, I would like to recognize the financial support of Marmara University BAPKO (Project No:10229.) and Helsinki Institute of Physics (Project: Measurement of inclusive gluon jet cross section with 2017 data), TENMAK (Project No: 2018TAEK(CERN)A5.H6.F2-18).

CONTENTS

PREFACE i

ÖZET v

ABSTRACT vi

CLAIM FOR ORIGINALITY vii

ABBREVIATIONS viii

LIST OF FIGURES xi

LIST OF TABLES xiii

1. INTRODUCTION 1

2. THEORY 3

2.1. The Standard Model 3

2.2. Quantum Chromodynamic QCD 5

2.3. Perturbative Quantum Chromodynamics (pQCD) 6

2.3.1. Asymptotic Freedom 6

2.4. Factorization, Parton Distribution Function and Cross Section 8

3. EXPERIMENTAL SETUP 10

3.1. The LHC Accelerator 10

3.1.1. Luminosity 11

3.2. The CMS Detector 13

3.2.1. Coordinate System of the CMS Detector 15

3.2.2. Tracker System 16

3.2.3. Electromagnetic Calorimeter 17

3.2.4. Hadronic Calorimeter 19

3.2.5. The Superconducting Solenoid Magnet 21

3.2.6. The Muon System 22

3.2.7. The Trigger System 23

3.2.8. The Particle Flow Algorithm 24

4. MATERIAL AND METHOD 27

4.1. Quark Gluon Jet Discrimination 27

4.1.1. Particle Multiplicity 28

4.1.2. Transverse Minor Axis σ_2 28

4.1.3. Momentum Fragmentation Function $p_T D$ 28

5. ANALYSIS 30

5.1. Datasets and Simulations 30

5.2. Event Selection 30

5.2.1. Trigger Selection and Luminosity 30

5.2.2. Jet Energy Correction 33

5.2.3. Pile-up Weight Correction 33

5.2.4. Correction for Detector Effects 35

5.2.4.1. Hotzone and Coldzone Map 35

5.2.4.2. ECAL Prefire 36

5.3. Particle Flow-PF Jet Reconstruction 37

5.4. QGL and Quark Gluon Jet Distributions 38

5.4.1. Quark Gluon Likelihood 39

5.4.2. Quark Gluon Template and Scale Factors 40

5.4.3. Quark Gluon Jet Fractions 42

5.5. Monte Carlo Comparisons 44

5.5.1. Jet Response of Quarks Gluons Unknown Jets 47

5.6. Unfolding 48

5.7. Cross-Section Calculation 55

5.8. Systematic Uncertainties 56

6. CONCLUSIONS 60

7. REFERENCES 61

8. APPENDIX 64

8.1 Multiplicity Distributions both for MC and Data 64

8.2 Minor Axis 2 Distributions both for MC and Data 67

8.3 p_TD Distributions both for MC and Data 70

8.4 QGL Distributions both for MC and Data 73

8.5 Template Fit both for MC and Data 76

8.6. Template Fit with Uncertainties 79

ÖZET

Jetler, yüksek enerjili proton-proton çarpışmalarında üretilen kuarkların ve gluonların fiziksel tezahürüdür ve LHC'de ölçülen en yaygın fizik nesneleri arasındadır ayrıca jetlerin üretimi ve karmaşık evrimi, proton parton dağılım fonksiyonları (PDF'ler), güçlü çiftlenim sabiti (α_s) ve Kuantum Renk Dinamiği (KRD) kuralları tarafından yönetilir. Yine de genellikle pertürbatif QCD kullanılarak nicel olarak anlaşılabilirler ve PDF'ler ve α_s'ler hakkında bilgi edinmek için kullanılabilirler. Bununla birlikte birçok fizik olayında elde edilmek istenen jetler gluonlar tarafından perdelenmektedir. Kuark ve gluon jetlerinin şekilleri ve özellikleri birbirinden farklı olduğundan dolayı CMS'de kullanılan ihtimal tabanlı ayrım (likelihood based discriminant QGL) metodu ile jetlerin kökenine ilişkin istatistik dahilinde bir bilgi edinmek mümkündür. Bu analiz kapsamında, CMS'de Run2 (2016) boyunca 13 TeV enerjide toplam ışınlılık değeri 36.3 fb^{-1} olan veriler kullanılarak anti-k_T algoritması ile kümelendirilmiş R=0.4 koni yarıçaplı jetler için ölçümler yapılmıştır. Sonrasında QGL metodu kullanılarak olay üreteçlerinin içindeki özlük bilgileri yardımıyla kuark ve gluon kaynaklı jetler ayırt edilip ölçüm verilerini olay üreteçleri seviyesine taşıyarak istatistik hata payları dahilinde kapsamlı gluon jet tesir kesiti ölçümü yapılmıştır.

Anahtar Kelimeler: LHC, CMS, gluon, jet, kuark, QGL, tesir kesiti, 13 TeV, KRD

ABSTRACT

Jets are the physical manifestation of quarks and gluons produced in high-energy proton-proton collisions and are among the most common physics objects measured at the LHC, as well as the generation and complex evolution of jets, proton parton distribution functions (PDFs), strong coupling constant (α_s), and Quantum Chromodynamics (QCD). It is governed by rules. However, they can usually be understood quantitatively using perturbative QCD and can be used to learn about PDFs and α_s. However, the jets desired to be obtained in many physical events are screened by gluons. Since the shapes and properties of quark and gluon jets are different from each other, it is possible to obtain statistical information on the origin of jets with the likelihood-based discriminant Quark-Gluon Likelihood (QGL) method used in CMS. Within the scope of this analysis, inclusive jet measurements were carried out for R=0.4 cone radius jets with the anti-kT algorithm using the data with an integrated luminosity of 36.3 fb^{-1} at 13 TeV energy during Run2 (2016) in CMS. Afterward, using the QGL method, quark gluon-sourced jets were distinguished with the help of the intrinsic information in the event generators, and the measurement data was carried out to the level of the event generators. Then, a comprehensive gluon jet cross-section measurement was made within the statistical error margins.

Keywords: LHC, CMS, gluon, jet, quark, QGL, cross section, 13 TeV

CLAIM FOR ORIGINALITY

In this thesis, the data obtained from 13TeV proton-proton collisions produced by LHC and the gluon jets in the inclusive jets are distinguished using the QGL method, and the cross-section results of the inclusive gluon jets within the unfolding calculations are presented for the first time.

ABBREVIATIONS

ALICE : A Large Ion Collider Experiment

ATLAS : A Toroidal LHC ApparatuS

CHF : Charge Hadron Fraction

CMS : Compact Muon Solenoid

CMSSW : Compact Muon Solenoid Soft Ware

CSC : Cathode Strip Chambers

DT : Drift Tubes

ECAL : Electromagnetic Calorimeter

EM : Electromagnetic

E_{miss} : Missing Energy

E_T : Transverse Energy

EWT : ElectroWeak Theory

GeV : Giga Electron Volt

HCAL : Hadronic Calorimeter

HE : Hadronic Endcap

HF : Hadronic Forward

HLT : High Level Trigger

HO : Hadronic Outer

IP : Interaction Point

JEC : Jet Energy Calibration

JER : Jet Energy Resolution

Jet ID : Jet Identification

L1 : Level-1 trigger

LHC : Large Hadron Collider

LHCb : Large Hadron Collider beauty

LO : Leading Order

MC : Monte Carlo

NEF : Neutral Electromagnetic Fraction

NHF : Neutral Hadron Fraction

NLO : Next to Leading Order

NNLO : Next-Next to Leading Order

NP: NonPerturbative

PbWO4 : Lead Tungstate

PDF : Parton Distribution Function

PFJets : Particle Flow Jets

PU : Pile Up

PMT : Photo Multiplier Tube

pQCD : perturbative Quantum Chromo Dynamics

PV : Primary Vertex

QCD : Quantum Chromo Dynamics

QED : Quantum Electro Dynamic

RMS : Root Mean Square

RPC : Resistive Plate Chambers

SCs : Super Crystals

SM : Standard Model

SVD : Singular Value Decomposition

LIST OF FIGURES

Figure 2. 1. The standard model of elementary particles 4
Figure 2. 2. One loop Feynman diagram 7
Figure 2. 3. Illustration of the contribution of parton i of the first proton to parton j of the second proton to the scattering of high p_T A(ij→ab). 8
Figure 2.4. Some QCD Feynman diagrams for q→gq 9
Figure 3.1. The LHC project planning until 2036 10
Figure 3.2. For the pp collisions, peak luminosity in relation to time for the years 2010–2012 and 2015–2018 12
Figure 3.3. The LHC with four main detectors, together with pre-accelerators 13
Figure 3.4. A cutaway view of the CMS detector 14
Figure 3.5. CMS and LHC, coordinate systems on cylindrical detector 16
Figure 3.6. A sketch of one fourth of the tracker in r-z plane 17
Figure 3.7. An endcap PbWO4 crystal and VPT 18
Figure 3.8. Sketch of the ECAL barrel, endcap and preshower regions represented in the longitudinal plane 18
Figure 3.9. Layout of a quadrant of the CMS HCAL in an y z plane. 19
Figure 3.10. Schematic of HB wedges on left, HE wedges on right. 20
Figure 3.11. Artistic view of the solenoid 21
Figure 3.12. Schematic of the CMS quadrant for with colored muon sub-detectors. 22
Figure 3.13. The Trigger System of CMS 23
Figure 3.14. Representation of PF particle objects inside cross-section of CMS 24
Figure 4.1. The jet observables used in quark gluon separation are particle multiplicity, σ_2 and p_TD, respectively 29
Figure 5.1. Trigger turn on curves for HLT60, HLT140, HLT260, HLT450 31
Figure 5.2. CMS jet calibration chart 33
Figure 5.3. Pile up distributions 34
Figure 5.4. Hotzones both for 2016 data and MC 35
Figure 5.5. Coldzones maps both for 2016 data and MC 35
Figure 5.6. ECAL Prefire Map both for 2016 data and MC 37
Figure 5.7. PF Energy distribution histogram for the CMS Barrel region 38

Figure 5.8. QGL distrubutions of jets in the barrel of the CMS for selected p_T bins 40
Figure-5.9. Quark gluon probability distributions for triggers 200, 260, 320, 400 41
Figure 5.10. Quark gluon fraction distributions for jet p_T corresponding triggers 42
Figure 5.11. Quark and gluon jet fraction distrubutions for each jet p_T 43
Figure 5.12. Gluon distributions for Pythia and Herwig 44
Figure 5.13. Gluon flavor fractions without unknown jets for Pythia and Herwig 45
Figure 5.14. Jet flavor distributions, Pythia on the left, MadGraph on the right 46
Figure 5.15. Jet flavor distributions, multijet Pythia, dijet Pythia 46
Figure 5.16. Jet flavor distributions, multijet Pythia, dijet Pythia 47
Figure 5.17. Response plot of quark, gluon and inclusive jets 48
Figure 5.18. Quark and Gluon fractions 49
Figure 5.19. Quark and gluon jet response histogram normalized to inclusive jet measurement 50
Figure 5.20. Response matrices 51
Figure 5.21. Unfolding correction factors 53
Figure 5.22. Quark gluon jet ratio histograms for MC only 54
Figure 5.23. Corrected quark gluon jet fraction histograms and for DATA/MC. 55
Figure 5.24. Total gluon cross section for the barrel region and jet cross sections up to $|y|< 2.0$ 56
Figure 5.25. Template Fit with Systematic Uncertainties 57
Figure 5.26. Total uncertainties for the cross section of the inclusive jets 58

LIST OF TABLES

Table 2.1. Fundamental Forces 4

Table 5.1. Effective luminosity and turn-on values of triggers 32

1. INTRODUCTION

We now have a more developed and formed understanding of our universe thanks to investigations into the nature of matter at higher energies. The ultimate objective of particle physics is to comprehend the fundamental components of matter and their interactions.

The Standard Model (SM) of particle physics accurately explains nearly all of the experimental findings to date and describes the fundamental particles as well as the fundamental forces. The European Organization for Nuclear Research's (CERN) Large Hadron Collider (LHC) provides an opportunity to look for unique events outside of the Standard Model and to deliver answers to the basics of our universe. The four major detectors at the LHC, including CMS, are built to find particles created in hadronic collisions and provide us the ability to measure the cross sections of elementary processes in the new energy range. High-precision experimental measurements and precise theory computations are necessary for the clear interpretation of the results from the LHC experiments. In particular, searches for proof of novel states or fundamentally novel interactions outside the boundaries of the Standard Model call for such high precision.

The 1960s had seen the beginning of research into protons' internal environment. Parton Distribution Functions have been developed as a result of systematic research in experiments like SLAC and ZEUS, and they currently provide an understanding for the internal structure of the proton. PDFs are defined from Strong Interactions by the rules of Quantum Chromodynamics (QCD) under the Standard Model. Although it is possible to define the particles inside protons and their interactions using PDFs, the quarks and gluons that make up these particles cannot be seen as free particles because of a phenomenon known as color confinement. As a result, it is theoretically possible to narrate the relationship between gluons and quarks to the results of perturbative QCD calculations at low energies. In addition, new physics studies investigating unique events are screened by Gluon jets. Therefore, the fact that the LHC can produce a high amount of jets paves the way for these boundary tests to be carried out with the jet measurements to be made in the CMS.

In this thesis, the 36.3 fb^{-1} integrated luminosity, 2016 data, which result from proton-proton collisions at $\sqrt{s} = 13$ TeV energy, has been used to measure the inclusive cross-section of gluon jets from p + p → jet + X.

This dissertation is structured as follows: In THEORY, the SM is introduced, paying particular attention to the QCD and jets in the LHC. Additionally, the non-perturbative models and MC event generators employed in the analyses are shown and explained. The LHC accelerator and the CMS detector's component parts are described in EXPERIMENTAL SETUP. The MATERIAL AND METHOD explain the role of jet variables in quark-gluon differentiation as well as CMS's approach to carrying out this task.

Three QCD investigations are shown in ANALYSIS, along with a breakdown of the process's phases. The measurements of the inclusive gluon jet cross section at $\sqrt{s}$ = 13 TeV for the findings are ultimately compiled and put to rest in the n CONCLUSIONS section.

2. THEORY

High energy physics, or particle physics, is a branch of physics that studies subatomic particles and their interactions. With the high energy physics experiments carried out until the 1970s, the nature of the interactions of the particles was explained and the theoretical model created was called the Standard Model (SM). In this section, the basics of SM are explained, and the tools and software used are presented.

2.1. The Standard Model

The Standard Model, created from the results obtained from experimental data, classifieds elementary particles into two groups: bosons and fermions. Bosons are particles with integer spin, and fermions are particles with half-integer spin. While quarks and leptons have half-integer spin, quarks also have color charges. An examination of the elementary particle table reveals that there are three families of fermions, and the particle properties of each generation behave like the previous generation. The first family of fermions is the lowest mass, stable elementary particles that make up the daily substances of the universe. The up (u) and down quark (d), electron (e) and electron neutrino (ν_e) are members of this first family. First family followed by charm (c) and strange quark (s), muon (μ) and muon neutrino (ν_μ) are called second family, similarly top (t) and bottom quark (b), tau (τ) and tau neutrino (ν_τ) form the third family.

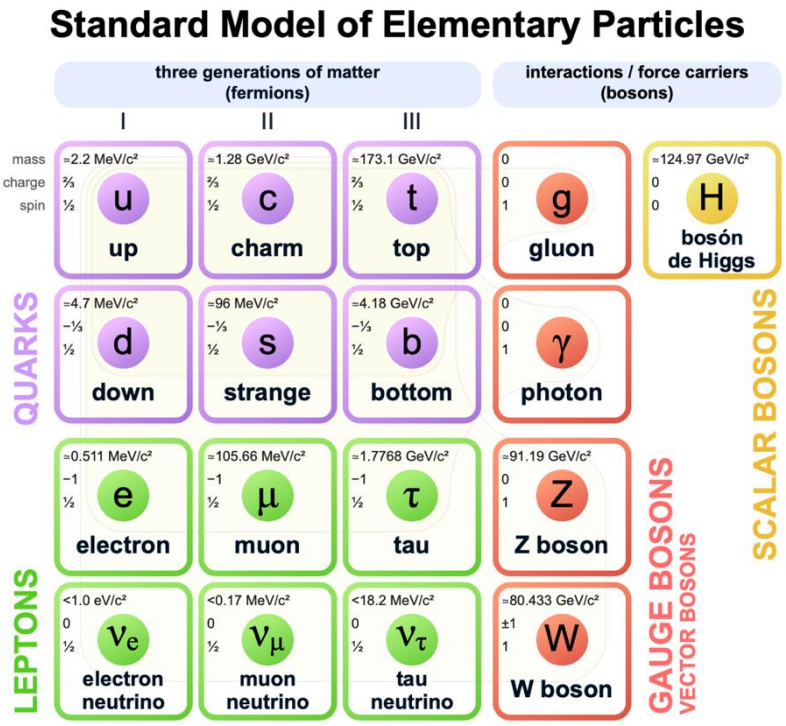


Figure 2. 1. The standard model of elementary particles [1]

Bosons, on the other hand, are force carrier particles with integer spin in accordance with the nature of the interactions that are defined by the change of fields of quantized fundamental forces. In Table 2.1, fundamental forces, carrier particles, namely bosons, and the theoretical framework including them are given.

Table 2.1. Fundamental Forces.

Force	**Force Carrier Particle**	**Theory**	**Strength**
Strong	gluon	Chromodynamic	1
Electromagnetism	photon	Electrodynamic	10^{-1}
Weak	$W^{\pm}$, Z^{0}	Electroweak	10^{-7}
Gravity	graviton	General relativity	10^{-39}

The strong force is the force that holds the particles formed by the quarks together, and its carrier particle is the gluon. The electromagnetic force is the force that holds the electrons around the nucleus, and the carrier particle is the photon. The weak force is

responsible for radioactive decay and is carried by W and Z bosons. Finally, the gravitational force is given in the table, but it cannot be explained with the standard model framework yet [2].

2.2. Quantum Chromodynamic

QCD is an important part of the SM, it is a gauge field theory with a gluon as a mediator, which describes interactions between quarks with the dynamics of color charges.

Lagrangian for QCD is given with

$$\mathcal{L} = \sum \bar{\psi}_{q,a} \left(i\gamma^{\mu} \partial_{\mu} \delta_{ab} - g_s \gamma^{\mu} t^{C}_{ab} A^{C}_{\mu} - m_q \delta_{ab} \right) \psi_{q,b} \frac{1}{4} F^{A}_{\mu\nu} F^{A\mu\nu} \tag{2.1}$$

Where $\bar{\psi}_{q,a}$ are quark field spinors for mass m_q, q is a variant of quark. γ^{μ} are Dirac gamma matrices. Index a represents the three-color charges from quarks and ranges from 1 to $N_c = 3$. A^{C}_{μ}, represents the gluon field and C varies from 1 to $N_C^2 - 1 = 8$ which means that there are 8 kinds of gluons. t^{C}_{ab} represents eight 3 × 3 matrices and the constituents of the SU (3) group. t_{ab} is the field tensor of A and is given by the group SU (3). g_s is a QCD coupling constant. $F^{A}_{\mu\nu}$ is the tensor field and is given as below:

$$F^{A}_{\mu\nu} = \partial_{\mu} A^{A}_{\nu} - \partial_{\nu} A^{A}_{\mu} - g_s f_{ABC} A^{B}_{\mu} A^{C}_{\upsilon} \tag{2.2}$$

Here f_{ABC} are the structure constants of the group SU (3). A B C transcends the eight color degrees of freedom of the gluon field. The third non-Abelian term on the right distinguishes QCD from QED. t is the matrix in the basic and combined representations of the group SU (3):

$$[t^{A}, t^{B}] = i f_{ABC} t^{C} \tag{2.3}$$

t^{A}, provided by eight Gell-Mann matrices that are hermitian and traceless,

$$t^{A} = \frac{1}{2} \lambda^{A} \tag{2.4}$$

$$\lambda^1 = \begin{pmatrix} 0 & 1 & 0 \\ 1 & 0 & 0 \\ 0 & 0 & 0 \end{pmatrix}, \quad \lambda^2 = \begin{pmatrix} 0 & -i & 0 \\ i & 0 & 0 \\ 0 & 0 & 0 \end{pmatrix}, \quad \lambda^3 = \begin{pmatrix} 1 & 0 & 0 \\ 0 & -1 & 0 \\ 0 & 0 & 0 \end{pmatrix},$$

$$\lambda^4 = \begin{pmatrix} 0 & 0 & 1 \\ 0 & 0 & 0 \\ 1 & 0 & 0 \end{pmatrix}, \quad \lambda^5 = \begin{pmatrix} 0 & 0 & i \\ 0 & 0 & 0 \\ i & 0 & 0 \end{pmatrix}, \quad \lambda^6 = \begin{pmatrix} 0 & 0 & 0 \\ 0 & 0 & 1 \\ 0 & 1 & 0 \end{pmatrix},$$

$$\lambda^7 = \begin{pmatrix} 0 & 0 & 0 \\ 0 & 0 & -i \\ 0 & i & 0 \end{pmatrix}, \quad \lambda^8 = \frac{1}{\sqrt{3}} \begin{pmatrix} 1 & 0 & 0 \\ 0 & 1 & 0 \\ 0 & 0 & -2 \end{pmatrix},$$

The normalization of SU (N) matrices is chosen as:

$$Tr\ t^a t^b = T_R \delta^{AB}, T_R = 1/2 \tag{2.5}$$

With this selection, the color matrices obey the following equations:

$$C_F = 4/3, C_A = 3 \tag{2.6}$$

C_F and C_A are called color factors. C_A defines the relative probability of a gluon pairing with another gluon, while C_F defines the probability of pairing with a quark. The C_F/C_A ratio, along with the strong coupling constant α_s, is one of the most fundamental quantities in QCD [3].

Due to the complex nature of QCD calculations, many techniques are studied and Perturbative QCD is one of them.

2.3. Perturbative Quantum Chromodynamics (pQCD)

pQCD is defined in the region where high momentum $|Q^2|$ transfers occur, quarks and/or gluons are very close to each other, and the force in between particles is weak.

2.3.1. Asymptotic Freedom

Scientists studying the strong interactions, David J. Gross, H. David Politzer and Frank Wilczek discovered that, during the interpretation of their mathematical results, the closer the quarks come to each other, the lower the color charge, and therefore the weaker the force, that is, the particles behave almost freely [4]. This phenomenon is called "asymptotic freedom".

The coupling constant, α_s, which determines the strength of the force for strong interaction is given by:

$$Q^2 \frac{\partial \alpha_s}{\partial Q^2} = \beta(\alpha_S) \tag{2.7}$$

where, α_s is given by the β function, since gluon and/or quark anti-quarks can pair with themselves in vacuum and is defined as follows:

$$\beta(\alpha_S) = -b\alpha_S^2\left(1 + b'\alpha_S + b''\alpha_S^2 + b'''\alpha_S^3 + O(\alpha_S^4)\right) \tag{2.8}$$

For one loop Feynman diagram,

$$b = \frac{(11C_A - 2n_{lf})}{12\pi} = \frac{(33 - 2n_{lf})}{12\pi} \tag{2.9}$$

It is given as the coefficient of one loop function β. n_{lf} is the number of active light flavors and the coefficients b′, b″, b‴ are also known. Since the beta function is negative, $\alpha_s \to 0$ for the $Q^2 \to \infty$ case.

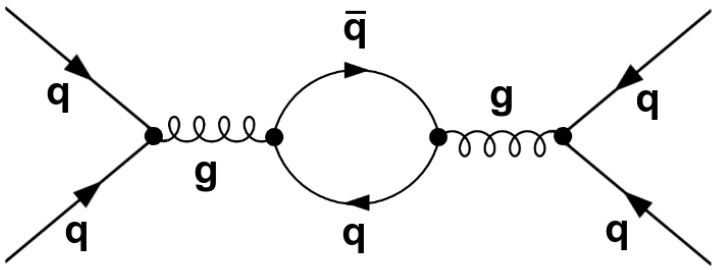


Figure 2. 2. One loop Feynman diagram

The lowest level approximation of the above equation for the relevant coupling constant is given as follows:

$$\alpha_S(Q^2) = \frac{1}{bln\left(\frac{Q^2}{\Lambda^2}\right)} \tag{2.10}$$

where Λ is the energy multiplier that makes α_S infinite. Experimentally, this value is about 300 MeV. In case of $Q^2 \simeq \Lambda$, the coupling constant becomes larger and pQCD becomes inoperable [5-9].

2.4. Factorization, Parton Distribution Function and Cross Section

Factorization is a key feature of QCD such that it divides cross-section calculations into two. Short distance partonic cross section calculations that can be done with pQCD and Long-distance calculations which can be removed from partonic calculations and converted to parton distribution functions. With this approach, the partons inside the colliding hadrons are represented by the parton distribution functions, that is, the PDFs with the $f_{i/h}(x,\mu_f)$ function. These functions give the probability of finding the parton i in the hadron h defined by the factorization scale μ_f with longitudinal momentum x.

The cross section for proton-proton collisions is defined as follows:

$$d\sigma_{(pp\to X)} = \sum_{i,j} \int dx dx' f_{i/p}(x,\mu_f) \cdot f_{j/p}(x',\mu_f) \times d\hat{\sigma}_{(ij\to X)}(x,x',\mu_f,\mu_r,\alpha_s(\mu_r)) \tag{2.11}$$

where i is the initial state of the j th parton flavor and their corresponding $f_{i/p}$, $f_{j/p}$ are proton PDFs with partial momentum x, x', respectively. The total includes the cross sections $i,j \in \{q, \bar{q}, g\}$ of all initial flavors. Its pictorial representation is given in Figure 2.3 below.

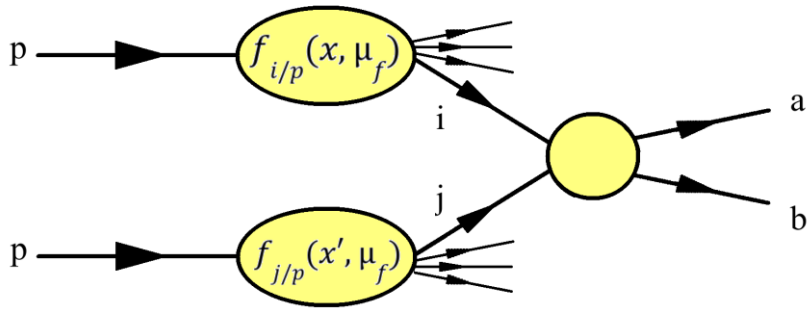


Figure 2. 3. Illustration of the contribution of parton i of the first proton to parton j of the second proton to the scattering of high p_T A(ij→ab).

According to the asymptotic degree of freedom, the desired cross section can be expanded to the power series for the relevant Q. The solution with the first term of the power series

is conventionally called Leading Order (LO). As the contributions of the subsequent terms are added, the degree of solution increases, and the naming is changed by prefixing the LO with the prefix (Next), such as NLO- NNLO [6-10].

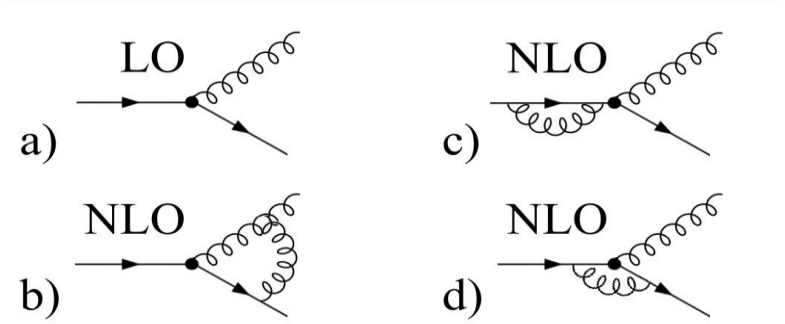


Figure 2.4. Some QCD Feynman diagrams for q→gq

3. EXPERIMENTAL SETUP

3.1. The LHC Accelerator

The Large Hadron Collider (LHC) is hosted by the CERN (Conseil Européen pour la Recherche Nucléaire), in Switzerland, it is the largest and most powerful hadron collider for particle physics research ever built. The LHC is built in the tunnel of the predecessor's accelerator of CERN, the Large Electron Positron Collider (LEP) that was constructed in 1984-1989. The LHC project has been started operation in 2008.

The LHC plans to enhance the center of mass energy up to 14TeV to understand the standard model and beyond the standard model. Figure 3.1 shows in detail the planned timeline undergoes various upgrades for the LHC to reach this enormous energy. In the Figure 3.1 blue and green areas indicate shutdown/technical stop (LS means Long Shutdown) and data acquisition phases respectively [11].

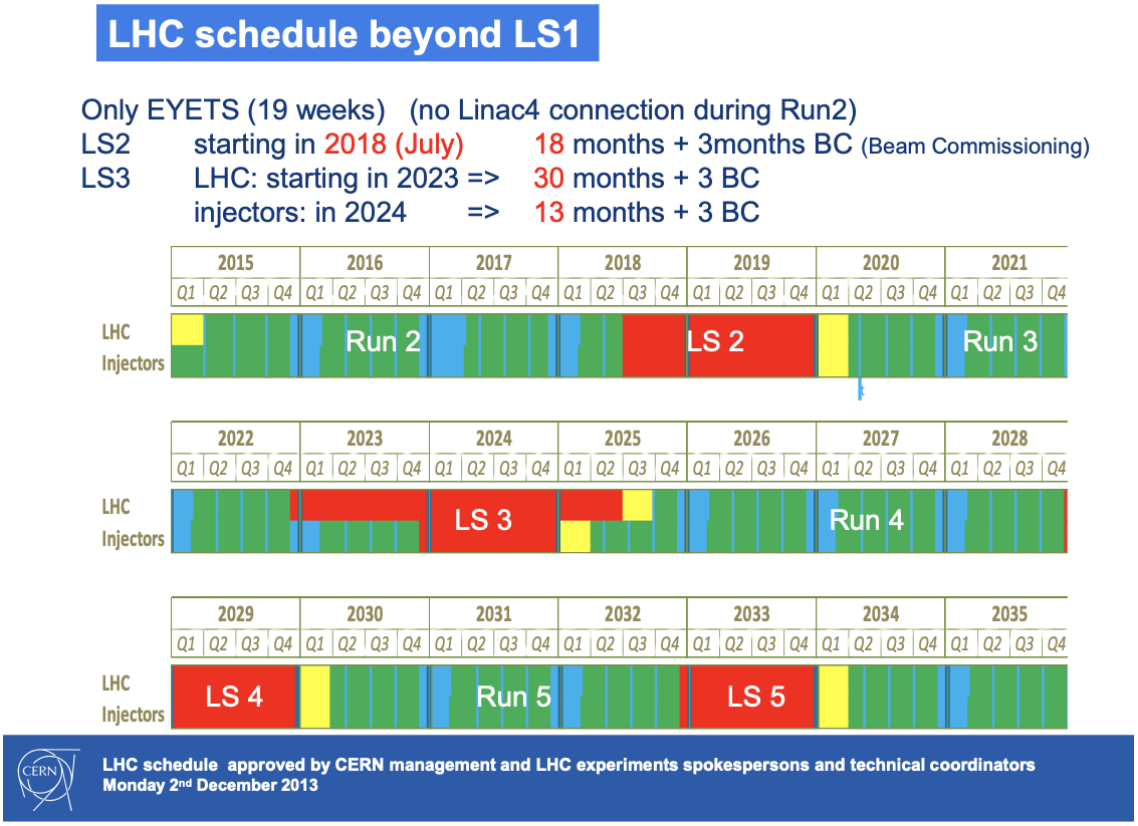


Figure 3.1. The LHC project planning until 2036 [12]

3.1.1. Luminosity

The luminosity is one of the key indicators of the probability of the particles colliding by the accelerator. It varies in proportion to how many collisions take place in a given period of time. Once we have higher luminosity, one needs to understand that the experiment is collected more data so that rare events can be found. The luminosity of the accelerator is given:

$$L = \frac{N_{event}}{\sigma_{event}} \tag{3.1}$$

For a given cross section (σ_{event}), N_{event} in the formula corresponds to the number of events for each second. Additionally, luminosity can be defined with a Gaussian beam distribution and depends on the beam parameters.

$$L = \frac{N_b^2 n_b f_{rev} \gamma_r}{4\pi \varepsilon_n \beta^*} \; F \tag{3.2}$$

In the given formula above, f_{rev}, γ_r, ε_n, and β^* correspond to the revolution frequency, the relativistic gamma factor, the normalized transverse beam emittance, and the beta function at the collision point, respectively. Moreover, the geometric luminosity reduction owing to the crossing angle at the interaction point, the number of particles per bunch, and the number of bunches for each beam, are denoted by the letters F, N_b, and n_b, respectively.

The LHC is designed to reach peak luminosity of 10^{34} $cm^{-2}s^{-1}$. The goal has already been achieved and even surpassed in 2017. Figure 3.2 indicates the peak luminosity values recorded by the CMS detector included from 2010 to 2022 data-taking periods.

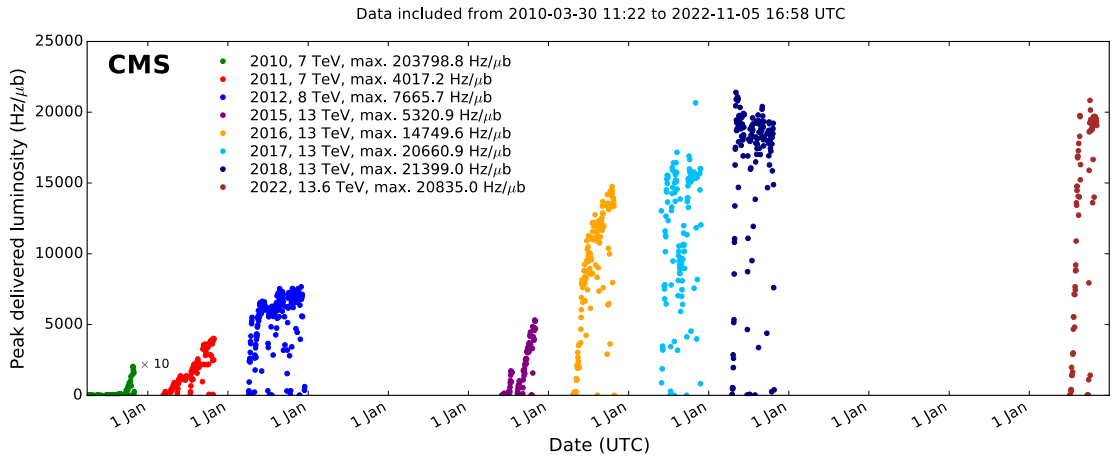


Figure 3.2. For the pp collisions, peak luminosity in relation to time for the years 2010–2012 and 2015–2018 [13].

Various experiments make use of the high luminosity data generated by the LHC. The general-purpose experiments ATLAS [14] and CMS [15] are designed to investigate processes both for the beyond Standard Model (SM) and the SM. TOTEM [16] and LHCB [17] are experiments using low luminosity data, focusing on forward physics and B-physics, respectively. Although the CMS and ATLAS can study heavy-ion collisions, ALICE [18] experiment is specifically designed for it. From the Figure 3.3, one can see the LHC and CERN's accelerator complex.

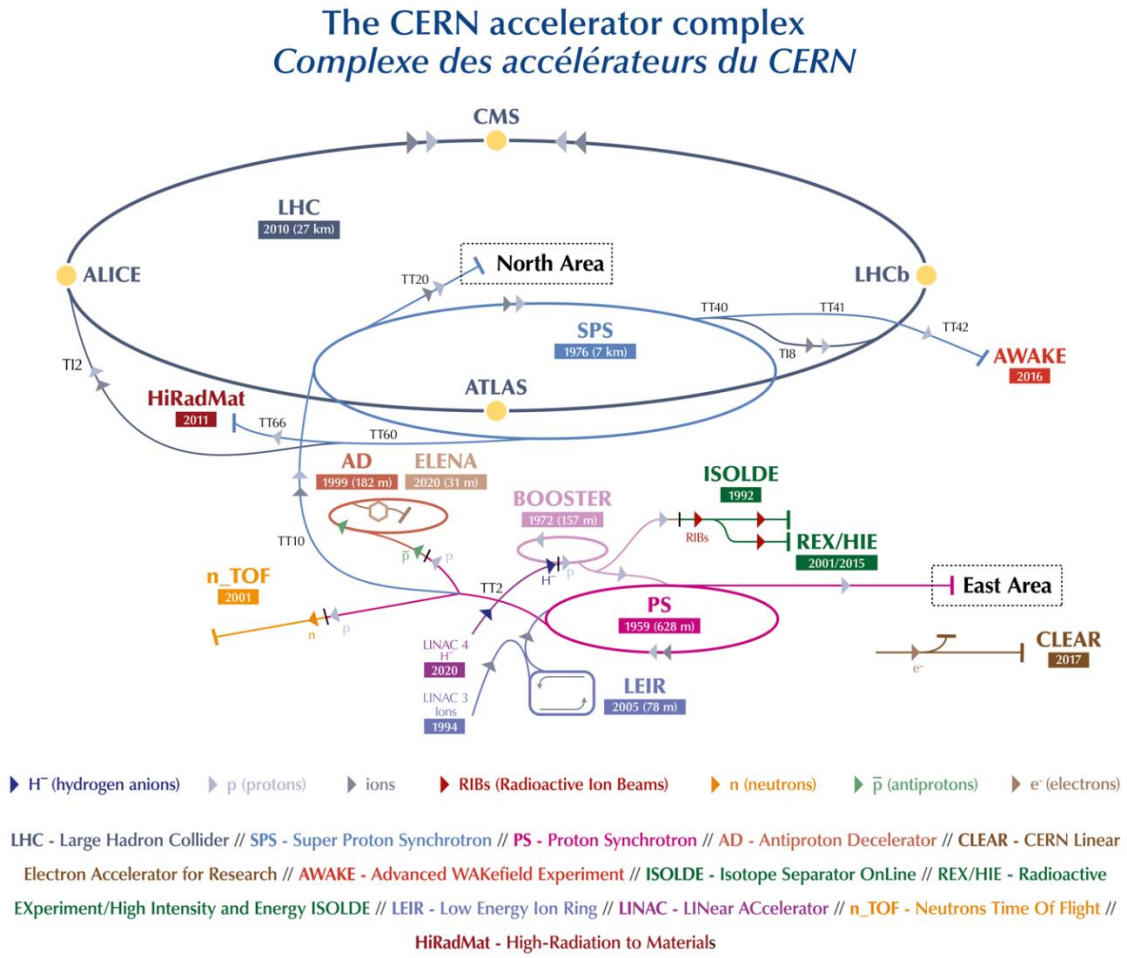


Figure 3.3. The LHC with four main detectors, together with pre-accelerators [19]

As seen in Figure 3.3, protons and heavy ions are accelerated through various stages before being injected into the LHC. Firstly, by applying an electric field to the hydrogen atoms, by removing the electrons, protons are obtained and then accelerated by LINAC to 50 MeV. Then with the help of BOOSTER, Proton Synchrotron (PS), and Super Proton Synchrotron (SPS), respectively, protons or heavy ions are accelerated up to 450 GeV. Finally, they are injected into the LHC where they can have a maximum energy of 7 TeV. Although all stages up to this point are the same for protons and heavy ions, heavy ions, as a first step, go through Linac 3 and then Low Energy Ion Ring (LEIR) accelerators.

3.2. The CMS Detector

The Compact Muon Solenoid (CMS) is a general-purpose detector designed to observe new physics phenomena that the LHC may reveal. There is an analogy where the CMS is a camera that can take a snapshot of collision up to 40 millionths of a second, which is often used and is true. Although this analogy is correct, in reality, the CMS collects

information about the momentum, energy, and physical properties of the stable particles that result from the collision so that the "physical" snapshot in the analogy can be formed.

As can be seen from Figure 3.3, there are four main interaction points on the LHC where collision data is collected. The CMS is located at the interaction point called IP-5 which is 100 meters below the ground.

In general, if the structure of the CMS is examined, it is seen that it weighs 12,500 tons and is 21.6 meters long and 14.6 meters in diameter. Moreover, CMS is not monolithic but consists of cylindrical layers making technical interventions relatively trouble-free.

Apart from these structural specifications, another important aspect of the CMS detector is its layout. One indispensable part of a general-purpose detector is a magnet. The superconducting solenoid magnet in the CMS can create a magnetic field of 3.8T. While there is the muon system outside of the solenoid magnet, there are Electromagnetic Calorimeters (ECAL), Hadron Calorimeters (HCAL), and trackers inside. Also, each system is composed of a barrel and two endcap sections. A cutaway view of the CMS detector and its sub detectors are shown in Figure 3.4.

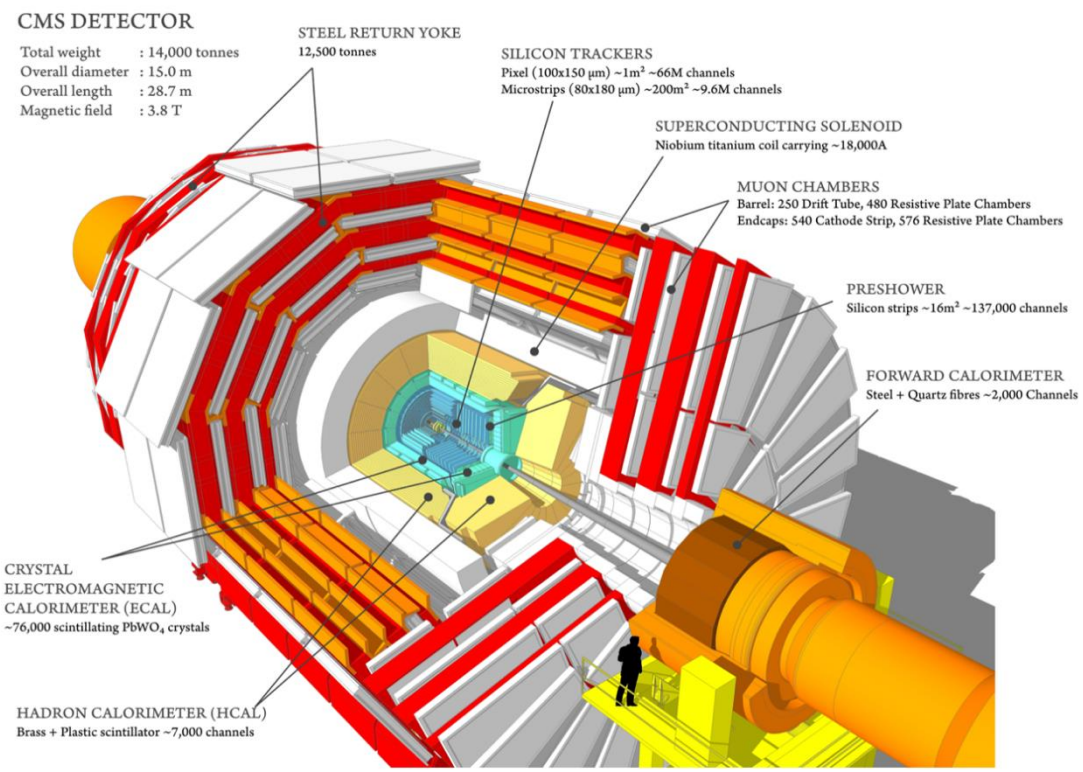


Figure 3.4. A cutaway view of the CMS detector [20]

3.2.1. Coordinate System of the CMS Detector

It is unimaginable for a detector like CMS to be without a coordinate system. The position of the particles formed as a result of the collision should be determined so that the physics emerging from the collision can be understood.

The CMS detector has a cylindrical structure located around the collision point so that the collisions coincide with the middle of the CMS. Therefore, it is possible to describe the CMS detector with the cartesian or cylindrical coordinate systems where this collision point is the origin. The explanations and components of these coordinate systems are given below, and their representation can be found in Figure 3.5.

Cartesian coordinates:

- The x-axis is horizontal and points towards the center of the LHC.
- The y-axis is vertical and points to the sky.
- The z-axis is horizontal and points along the beam direction toward the Jura mountains.

The expression of the transverse plane, which is often used in the analysis, is the x-y plane and perpendicular to the beam direction. Variables measured in this plane are represented with subscript T and help us to constrain the net momentum of the final state particles.

Cylindrical coordinates:

- r is the radial distance to the beamline.
- φ is the azimuthal angle in the x/y-plane. It points to the +x axis when $\varphi = 0$, and the +y axis when $\varphi = \pi/2$.
- θ is the polar angle and defined with respect to the z-axis. It points to the +z direction when $\theta = 0$, and the -z direction when $\theta = \pi$.

One physically important coordinate definition is pseudorapidity η. It is defined via the polar angle θ as $\eta = -\ln(\tan(\theta/2))$ and used to physically define the angular position of the particles.

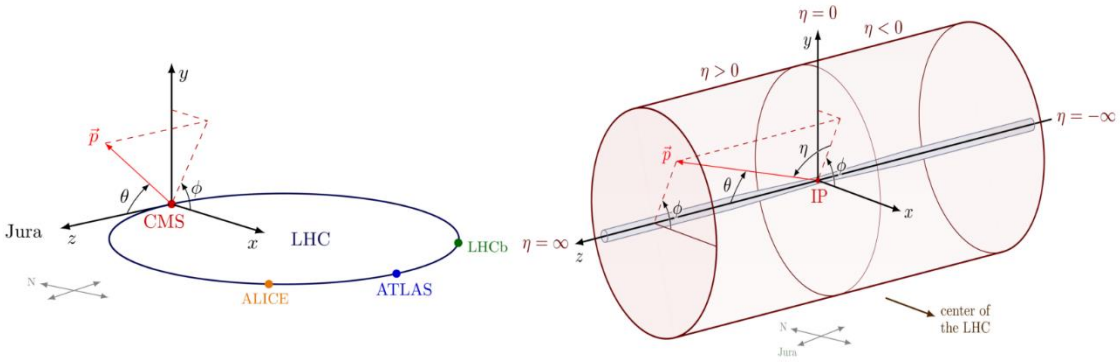


Figure 3.5. CMS and LHC (left), coordinate systems on cylindrical detector (right) [15]

3.2.2. Tracker System

The tracking system is the first sub-detector of the multilayer CMS detector close to the collision points given in Figure 3.4. Since the tracker is very close to the interaction point (IP) and the $10^{34}\,cm^{-2}\,s^{-1}$ designed luminosity of the LHC is very high, measuring charged particles with transverse momentum greater than 1 GeV is challenging. When the path of a particle traveling through a magnetic field is traced, the momentum of that particle is also determined. The CMS tracker system, for each bunch crossing which means for every 25 ns, saves these paths by measuring locations of the particles at several points in high resolution for such challenging conditions where 1000 charged particles can be found.

The CMS tracking system composed of inner pixel detectors and outer strip detectors, covering the range up to absolute pseudorapidity 2.5. The tracker system must withstand high luminosity as well as radiation damage due to very close to IP. The necessities of read-out speed, radiation hardness, and granularity have pushed the inner tracking system on silicon detector technology.

It is possible to describe the inner pixel tracker into two parts: Barrel Pixel (BPIX) and Forward Pixel (FPIX) which covers Endcap. With this configuration, three tracking points are covered for the given pseudorapidity range. Up until this point pixel detector covers radial region from 4.4 to 15 cm.

The strip tracker has three main segments, the Tracker Inner Barrel (TIB) and Disks (TID), the Tracker Outer Barrel (TOB), and the Tracker Endcaps (TEC). With this configuration radial region from 25.5 to 113.5 cm are covered for given pseudorapidity.

Overall, the tracker system of the CMS, whose segments are given above, consists of 1440 silicon pixel detectors and 15148 strip detectors, one-fourth of which can be seen in Figure 3.6 [21-22].

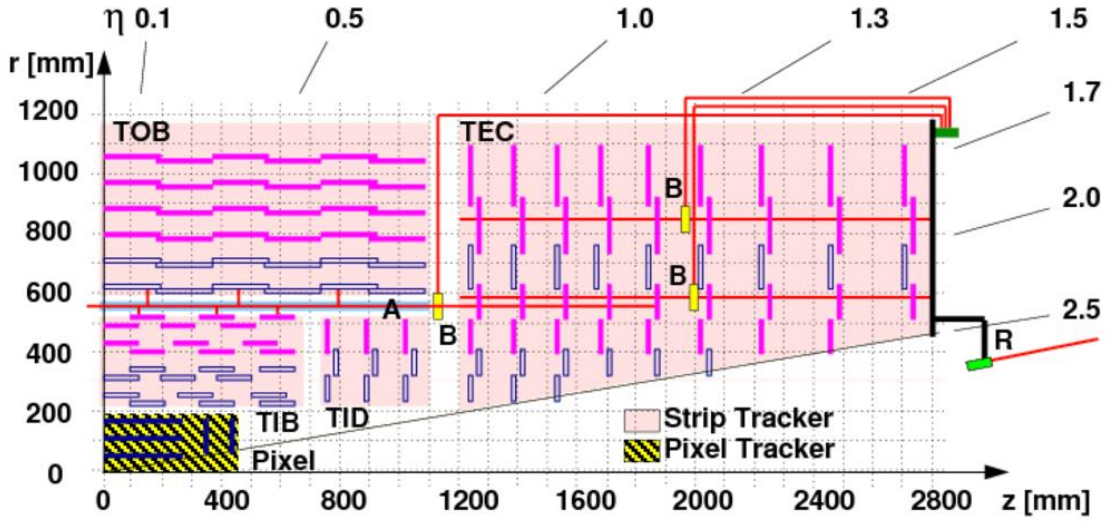


Figure 3.6. A sketch of one fourth of the tracker in r-z plane [22].

3.2.3. Electromagnetic Calorimeter

As the name suggests, the Electromagnetic Calorimeter (ECAL) is intended to measure final electromagnetic particles such as photons, positrons, and electrons emerging from collisions [23]. ECAL is a vital sub-detector for Higgs, SM, and beyond SM studies [24]. As a matter of fact, the final products of the $H \rightarrow \gamma\gamma$ and $H \rightarrow ZZ$ channels, which provided the best mass resolution of the Higgs Boson discovery, which was first announced in 2012, were measured via ECAL [25].

The ECAL calorimeter covering the tracker system like an onion layer consists of lead tungstate ($PbWO_4$) crystals and photomultipliers that are sensitive to the light formed inside the crystals. The crystals are rectangular prisms that are tapered in shape and paired with avalanche photodiodes (APDs) for the barrel region covering $|\eta| < 1.479$, while vacuum phototriodes (VPTs) are paired for the Endcap region covering $1.479 < |\eta| < 3.0$.

These sections are referred to as ECAL Barrel (EB) and ECAL Endcap (EE), respectively.

Lead tungstate crystals are a transparent material that can scintillate within 25 ns once particles pass through it and are heavier than stainless steel due to the lead inside.

Considering all these features together with their ability to resist high radiation, it is clear why they are used in ECAL calorimetry. An exemplary ECAL crystal and its coupled photomultiplier can be seen in Figure 3.7.

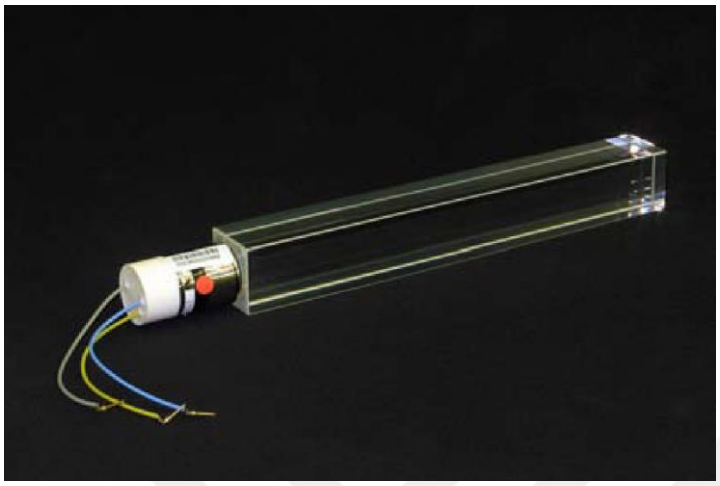


Figure 3.7. An endcap PbWO4 crystal and VPT

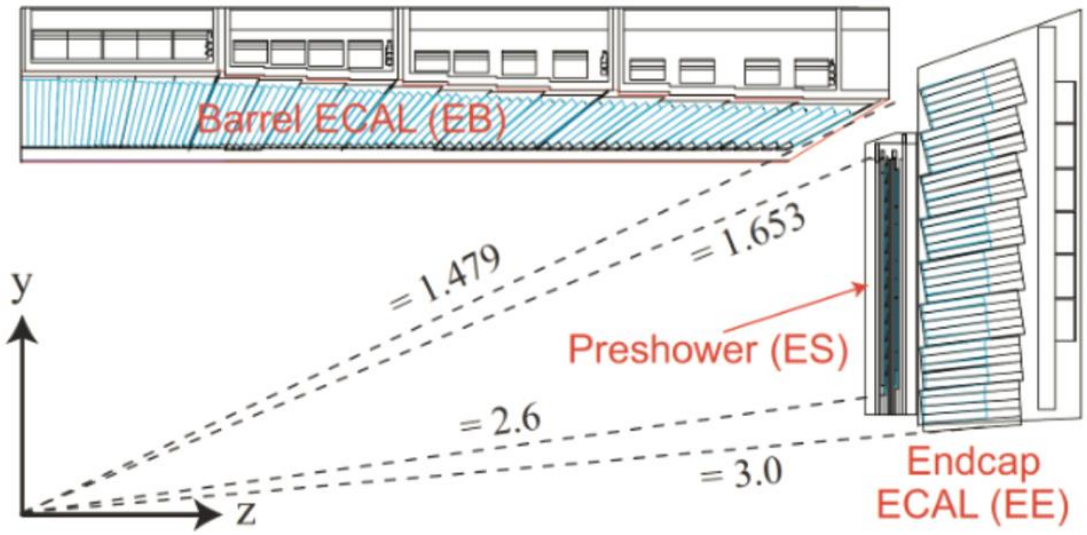


Figure 3.8. Sketch of the ECAL barrel, endcap and preshower regions represented in the longitudinal plane

When Figure 3.8, which shows the geometric configuration of ECAL, is examined, it is possible to see the preshower (ES) detector standing right in front of the EE located between rapidity 1.653 and 2.6, as well as the EB consisting of 61200 crystals and the EE consisting of 7324 crystals.

Low energy photon pairs arising from π^0 and high energy photons indicating intriguing physics need to be differentiated. For that purpose, the preshower detector (ES) is designed to provide extra precision to the endcap region with the help of its lead layers, and it also helps to differentiate electron and minimum ionizing particles. The preshower detector, which is geometrically composed of two layers, consists of a thin lead layer facing the IP and a silicon strip sensor placed behind them, and the thickness is 20 cm [24].

3.2.4. Hadronic Calorimeter

The hadronic calorimeter (HCAL) is one of the indispensable subsystems of CMS detector design, specifically designed for jet studies, and it is capable of measuring the energy and directions of particle jets, helping to differentiate quarks and gluons. Furthermore, it is possible to calculate missing transverse energy (MET) with the help of particle jets, which is crucial in exotic particle searches. Therefore, it plays a crucial role in SM and beyond SM studies carried out at CMS.

The Hadronic calorimeter, enclosing ECAL, is a large structure consisting of Hadron Outer (HO) and Hadron Barrel (HB) for $|\eta| < 1.3$ regions, Hadron Endcap (HE) for $1.3 < |\eta| < 3$ regions, and Hadron Forward (HF) for $3 < |\eta| < 5$ forward regions. Overall lay out of the hadronic calorimeter in CMS can be seen in Figure 3.9 [26].

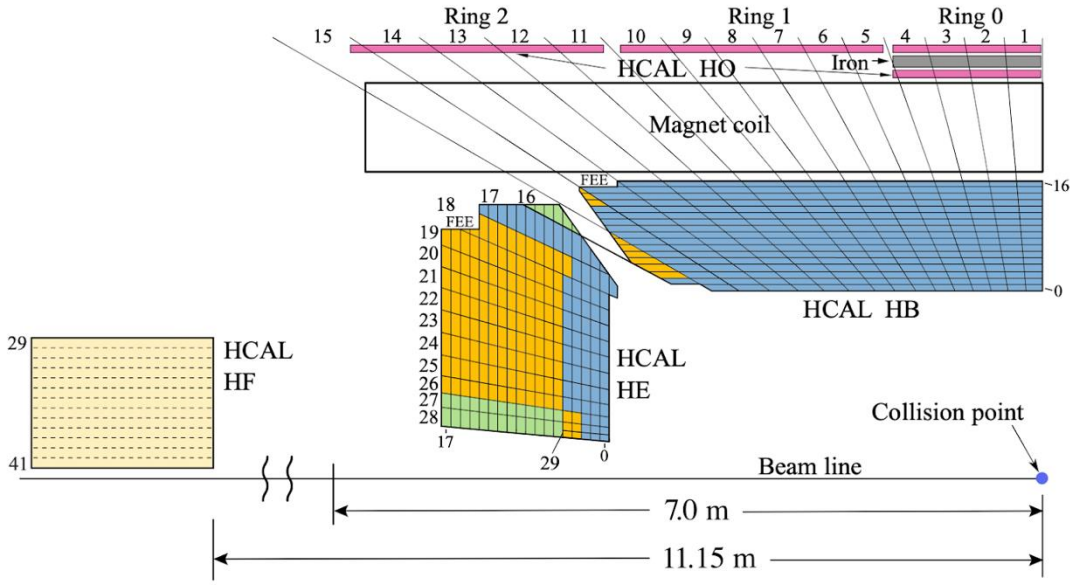


Figure 3.9. Layout of a quadrant of the CMS HCAL in an y z plane.

HB and HE located inside the solenoid magnet consist of thick Bicron BC408, Kuraray SCSN81 plastic scintillators, hybrid photodiodes, wavelength shifters (WLS) placed in grooves on scintillators, and mostly brass absorbers which are non-magnetic. Here absorbers increase the chance of hadronization, scintillators produce lights in response to hadronized particles, WLSs carry those lights to hybrid photodiodes, and finally, photodiodes turn photons into signals.

Geometrically, the HB is a barrel combined from two half barrels known as HB+ and HB-. Each half barrel consists of 18 wedges. HE is designed to be a cap for both ends of the HB. Each cap consists of 36 wedges designed to insert mega-tiles. Schematics of wedges are shown in Figure 3.10. for both HB and HE.

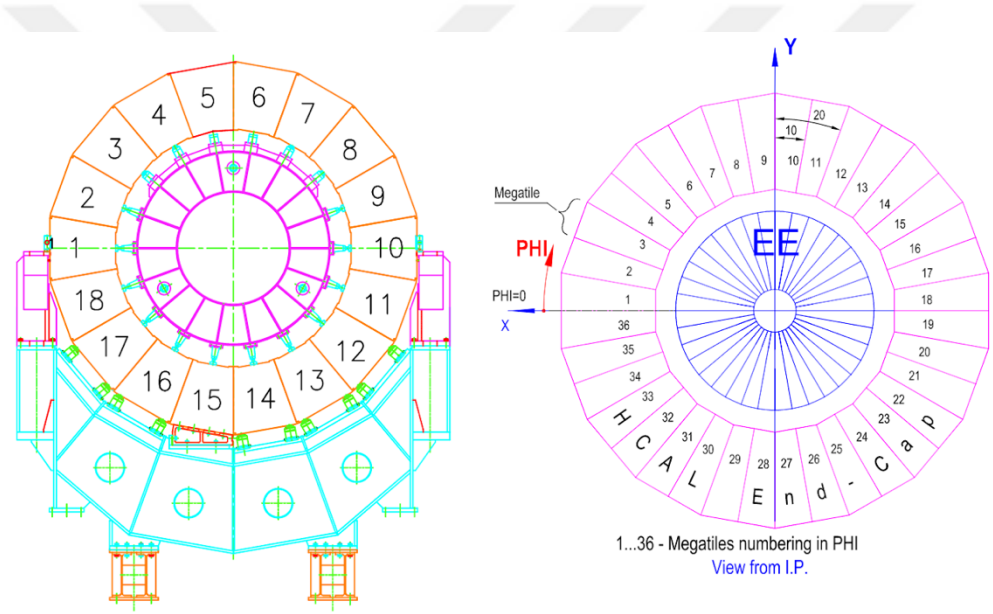


Figure 3.10. Schematic of HB wedges on left, HE wedges on right.

Another sub-calorimeter of the HCAL, in the barrel region, is HO which is placed outside of the magnet. This calorimeter prevents hadronic particles from reaching muon systems which is why it is known as a tail catcher. HO is segmented into 5 rings in η which correspond to muon rings of the muon system for given η coverage.

The Forward Calorimeter (HF) is essentially different from all the above-mentioned calorimeters due to its structure. The first thing to remember is that due to the rapidity coverage of HF, there is no electromagnetic calorimeter in front of it. This requires the HF to have a design in which it can measure both electromagnetic particles and hadronic particles. Furthermore, HF needs to stand the severe radiation conditions.

Due to the requirements described above, stainless steels were used as absorbers in the passive region, and radiation-resistant quartz fibers were used as light collection in the active region. There are two cylindrical geometry of HF detectors, HF- and HF+, that consists of 18 wedges. Each wedge has long and short quartz fibers embedded in the layers. These quartz fibers carry the Cherenkov radiation formed inside them to the photomultipliers behind the detectors once particles interact with calorimetry. Moreover, with the help of these short and long fibers, electrons/photons and hadrons can be distinguished from each other [27].

3.2.5. The Superconducting Solenoid Magnet

A magnetic field is essential in energy measurements of particles emerging from collisions. The magnetic field, created along the same axis as the proton bunches circulated by the LHC, deflects the particles formed as a result of the collision of the proton bunches and causes them to move along a curved path. The more energetic the particle, the smaller the arc is created, and vice versa.

The Superconducting Solenoid Magnet is constructed to enclose the HCAL surrounding ECAL in the CMS experiment. It is a single magnet with dimensions of 6 m in diameter and 12.5 m in length that generates a magnetic field within and outside the magnet for precision measurements. Moreover, the magnet can generate a homogeneous 4 T magnetic field at 2.6 GJ full current in the tracker system. Artistic view of the solenoid can be seen from Figure 3.11 [28].

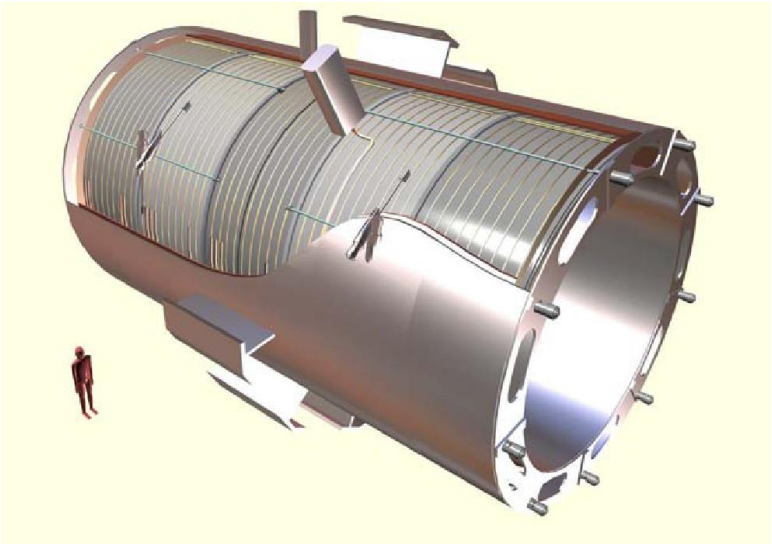


Figure 3.11. Artistic view of the solenoid

3.2.6. The Muon System

The LHC creates high background where physicists are interested in rare phenomena like the Higgs measurements. So, the Muon system is expected to be good so that the H → ZZ and ZZ* channels, where the end products are leptons, can be probed. It is well-known that muons can penetrate more material than electrons, and one can interpret that with a well-designed muon system, muons can provide better resolution for the Higgs analysis given above.

In total, there are 3 different detector types used in the CMS muon system and their positions are shown in the Figure 3.12. below. These are drift tubes (DTs) used in barrel region (|η| <1.2) only, resistive plate chambers (RPCs) used in endcap and barrel region (|η| <1.6), and cathode strip chambers (CSCs) used in endcap region (1.2< |η| <2.4) only.

A muon is measured by fitting a curve to the points detected by the 4 muon layers outside the CMS magnet. Thanks to the magnetic field, this curved path that the muon follows gives the momentum information of that muon. However, when the muon momentum gets greater, the arc of the muon path gets smaller, which lowers the resolution [29].

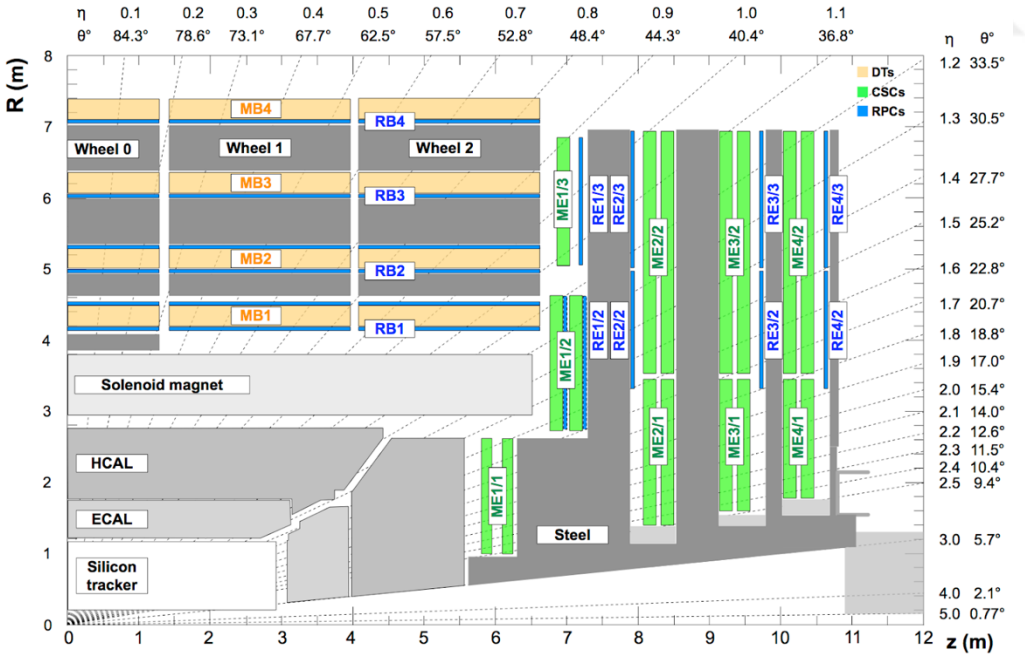


Figure 3.12. Schematic of the CMS quadrant for (2015) with colored muon sub-detectors.

3.2.7. The Trigger System

The CMS trigger system has two phases, LEVEL 1 (L1) and High-Level Trigger (HLT). While the LHC can generate data in 25 ns, the CMS can take so-called “snapshots of the collisions” synchronously with it.

It takes very high computing power and recording space if one wants to analyze all the data. Therefore, it makes sense to select promising events from a physics point of view rather than storing all events. Event selection begins with the L1 trigger, which has a data acceptance frequency of 40 MHz. Thanks to the algorithms established with hardware such as Field Programming Gate Arrays (FPGAs), the event rate is reduced to 100Khz in 3.2 μs in the presence of interesting physics objects. The L1 trigger is designed in a hierarchical structure, and at the top of this hierarchy is the Global trigger, which analyzes the event information from the sub-detectors and the Timing Trigger Control system information together, and then sends the selected events to the next Trigger, the HLT.

The frequency of events that the HLT is responsible for examining generates reasonable information to be stored in commercial RAMs. For this reason, the HLT is designed in such a way that it can select promising physics events using complex algorithms in a computing farm with 1000s of CPU power. HLT ultimately reduces the event frequency to 100 Hz with event filtering and finalizes these events by reconstructing them to be stored in different datasets. The trigger system is schematically shown in Figure 13.3. [30-32].

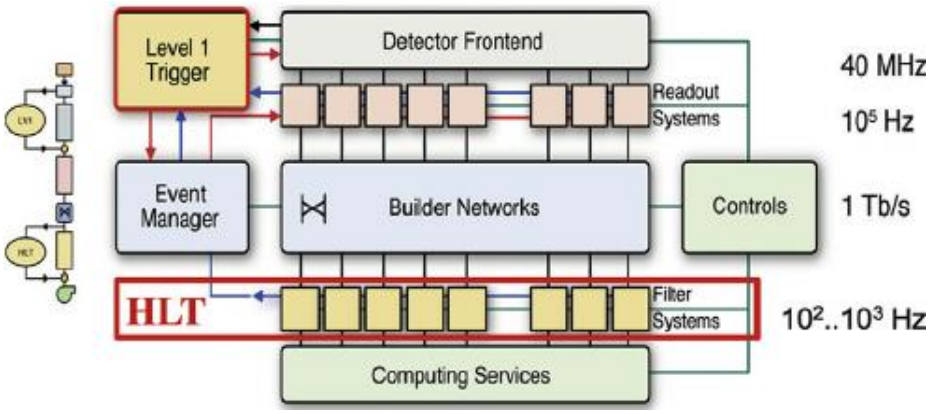


Figure 3.13. The Trigger System of CMS

3.2.8. The Particle Flow Algorithm

Particles resulting from the collision leave traces in CMS sub-detectors designed to be detected according to the properties of the particles. Since CMS has a structure like interlocking onion rings, it is designed in such a way that the particles that lose the least energy will be measured outside, and the particles with high energy loss will leave their energy in the inner parts. The Particle Flow PF algorithm has been developed to be used in analyzes using the layered and particle-selective structure of CMS. The performance of the PF algorithm has been demonstrated by many studies. It allows highly effective jet identification, electron muon discrimination, and missing transverse momentum calculations. Another benefit of the PF algorithm is that it allows cleaning pileup events that occur due to pp collisions.

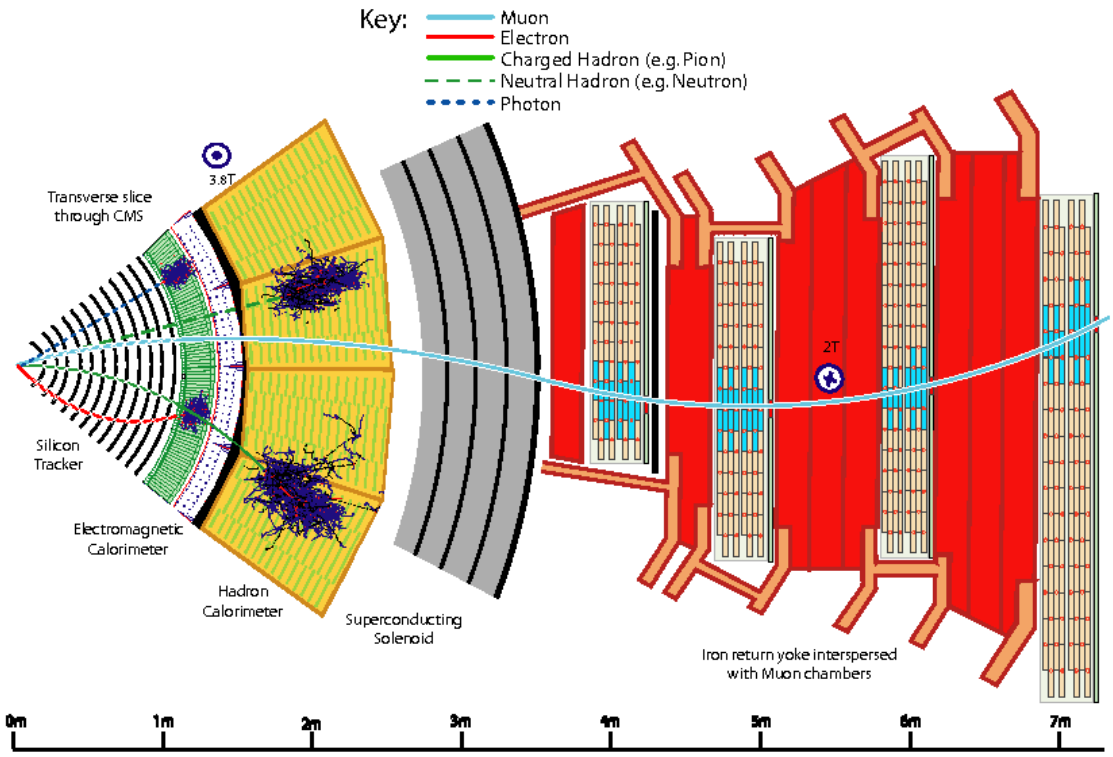


Figure 3.14. Representation of PF particle objects inside cross-section of CMS

The figure above shows how the particles are selected by the PF algorithm according to the sub-detectors. Particles are first reconstructed according to the hits take palace in detectors and then again defined by the algorithm.

Tracking particles:

Charged particles with transverse momentum greater than 0.9 GeV are formed from their tracks in pixel and strip sub-detectors of the tracker. The positions and momentums of the paths they follow are measured. In addition, secondary vertexes that may be formed by nuclear collisions are excluded with the help of iterative calculations.

Electrons:

Electrons can show themselves in the detector as part of many processes. Isolated electrons with transverse energies above 4 GeV, particles lose their energy in ECAL as a cluster. However, electrons lose part of their energies in the tracker as a result of bremsstrahlung, so the supercluster method has been developed using both the information of those photons and the ECAL cluster information. By benefiting from iterative calculations, measurable electron energy has been reduced to 2GeV. In addition to these, limitations have been applied to the electrons, which ensure that the electrons that can form in the jets are minimum, despite the possibility of measuring false electrons.

Muons:

CMS does not need the PF algorithm to detect muons. So much so that only the position and momentum of the muons can be measured from the traces on the sub-detectors such as DT and CSC. However, muons formed as a result of the collision leave their traces on the inner tracker. The PF algorithm defines these muons from 0.5 GeV to 2.5GeV as inner muons, and if the muons are larger than this energy, it seeks to find traces on any segment of the muon detectors. In addition, PF algorithm plays a role in increasing the momentum resolution by globally measuring and matching muons larger than 200GeV in both detectors.

Clustered particles:

Measurements are made by clustering the energy distributions in ECAL and HCAL. Thus, the direction and energies of the clustered particles seen in the calorimeter are measured. ECAL plays a crucial role here because, as is known from both simulations and test beam studies, the response of the ECAL, which is purposely calibrated for photons, is quite different for hadrons.

Finally, by making use of the final state particles described above, electrons are distinguished from charged hadrons, and photons are distinguished from neutral hadrons [33].

4. MATERIAL AND METHOD

4.1. Quark Gluon Jet Discrimination

In order to distinguish between quarks and gluons, we examine the jets they create. Hard scattered particles emerging from proton-proton collisions can be quarks or gluons. However, those quarks can produce gluons as well. Furthermore, initial and final radiations (ISR, FSR) can complicate these processes. The preference for hard scattered partons ΔR, that is, jets that match the pseudorapidity and azimuthal angle between the parton and the corresponding jet, is a relatively obsolete method. Instead, we use the model in which the high p_T parton is most likely formed by the hard scattering particle. This is called "the ghost model". According to the model, all the partons formed up to the moment before hadronization form that jet. In other words, the jet quark with high p_T that makes up the relevant jet is defined as a quark, and a gluon is defined as a gluon. In other cases, the flavor is not taken care of.

In the model described above, jet tagging can be done appropriately for MCs. However, the same cannot be done for collision data, because in data there are only hadrons of the final state and accompanying leptons and photons. We are still in a position to make an assessment of whether the jets come from quarks or gluons. This probability assessment is based on the theory explained in the sections above that the color charge of quarks is C_A=3 and that of gluons is C_f =4/3. From this point of view, it is possible to say that gluons will spread more than quarks with a higher probability.

There are 3 basic jet observables used in quark gluon probability calculations. These observables are given in Figure 4.1. for MC and DATA.

● Particle multiplicity: In this scope of the analysis, multiplicity distributions for gluon/quark jets for each transverse momentum beginning from 49 GeV can be found Appendix 8.1.

● Transverse minor axis σ_2: In this scope of the analysis, axis σ_2 distributions for gluon/quark jets for each transverse momentum beginning from 49 GeV can be found Appendix 8.2.

● Momentum fragmentation function $p_T D$: In this scope of the analysis, $p_T D$ distributions for gluon/quark jets for each transverse momentum beginning from 49 GeV can be found in Appendix 8.3.

4.1.1. Particle Multiplicity

We already expect more jets inside the gluons for the corresponding high momentum range from the equation $C_A/C_f = 9/4$. Therefore, particle multiplicity, which is the total number of particle candidates that make up a jet, is an important observable.

4.1.2. Transverse Minor Axis σ_2

Because the jets are spray-shaped particles coming from a point, they are observed in the form of a cone. The ellipse of the cone is defined by two axes; however, the mean jet amplitude is defined as follows:

$$\sigma = \sqrt{\sigma_1 + \sigma_2} \tag{4.1}$$

Because gluons have more particles, it is possible to say that the gluon jets should be wider, that is, their average amplitude should be larger.

4.1.3. Momentum Fragmentation Function $p_T D$

The momentum fragmentation function $p_T D$ is given as follows:

$$p_T D = \frac{\sqrt{\sum_i p_{T,i}^2}}{\sum_i p_{T,i}} \tag{4.2}$$

According to this definition, it is possible to say that $p_T D$ is a measure of the distribution of transverse momentum among the components of a jet. If the jet consists of a particle, of course, this value will go to one, if it consists of an infinite number of particles, this value will go to zero.

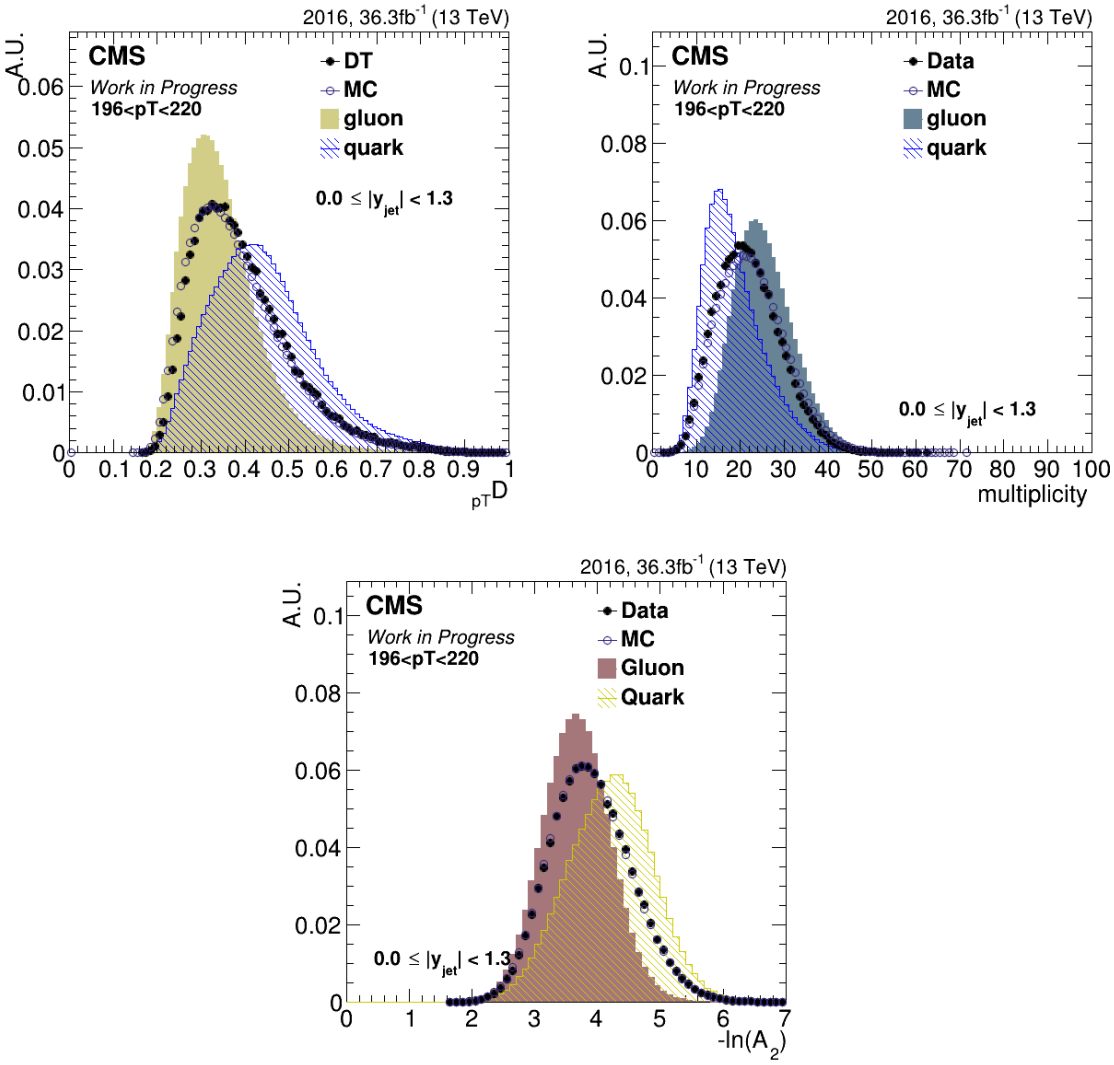


Figure 4.1. The jet observables used in quark gluon separation are particle multiplicity, σ_2 and $p_T D$, respectively

5. ANALYSIS

We used proton-proton collision data from the LHC in 2016 that was collected by CMS, along with the simulations produced for jet analysis. In this analysis, the steps of dataset selection, event selection, jet reconstruction, extraction of quark gluon jet distributions, comparison of MC-DATA, and application of the unfolding procedure were followed, respectively. C++ and C++ based Root analysis program was used for the analysis.

5.1. Datasets and Simulations

The datasets are referred to by different names of Prompt-Reco, Re-Reco and UL-Reco in line with the improvements made in general. In the quark-gluon likelihood (QGL) studies, we used 2016 Re-Reco datasets from LHC proton-proton collisions at 13 TeV. Again, Mad-Graph, Pythia and Herwig simulations created for the same data set were analyzed and the results were compared.

There are Jet tuples used by the CMS SMP-HAD group, which include the possibility of finding quarks and gluons in the data and are produced from versions of AOD samples. Tuples include variables such as QGL, P_T, Eta, and Phi for each HLT trigger, in accordance with the concerned physics, determined by the group. Similarly, tuples are produced from collision simulations using various event generators that are Pythia, Herwig and Mad-Graph.

In general, it is possible to summarize the tuples used in the analysis as particular physics-motivated data packages for analysis types for both Monte-Carlo and collision data. In this way, each group member can analyze all the events for given triggers without having to examine all the data which takes up a lot of digital space and processing time and labor work.

5.2. Event Selection

5.2.1. Trigger Selection and Luminosity

The Compact Muon Solenoid (CMS) detector receives data using High-Level and Level-1 triggers. Level-1 only extracts events from the sub-detectors (Muon Chambers and

Calorimeters). Afterwards, the High-Level trigger software selectively lowers the data retrieval rate up to approximately 1 kilohertz for desired events.

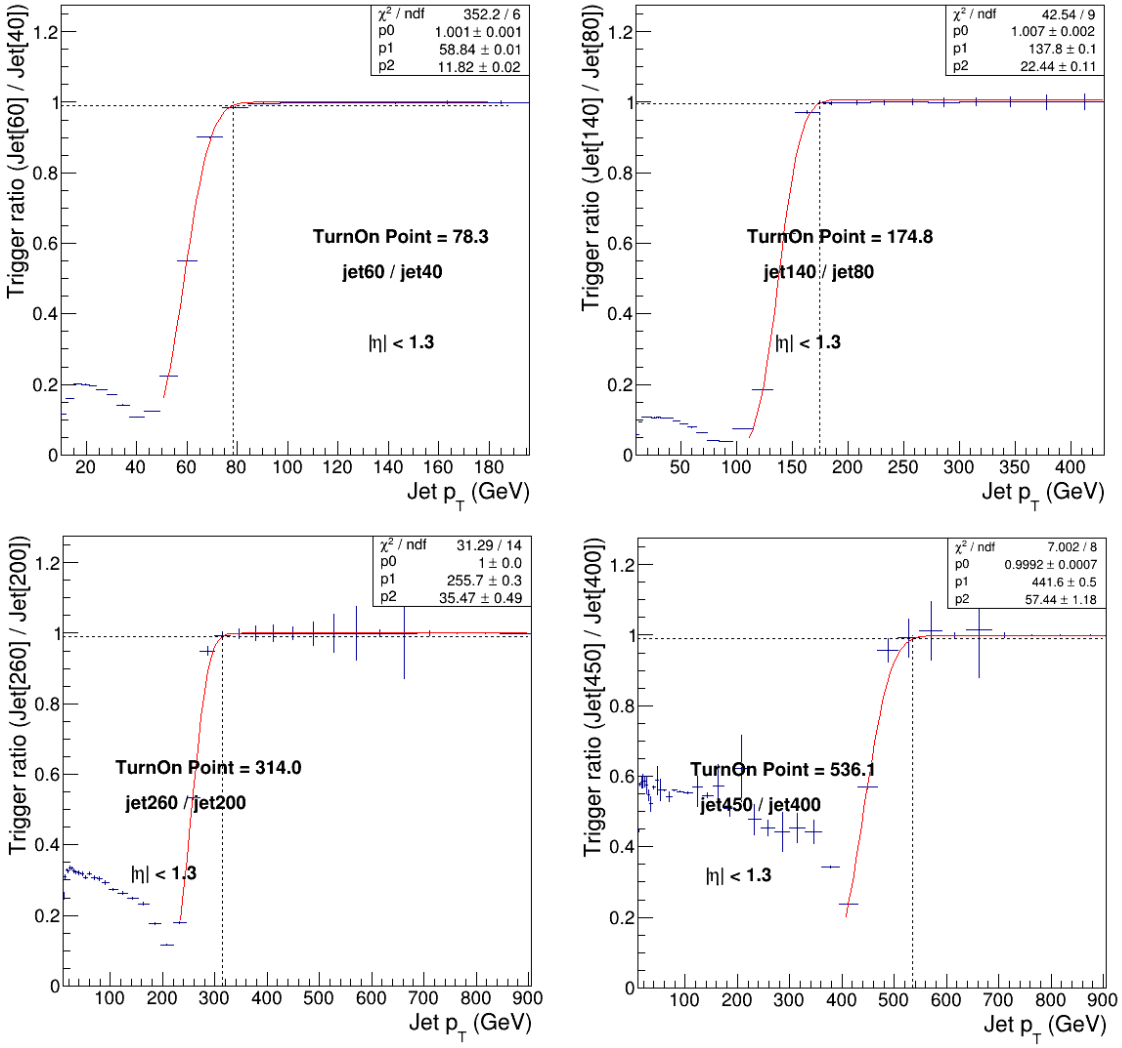


Figure 5.1. Trigger turn on curves for HLT60 (left top), HLT140 (right top), HLT260 (left bottom), HLT450 (right bottom)

The jet triggers that were used in inclusive jet studies are customized for different jet momentum ranges. For this reason, the effective ranges and effective luminosity (L_{eff}) of each trigger are different.

Considering these differences while performing the analysis, the effective luminosity (L_{eff}) values of the triggers in which PFCHS jets with a jet cone diameter (R) of 0.4 were selected, with the least overlapping effects, were calculated by means of the luminosity measuring program called BrilCalc. Afterwards, the intervals in which the triggers were efficient were found by calculating the trigger turning points.

This process is based on the principle that events that pass through the higher trigger pass through the lower trigger after the p_T distributions obtained for each trigger are divided by the effective luminosity value. Turn on curves can be seen Figure 5.1. for selected triggers, and result of calculated turn-on p_T points, corresponding effective jet pT ranges and calculated luminosity information are given in Table 5.1.

Table 5.1. Effective luminosity and turn-on values of triggers.

Trigger	L_{eff} (pb^{-1})	Turn-on p_T(GeV)	Effective Jet p_T Range
HLT40	0.267	-	0-84
HLT60	0.726	78.3	84-114
HLT80	2.758	99.6	114-196
HLT140	24.189	174.8	196-272
HLT200	103.79	236.8	272-330
HLT260	593.63	314	330-395
HLT320	1772.1	385.6	395-468
HLT400	5193.1	453.6	468-548
HLT450	36310.1	536.1	548- ∞

Turn-on points determined for each trigger naturally determine where sequential triggers work effectively. For instance, the HLT140 jet trigger works efficiently between its turn-on 196 GeV and the turn-on 272 GeV of its successor HLT200. All trigger turn-ons and effective ranges are determined with similar logic.

Thanks to this method, both double counting's of events from different triggers are prevented, and the events in the intervals are excluded for the inefficient triggers.

5.2.2. Jet Energy Correction

Particles from proton-proton collisions travel through the CMS and leave their signals in sub-detectors such as tracker, electromagnetic and hadronic calorimeters. Afterwards, these signals are brought together in the calorimeter with the help of jet algorithms. The jet clusters are constructed, then the overlapping jets are separated from each other with the help of the tracker detector. However, this does not mean that all the jets we reconstructed exactly reflect the characteristics of real jets.

Since the reconstructed jets are not exactly the same as the real jets for the reasons given above, a series of jet energy corrections are made to the analyzed jets. First of all, jet energy scale (JES) from overlapping jets and jet resolution, jet response corrections for the determined p_T intervals are added to the analysis. Afterwards, the corrected jet distributions are obtained by including and adding the residual corrections with the jets dijet (bijet) and the Z+jet events. Similarly, corrections are made to the jets obtained in the simulations. Figure 5.2 shows the schematic structure of these corrections.

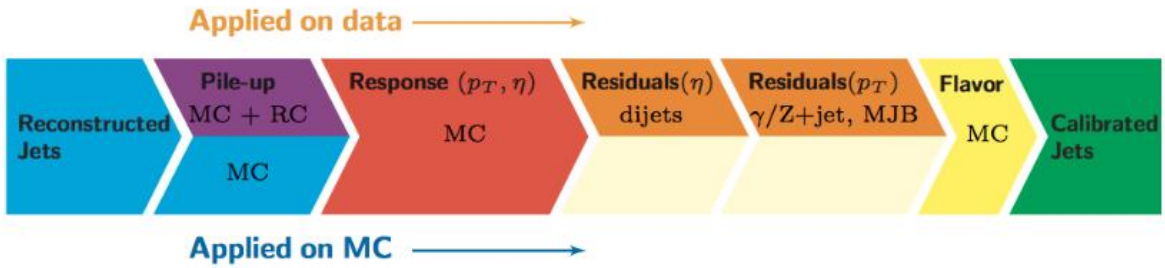


Figure 5.2. CMS jet calibration chart

These correction terms applied to the analysis are regularly generated by the Jet-MET group for each data set. We used the correction values (Summer16_07Aug2017_V18 MC and Data) shared by this group and recommended by the CMS in the analysis.

5.2.3. Pile-up Weight Correction

Data and MC compatibility is related to more than one parameter specific to jets. First, luminosity corrections are necessary for both MC and DATA. However, since the pile-up values for DATA and MC are different, MC events need to be re-weighted.

Pile-up event distributions are obtained for each jet trigger with the help of BrilCalc command line tool developed by the CMS Beam Radiation Instrumentation and Luminosity (BRIL) group. Afterwards, corrections are made considering the luminosity values. In Figure 5.3. we see the pile up distributions for MC and DATA.

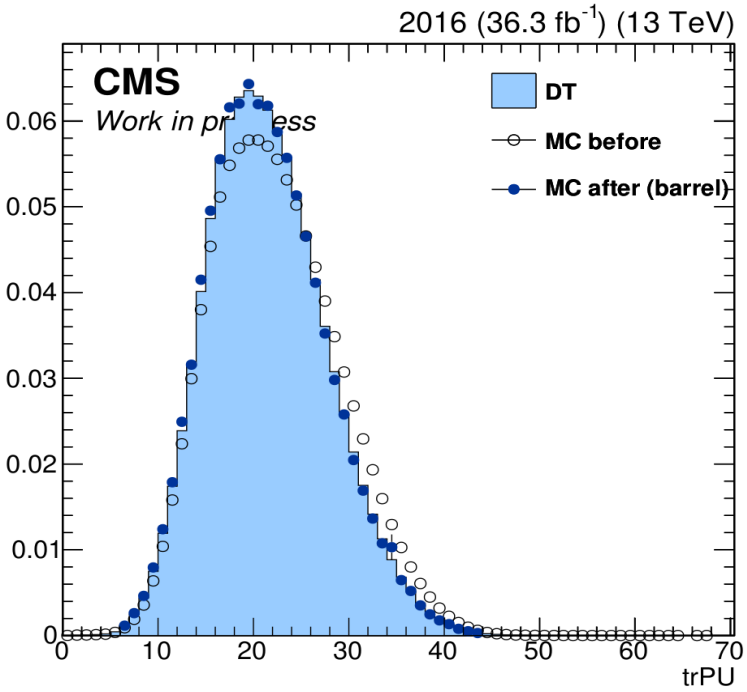


Figure 5.3. Pile up distributions

In the Figure 5.3 pile up distributions are given for the 2016 data acquisition period, DATA is shown in light blue, MC with hollow circles, and corrected MC pile-up distributions with solid blue circles for the barrel region. Here, the total pile-up distributions of all triggers are used for ease of illustration. However, the PU correction terms were applied separately to the MC jets for each trigger and each data acquisition period.

The amount of luminosity recorded by each trigger is obtained with the help of BrilCalc software developed by Bril group.

5.2.4. Correction for Detector Effects

In addition to the corrections detailed above, due to the detector problems specific to the 2016 data, extra corrections were applied while measuring jets in this analysis. These detector problems and corrections are described below.

5.2.4.1. Hotzone and Coldzone Map

For the precision measurements of jet cross section, ineffective regions of the detectors where the jets are over or under-measured should be determined and discarded from both the collision data and MC

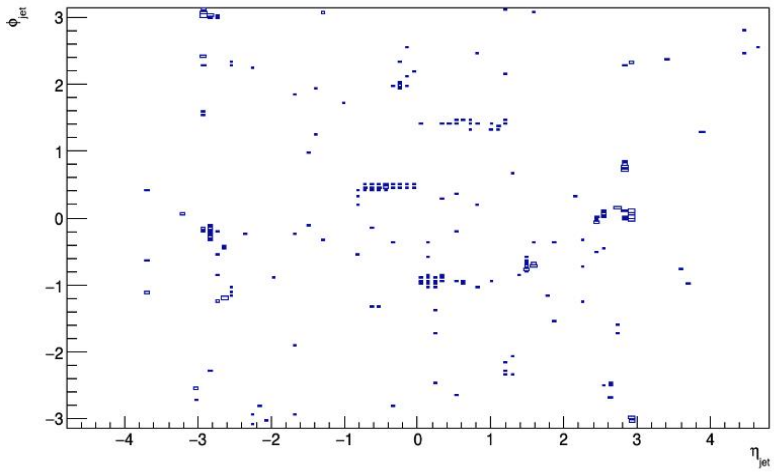


Figure 5.4. Hotzone map for both DATA and MC in 2016

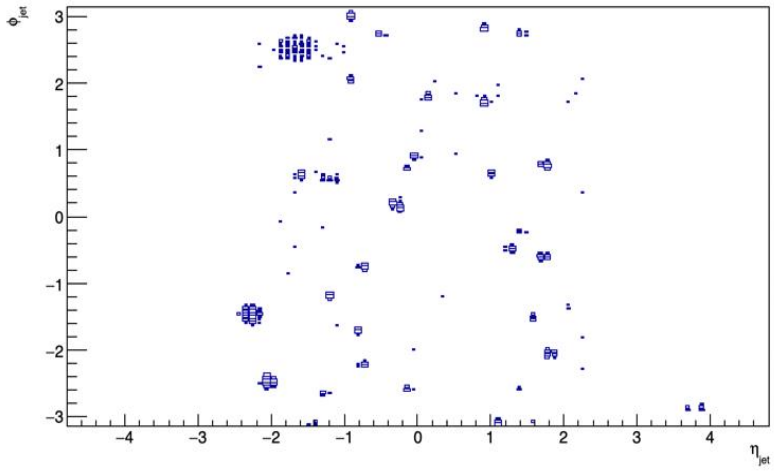


Figure 5.5. Coldzones map for both DATA and MC in 2016

Suppose these ineffective regions of the CMS detector, which has been operating under high radiation for years, are adequately described in the MC. In that case, these

problematic regions may not need to be removed, but with Run II, these regions have increased, and MC-Data discrepancies have become more evident. To overcome this problem, examining these regions in the eta and phi planes of the jets is sufficient. Throughout this study, the regions where the jets are measured more are defined as "hot", and the regions where the jets are measured less are defined as "cold" regions. The "hotzone map" produced for MC with the 2016 collision data in the JEC Database is shown in Figure 5.4, and the "cold zone map" in Figure 5.5.

Jet Veto Map calculations, that is, obtaining maps where hot and cold jet regions are excluded from the analysis, is based on the principle that the CMS detector is symmetrical in the phi axis. It is possible to physically identify each HCAL tower by specifying the phi-eta axes appropriately. Moreover, Jet Energy Correction calculations also use these eta values. The logic of the calculation is simple: for each phi, the number of jets on eta for the respective trigger is determined and divided by the number of jets on the calculated phi axis. Then also the standard deviation (sigma-σ) is calculated in a similar way. Thus, the mean value and the corresponding σ for each eta-phi plane are obtained. Finally, eta-phi zones deviating by 3σ are defined as hot or cold zones. In our analysis, hot-cold zone maps corresponding the collision data of 2016 and MC were used, and the relevant jets were vetoed [34].

5.2.4.2. ECAL Prefire

2016 and 2017 data are problematic for certain events due to the timing problem of the ECAL detector's L1 trigger, and this is known as the ECAL Prefire problem. This problem is essentially caused by the time-lapse of ECAL, accidentally transmitting the information of the previous bunch data to the L1 trigger instead of the bunch at the time of the collision, in addition to the L1 trigger not receiving data for two consecutive bunches. As a result, a significant amount of energy, which must be measured in ECAL at the time of the collision, is lost.

There are various methods to overcome this problem in the analysis, but the core is similar for each one. In events triggered by single jets, jets in eta <2 are tagged and jets their p_T bigger than 40 GeV found in the $2. < |\eta| < 3.5$ are probed. This method ensures that probed jets are responsible for pre-firing. Then, the probabilities are obtained by dividing the

events in which the probe jets are found by the events in which the probe jets are not found.

As a result of these calculations, probability maps were prepared. The ECAL pre-firing map for 2016 data used in our analysis is shown in Figure 5.6. With the map shown, events with jets corresponding to the relevant eta-phi region are re-weighted. The equation 5.1 was used while the events were weighted.

$$w = 1 - P(prefiring) \tag{5.1}$$

where, w corresponds to weight, and P(prefiring) corresponds to the probability of being prefired for that particular event.

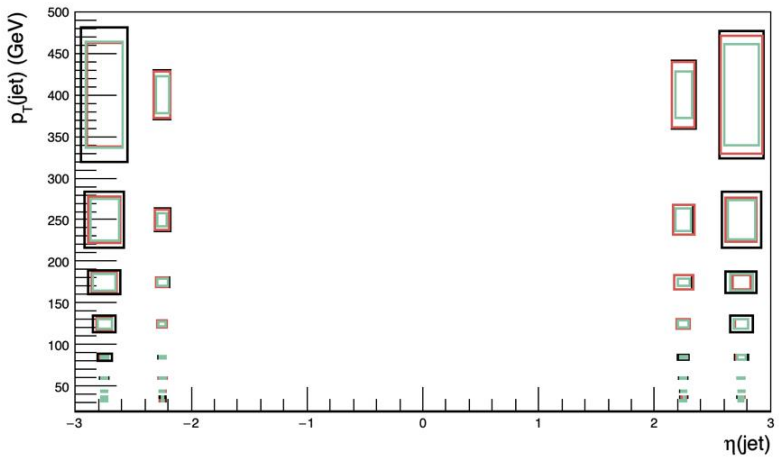


Figure 5.6. ECAL Prefire Map both for 2016 data and MC [35].

5.3. Particle Flow-PF Jet Reconstruction

PFCHS jets with a cone radius of 0.4 were used in the analysis. These jets are the least affected by overlapping events. Particles in these jets are created by using information from each sub-detector of the CMS. These particles are charged and uncharged of hadrons, and electromagnetic particles. In other words, jets are made up of these particles. The distribution of PF particles in the jets helps us to understand the characteristics of the jets.

The barrel region of the CMS detector is relatively unified by the tracker detector, electromagnetic calorimeter, and hadron calorimeters, which cover the -1.3 and +1.3

rapidity region. For this reason, the jet reconstruction is superior in this region rather than other rapidity regions.

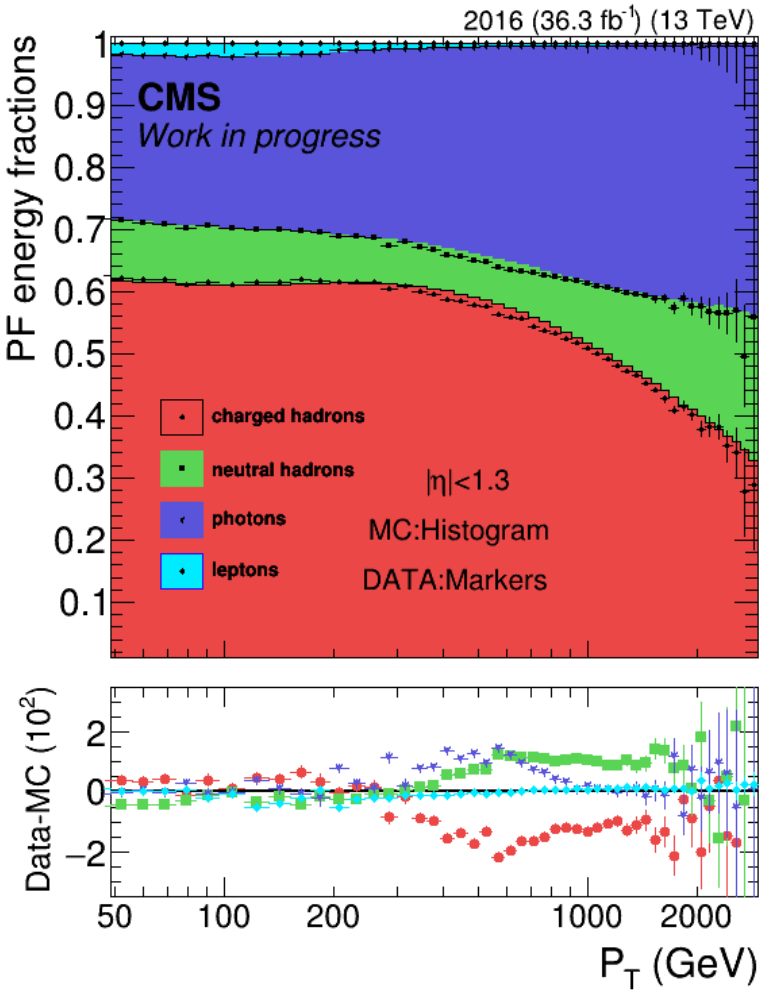


Figure 5.7. PF Energy distribution histogram for the CMS Barrel region

The proportions and distributions of the particles forming the jets according to the jet energies are shown in Figure 5.7 for both MC and DATA. When the Figure 5.7. is examined, the jet energy distributions are coming approximately 60% from charged hadrons, 11% from neutral hadrons, 28% from photons and 1% from leptons. However, DATA/MC compatibility is over 98% for each PF particle when jet selection criteria are met, and corrections are made.

5.4. QGL and Quark Gluon Jet Distributions

Distinguishing whether jets come from quarks or gluons at the LHC is of great importance for new physics studies. Within the scope of the analysis, inclusive jet measurements were

carried out using the 2016 data of particle flow jets with a cone radius of R=0.4 in CMS, and quark gluon probability distributions were produced for the trigger p_T intervals given effective ranges in trigger selection section above.

5.4.1. Quark Gluon Likelihood

The identity information of reconstructed jets in MC is defined by the ghost method. With the help of the corresponding jet variables, such as particle multiplicity, σ_2 and $p_T D$, the identity of a jet is generated as probability distribution functions. Quark and gluon density functions are defined as follows in the product of the pdfs corresponding to each variable.

$$G(\vec{x}) = f_G\ \left(x_{P_T D}\right) f_G\ (x_{\sigma 2}) f_G\ (x_{mult}) \tag{5.2}$$

$$Q(\vec{x}) = f_Q\ \left(x_{P_T D}\right) f_Q\ (x_{\sigma 2}) f_Q\ (x_{mult}) \tag{5.3}$$

The Quark Gluon Likelihood (QGL) Discrimination is generated from Gluon and Quark jet probability density functions so that the QGL discriminant is defined on the probability of being a quark as follows.

$$QGL(\vec{x}) = \frac{Q(\vec{x})}{Q(\vec{x}) + G(\vec{x})} \tag{5.4}$$

The calculation is done for desired transverse momentum, pseudorapidity and offset energy density of the jets.

Both for MC and data, the QGLs produced from the probability distribution functions for the jets selected p_T bins in the barrel region are shown in Figure 5.8. The jets in the MC are shown as stack plots in line with the information obtained from the parton flavor so that one can see quark and gluon explicitly.

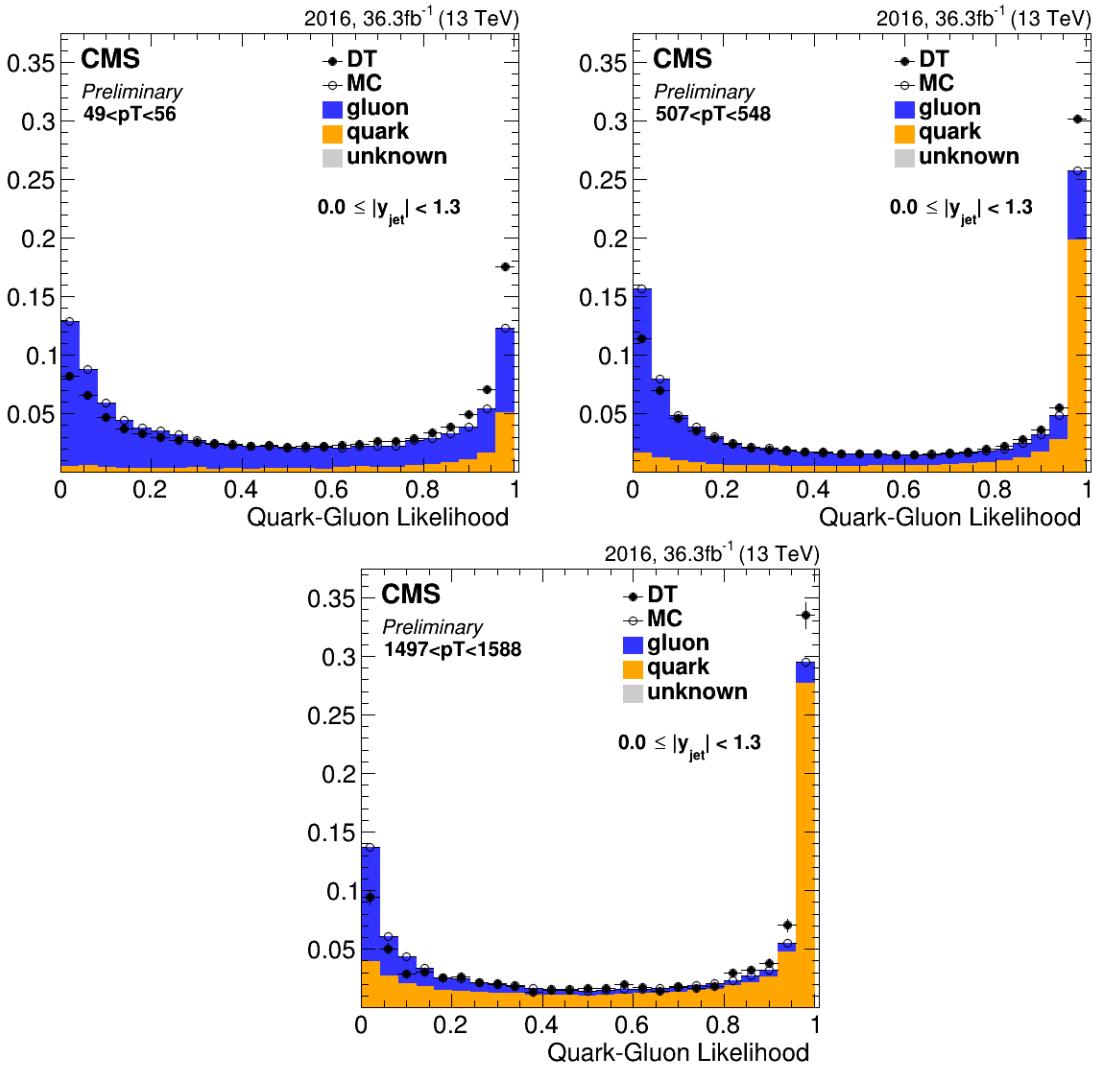


Figure 5.8. QGL distrubutions of jets in the barrel of the CMS for selected p_T bins

5.4.2. Quark Gluon Template and Scale Factors

QGL distributions allow us to distinguish jets with their parameters affecting the jet radius. The QGL distributions are analyzed together with the scale factors to increase the Data and MC compatibility for the gluon and quark QGL distributions. Scale factors for gluon and quark jets are calculated for their bins of each QGL distribution from the 2x2 linear system given below.

$$N_{data}^{DY} = w_g N_{MC,gluons}^{DY} + w_q N_{MC,quarks}^{DY} + N_{MC,unknown}^{DY} \quad (5.5)$$

$$N_{data}^{QCD} = w_g N_{MC,gluons}^{QCD} + w_q N_{MC,quarks}^{QCD} + N_{MC,unknown}^{QCD} \quad (5.6)$$

w_g w_q values are obtained by using Z+jet events rich in terms of quark jets for the DrellYan process, and dijet events for the QCD process. Scale factors for gluon and quark QGLs are used in the analysis is as given in equation 5.7 and 5.8.

For Pythia8 MC with tune CUETP8M:

$$w_{quark(|\eta|<2.0,p_T)} = -0.666978\,x^3 + 0.929524\,x^2 - 0.255505\,\mathrm{x} + 0.981581 \quad (5.7)$$

$$w_{gluon(|\eta|<2.0,p_T)} = -55.7067\,x^7 + 113.218\,x^6 - 21.1421x^5 - 99.927x^4$$

$$+92.8668\,x^3 - 34.3663\,x^2 + 6.27\,\mathrm{x} + 0.612992 \quad (5.8)$$

In this analysis, partonic fractions were obtained from the data QGL by applying the scale factors to partonic MC QGL distributions.

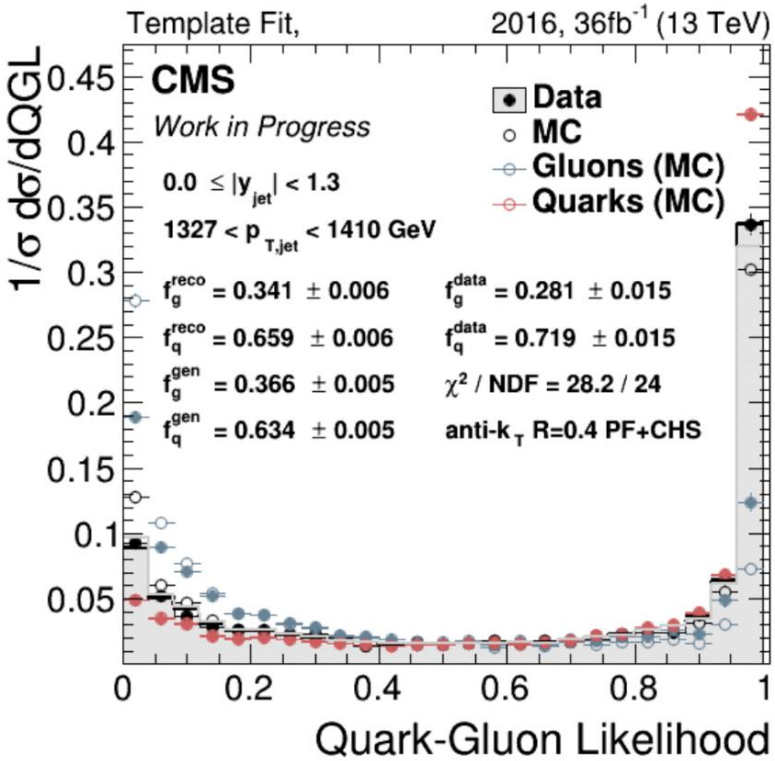


Figure 5.9. Quark gluon probability distributions

Figure 5.9 shows the QGL distributions of the jets in the barrel region and the fractions obtained as a result of the template fit for bin $1327 < |\,p_{Tjet}\,| < 1410$. The black and gray line are the template fit of the data and MC respectively. The full and empty circles are scaled QGL and QGL distributions respectively. In the same plot, calculated fractions of

gluon-quark jets are represented with statistical errors that can be found for gen jets, reconstructed MC jets, and data jets.

QGL distributions with template fit can be found in Appendix 8.5 for other jet p_T bins.

5.4.3. Quark Gluon Jet Fractions

The quark and gluon jet fractions obtained from the template fits are shown in Figures 5.10. and 5.11. as a function of the jet p_T. In Figure 5.10, firstly, the quark-gluon fractions for selected jet p_T points corresponding to the trigger intervals are shown, then the fractions for each jet p_T value are detailed in Figure 5.11.

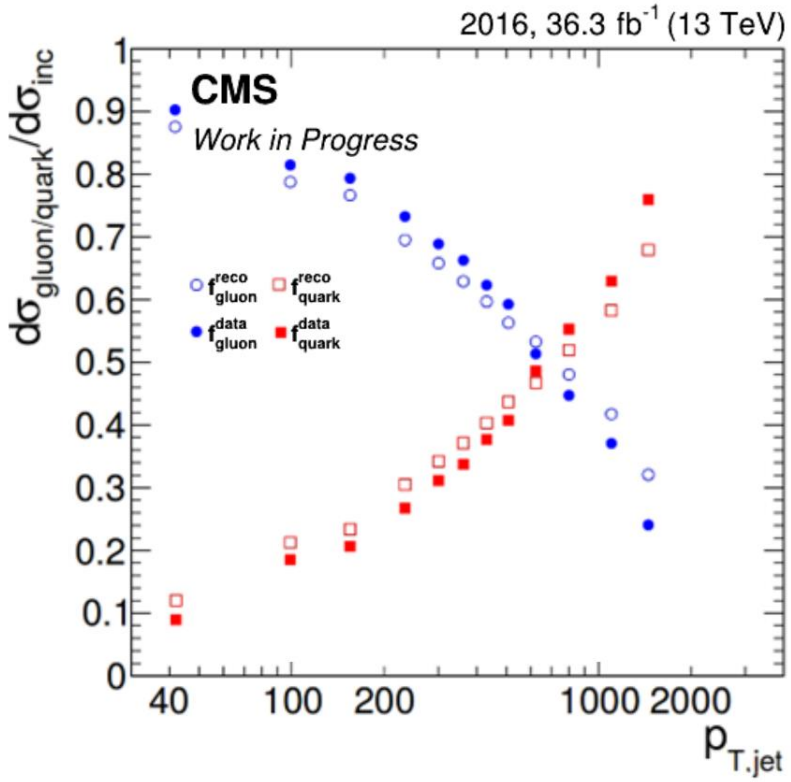


Figure 5.10. Quark gluon fraction distributions for jet p_T corresponding triggers

In the Figure 5.10. given above, solid blue and red markers represent gluon and quarks for data, respectively, while hollow blue and markers represent MC simulation results for gluon and quark jets, respectively. The first eight trigger values are represented by only one transverse momentum value, while the last trigger, which itself covers jet p_T range from 584 GeV to 6500 GeV, is represented by 4 separate jet p_T values.

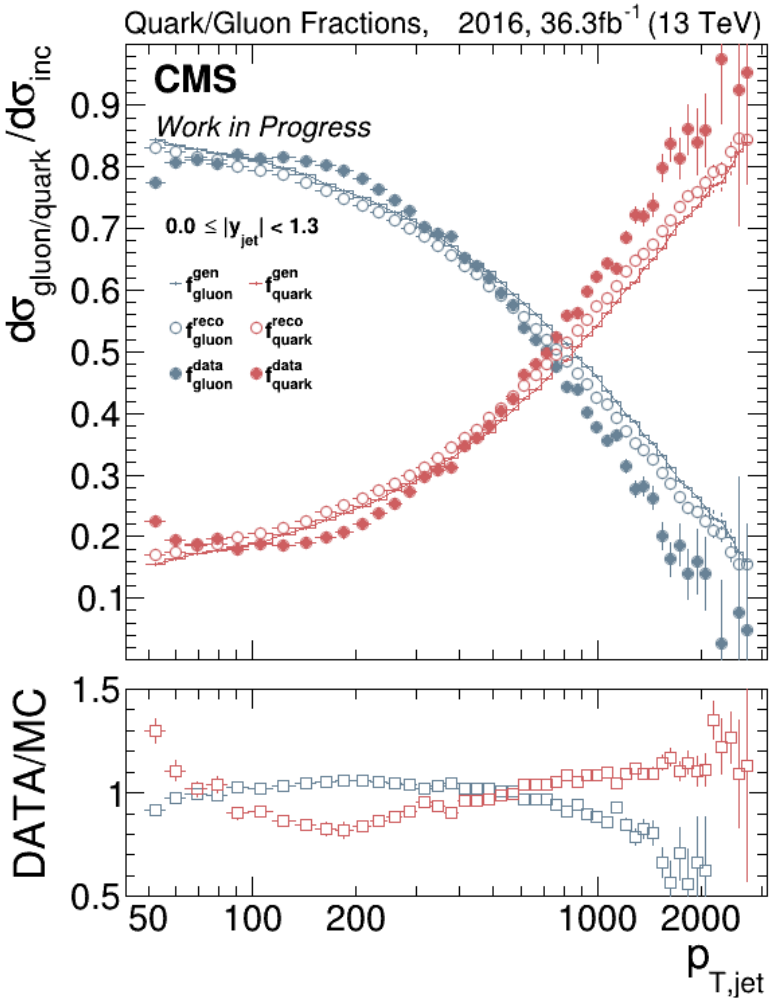


Figure 5.11. Quark and gluon jet fraction distrubutions for each jet p_T

The jets used in Figure 5.11 cover the rapidity region of |eta|<1.3 for jet p_T from 49 to 3100 GeV by following the analysis steps described in detail above. Quark and gluon fractions obtained from these jets are shown in the Figure 5.11. with statistical uncertainties. The MC used is Pythia8 with tune CUETP8M1.

Similar to the previous illustration, blue color was used for gluons, while red color was chosen for quarks. Line representations show generated information, i.e., particle level particles in MC, while hollow and full markers show reconstructed objects for MC and data, respectively.

5.5. Monte Carlo Generator Comparisons

In this Monte Carlo generator comparisons section, gluon quark distributions were examined using different MC generators. First, Herwig and Pythia samples were compared. Different results were obtained depending on whether unknown jets were included in the analysis.

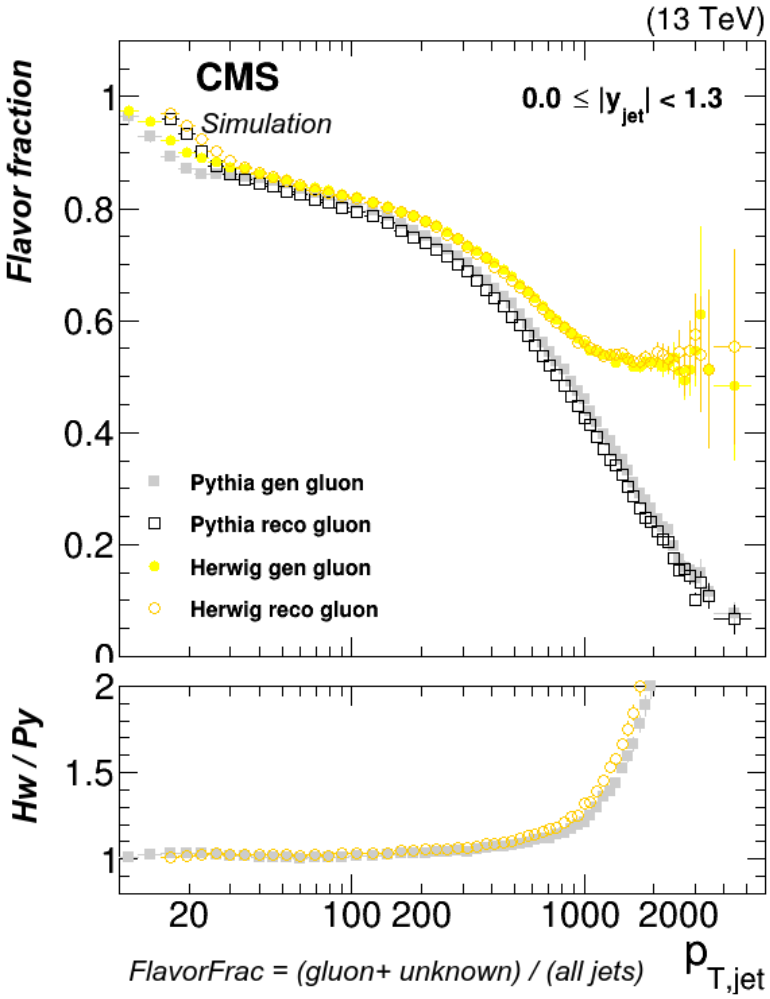


Figure 5.12. Gluon distributions for Pythia and Herwig

When we compared Herwig MC with Pythia8 MC, it was observed that the gluon fractions deviated greatly from Pythia.

In Figure 5.12, a discrepancy is evident between the yellow and gray markers at high p_T values. In order to understand the problem, gluon fraction distributions excluding unknown jets are given in Figure 5.13.

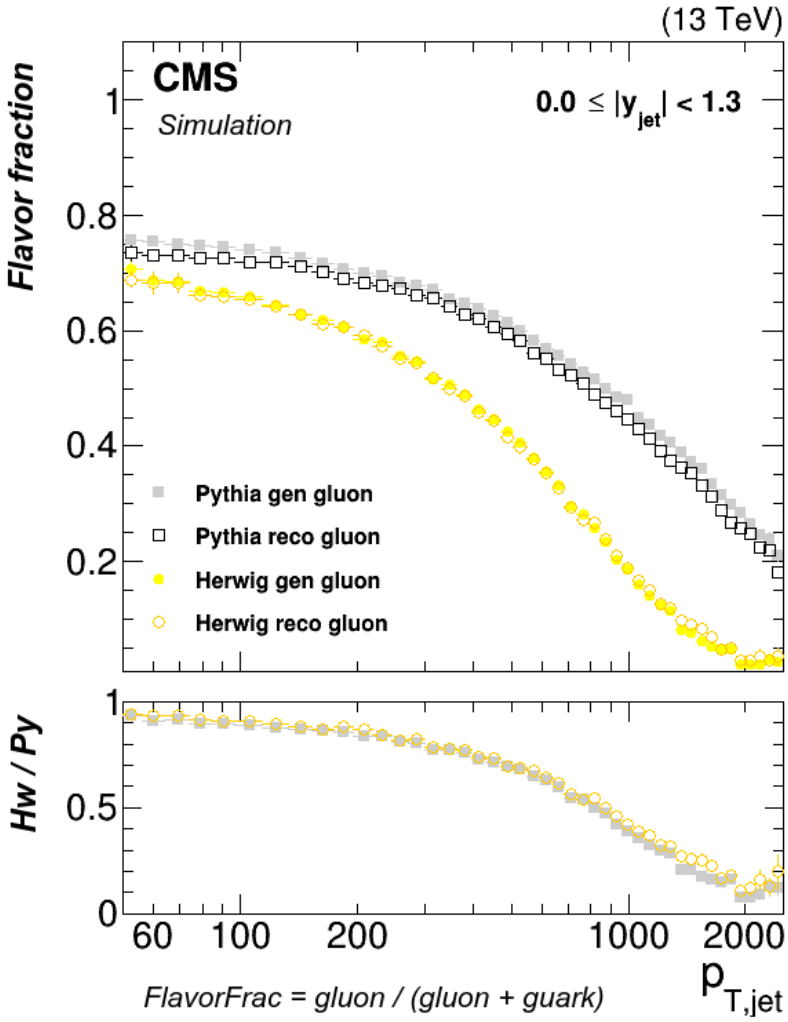


Figure 5.13. Gluon flavor fractions without unknown jets for Pythia and Herwig (if unknown jets are excluded)

It should be understood from Figure 5.13 that the behavior of unknown jets is different for Pythia and Herwig. To understand the problem, both multi-jets and dijets for Herwig MC and dijets with Pythia MC were studied. In Figure 5.14 we see the comparison of Mad-Graph and Pythia for multi-jets.

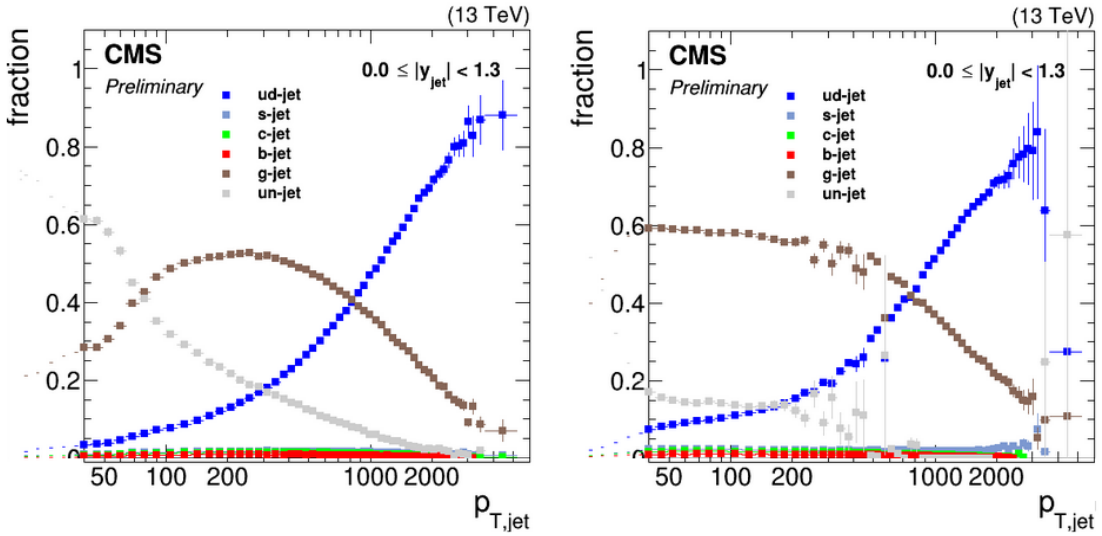


Figure 5.14. Jet flavor distributions, Pythia on the left, MadGraph on the right

In Figure 5.14, the blue markers represent the up and down quarks, the light blue, the green, the red, the brown and the gray markers represent strange, charm, bottom quarks, gluons, and unknown partons respectively. For Mad-Graph, it is possible to say that the number of unknown partons is relatively small but still screens the gluons.

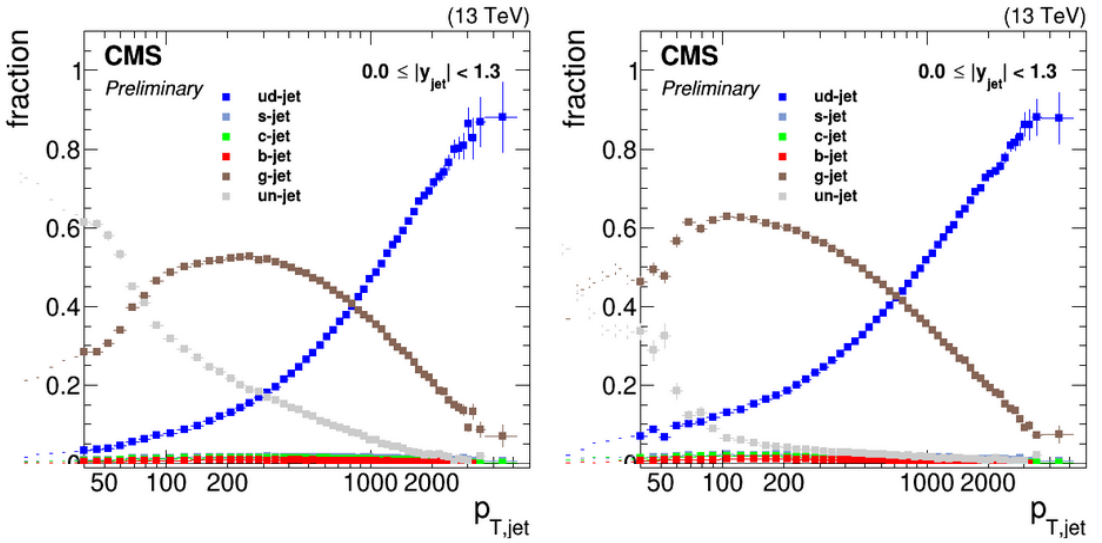


Figure 5.15. Jet flavor distributions, multijet Pythia on the left, dijet Pythia on the right

In Figure 5.15, the same color distributions are used for the jets. Pythia MC results for dijet events show much fewer unknown jets than Pythia MC results where multijet events are selected. From the above comparisons, one can say that unknown jets at low p_T increase drastically no matter what jets are multijets or dijets. Then the gen-reco matching

criteria below 100 GeV was tightened so that PU contamination could be under control, and similar dijet and multijet comparisons were performed (Figure 5.15).

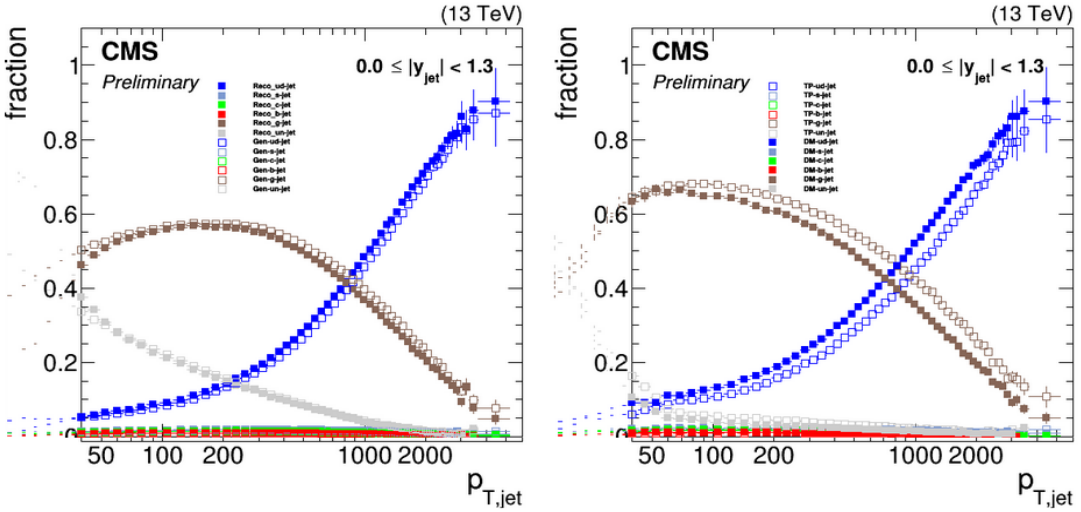


Figure 5.16. Jet flavor distributions. Multijet Pythia on the left, dijet Pythia on the right (with strict gene-reco matching criteria)

In the section where different MCs were tested, it was observed that the unknown jets in the Herwig MC affected both gluon and quark jets. However, unknown jets in Pythia8 MC affected the gluons. Figure 5.16 shows that if pu jets are taken under control, unknown jets can be avoided in dijet events such that the rate of these jets above 50 GeV has dropped below one percent.

5.5.1. Jet Response of Quarks Gluons Unknown Jets

In this section, the response distributions of jets are studied with partonic information. Response distributions are simply obtained by the ratio of each reconstructed jet p_T to particle-level jet p_T if a reconstructed jet is matched with a particle-level jet.

For Pythia MC, response distributions of jets are represented in Figure 5.17 for inclusive jets, gluons, quark, and unknown jets. When the Figure 5.17 is examined, it is observed that the inclusive jet response is completely different for gluons and quarks, while unknown jets are structurally the same as gluon jets.

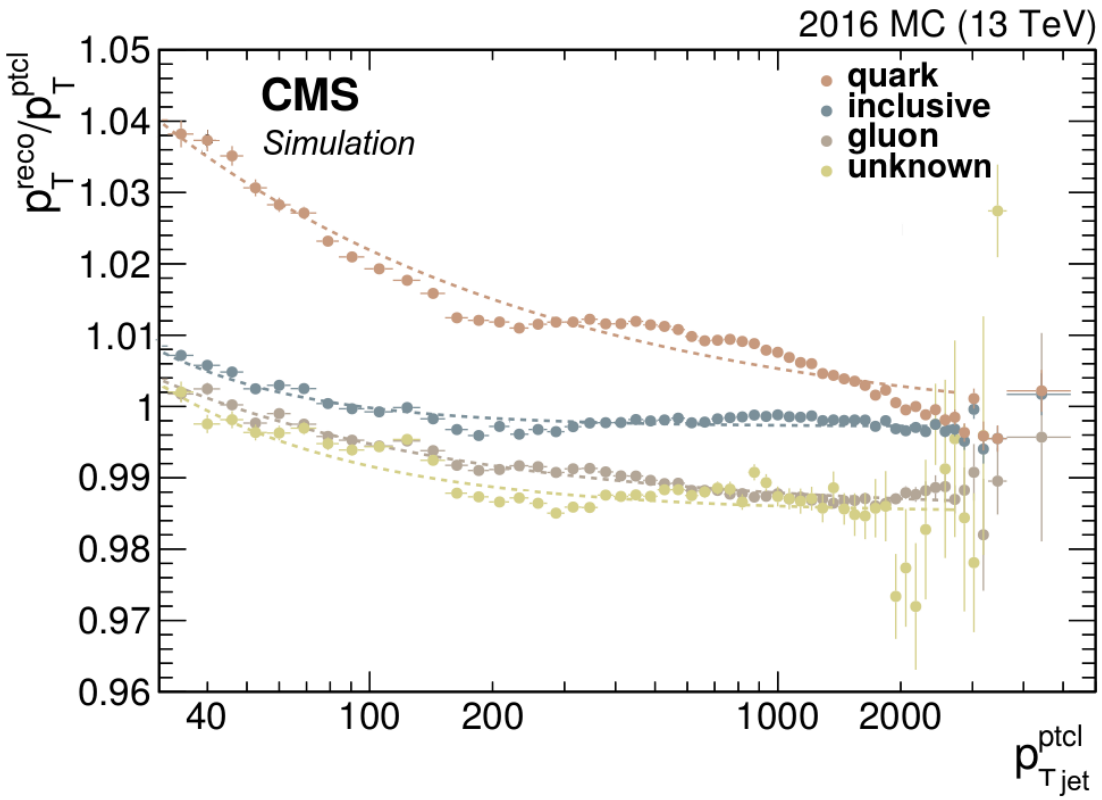


Figure 5.17. Response plot of quark, gluon and inclusive jets.

5.6. Unfolding

So far, the main structure of the analysis has been successfully established. 2016 Re-reco dataset and QCD Flat simulation with defined quark and gluon flavors produced with Pythia8 were compared for jets p_T with the jet energy corrections Summer16_07Aug2017_V18. As a result, we see in Figure 5.18 that the template fit method allows quark-gluon separation for each transverse momentum value.

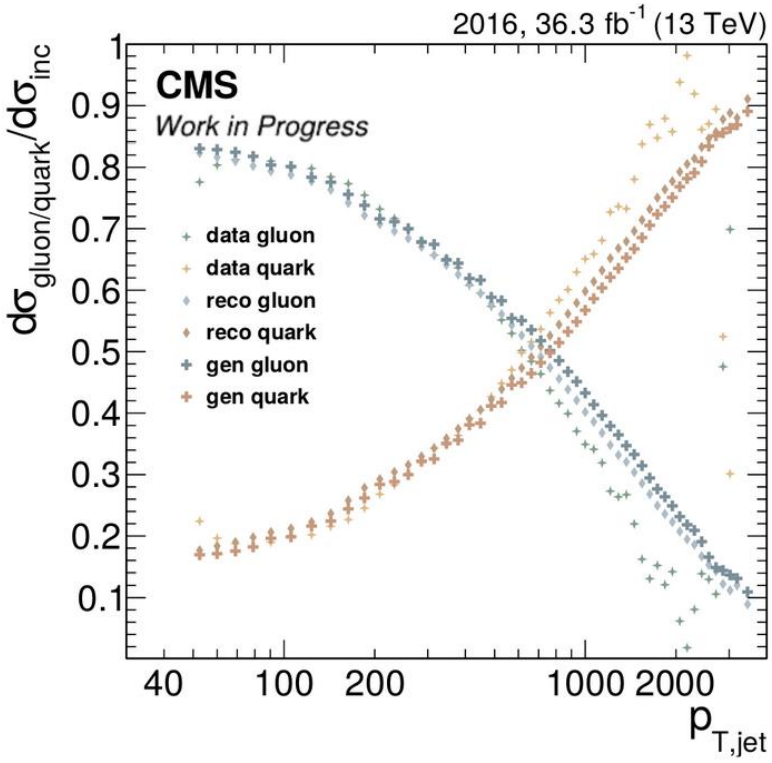


Figure 5.18. Quark and Gluon jets fractions.

Figure 5.18 shows how the fractions of quark and gluon jets are distributed according to transverse momentum. Here, quark jets are given in warm colors and gluon jets are given in cool colors. These distributions are shown for jets obtained from 2016 collision data, reconstructed (reco) jets, and generated (gen) jets.

As expected, gluon jets dominate inclusive jets at lower momentum values and quark jets dominate inclusive jets at higher momentum values. Additionally, when Figure 5.18 is examined for both quark jets and gluon jets, it is seen that the reco distributions are mostly between data distributions and gen distributions. Simply moving both the data and the MC reco distributions to the generation level, that is, improving them to converge to gen distributions, will increase the compatibility between data and simulation.

The differences between the collision data and the simulation in the measurements are likely to come from statistical fluctuations, and it is possible to say that this difference will close with increasing statistics. However, even if the statistics are sufficient, it can be seen that the gen p_T distributions and reco p_T distributions of both gluon- and quark-jets differ from each other when only the simulation results are examined. This difference is a natural consequence of the fact that the jets observed in a range of a bin come from

neighboring bins (migration) due to the finite detector resolution, and this causes smearing for particular p_T ranges in 2D histograms. Unfolding is an attempt to fix this problem by applying backwards corrections to both data and reco objects.

Mathematically, the unfolding problem can be defined as:

$$\int_{\Omega} K(y,x)f(x)dx = g(y) \tag{5.9}$$

where g(y) and f(x) represent the measured and real momentum distribution, respectively, and K(y,x) represents the source function that moves f(x) to g(y). Also, Ω represents a constant phase space. The solution of such a Fredholm integral equation of the first kind is considered among the so-called inverse problems.

In this study, the RooUnfold library, which can work with the Root analysis program, was used to make the unfolding calculations.

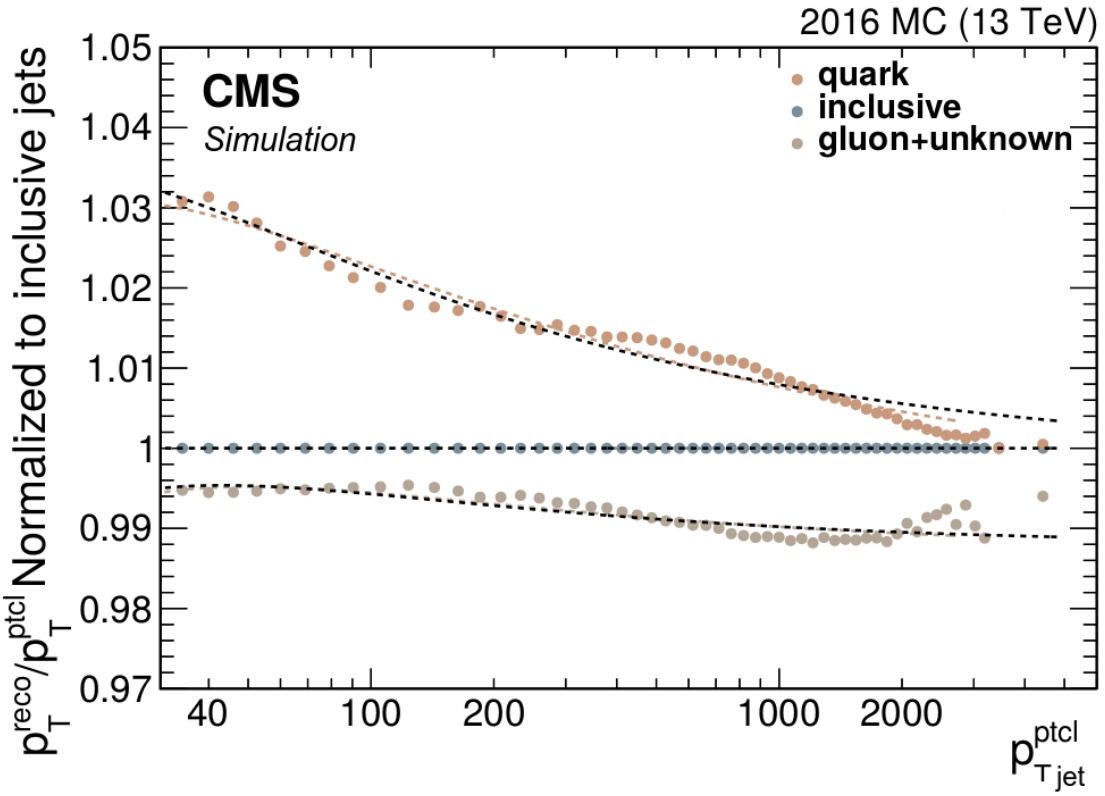


Figure 5.19. Quark and gluon jet response histogram normalized to inclusive jet measurement

The quark-gluon jet response distributions obtained from study shown in Figure 5.19 were normalized to the inclusive jets. So that quark and gluon jet response matrices can be simulated.

When Figure 5.19, quark and gluon jet response distributions normalized to inclusive jets, it is clear that the response of gluon jets is less than the response of the quark jets. These results coincide with the knowledge of how the jets are hadronized in the calorimeter. Since gluon jets contain more particles, the gluon jet response is lower than the overall jet response, while the quark jet response is high and decreases as momentum increases, as expected for all.

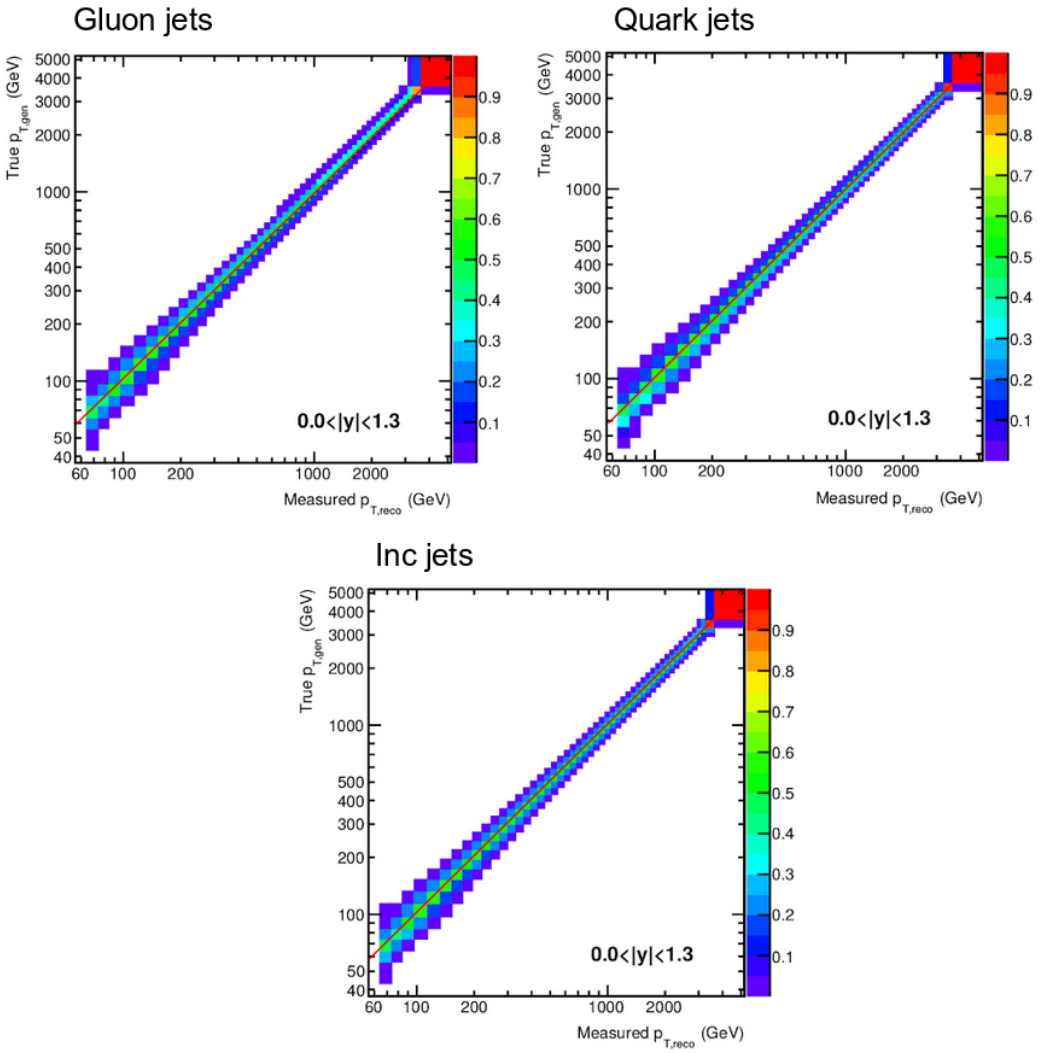


Figure 5.20. Response matrices

While performing unfolding studies, firstly, two-dimensional response matrix histograms were produced with the help of RooUnfold library (Figure 5.20). The response matrices show the extent of the p_T smearing over the entire p_T spectrum. This representation is given as a two-dimensional histogram in which the measured p_T (Measured p_T, reco) values are displayed in colors against each true p_T (True $p_{T, gen}$) value. These histograms are again produced separately for gluon, quark, and inclusive jets. The quark and gluon histograms can also be verified by inclusive jet measurements. As can be seen from the histograms in Figure 5.20, smearing effect takes place at high momenta for gluon jets, while relatively fewer smearing takes place at low momenta for quark jets. This is consistent with the response distributions given in Figure 5.19.

Afterwards, the correction factors resulting from the unfolding process were produced using the RooUnfold program and forward smearing method. That is, based on the response matrix, correction values were produced that allow each measured transverse momentum value to be transferred to the real momentum value. Figure 5.21 shows these corrections for both simulation and collision data. Here, blue circles represent gluon jets, black circles represent quark jets, and red circles represent inclusive jets. Hollow circles represent data corrections, filled ones represent simulation corrections. The corrections corresponding to the inclusive jets were found to be between the quark and gluon jets for both simulation and data. In corrections at high momentums, there are transitions depending on statistics.

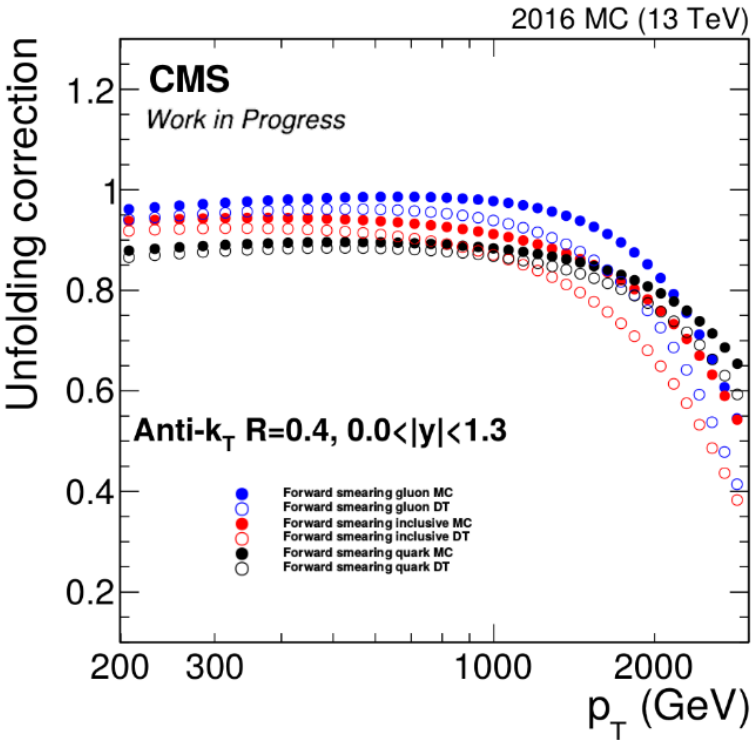


Figure 5.21. Distribution of unfolding correction factors

Correction factors were applied to the simulation results of reco jets to obtain unfolded jets. In Figure 5.22, for the MC unfolded jets, reco jets, and gen jets are shown as a fraction distribution. In order to see how well the unfolding process works, closure graphs are also added to the fraction distribution plot. In the closure, MC corresponds corrected reco jets and Gen corresponds generator level jets.

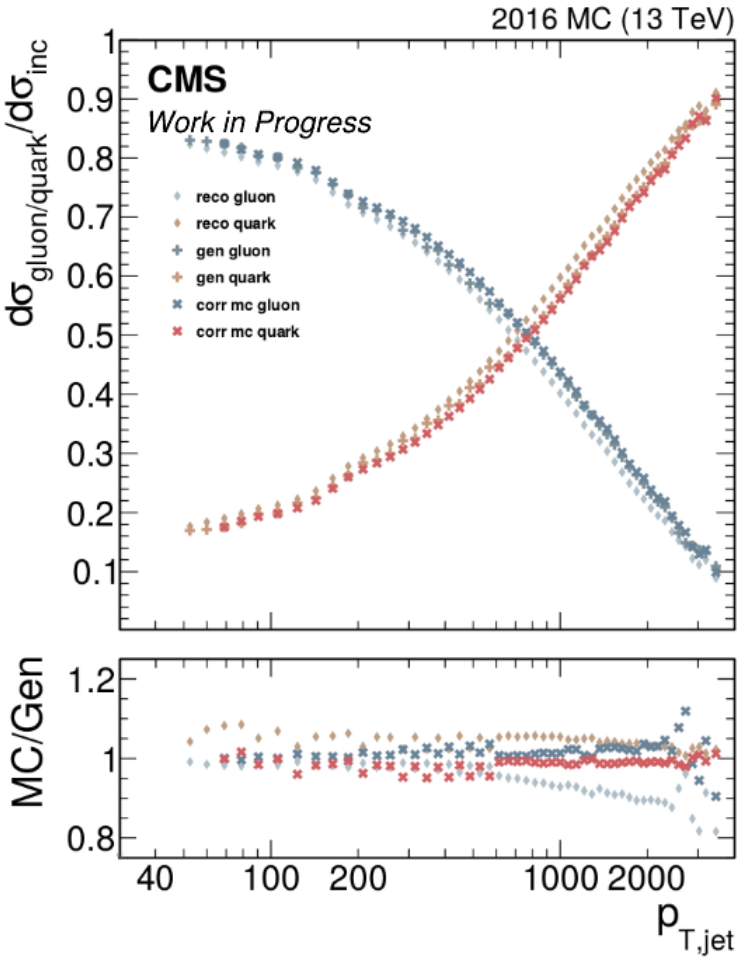


Figure 5.22. Quark gluon jet ratio histograms for MC only

Similarly, the correction factors shown in Figure 5.21, created with the help of response matrices, were applied to the collision data. In Figure 5.23, the unfolded measured jet values and the corrected simulation values are compared with the help of quark gluon jet ratio histograms.

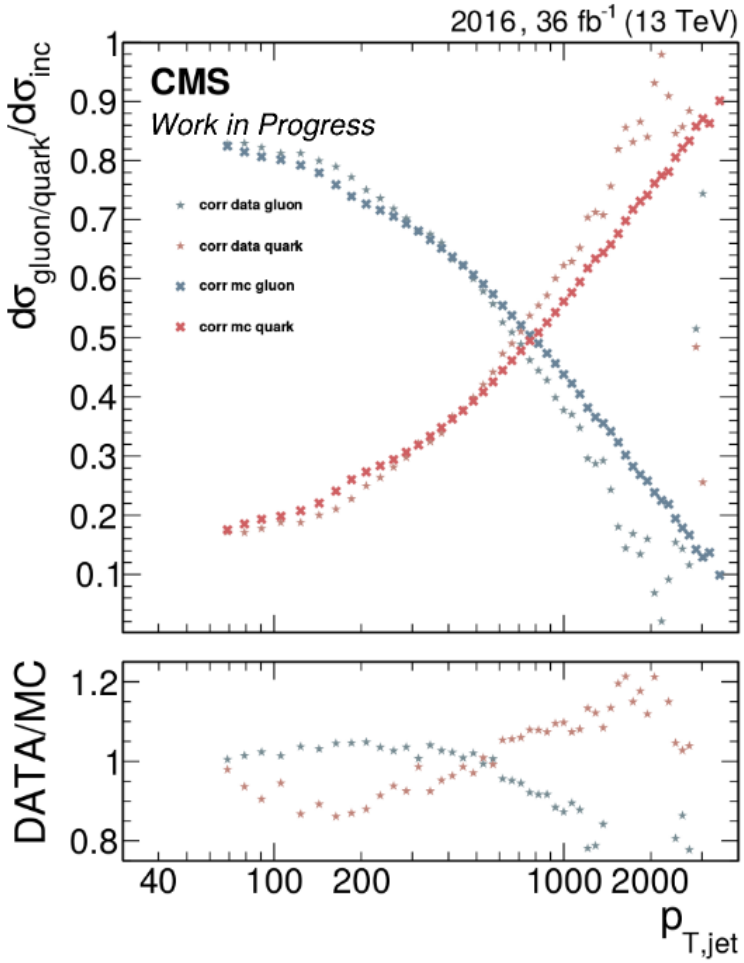


Figure 5.23. Corrected quark gluon jet fraction histograms and ratio histogram for DATA/MC.

5.7. Cross-Section Calculation

The second-order differential jet cross-section is a necessary quantity to be compared with observable physics phenomena and theoretical calculations. After the jet criteria are met, the second order differential jet cross section can be given as a function depending on jet p_T and rapidity.

$$\frac{d^2\sigma}{dP_T d_y} = \frac{1}{L_{int}\varepsilon}\frac{N_{jets}}{\Delta P_T\, \Delta y} \tag{5.10}$$

Where N_{jets} is jet number, ε is jet and incident efficiency, L_{int} is total luminosity, ΔP_T is transverse momentum, and Δy is rapidity.

Figure 5.24 shows the total gluon cross section for the barrel region for MC and DATA. In addition, the MC/DATA ratio obtained from this measurement is shown as well. Here, light red filled icons show data, black line histogram shows MC.

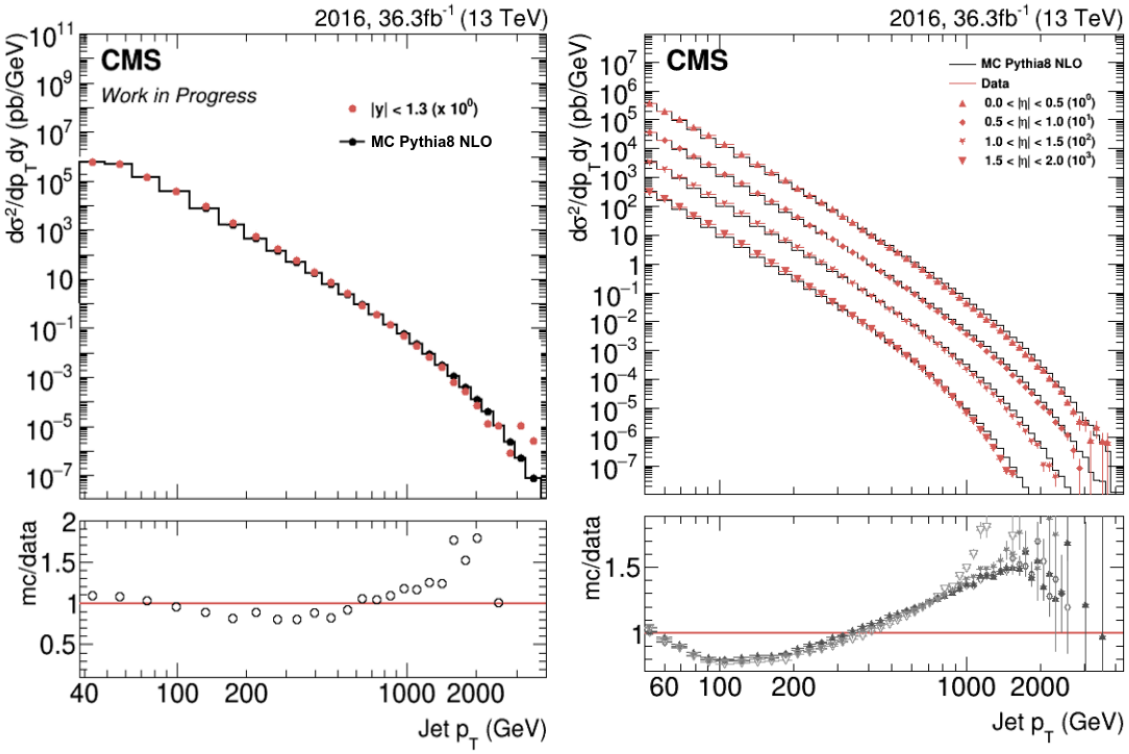


Figure 5.24. Total gluon cross section for the barrel region (left) and jet cross sections up to |y|< 2.0 region (right)

5.8. Systematic Uncertainties

Analyzes are always displayed with uncertainty calculations. There are multiple parameters that affect the measurement uncertainty. In gluon jet measurements, these parameters result from, QGL scale factors, jet energy scale corrections (JES), jet energy resolutions (JER) and luminosity uncertainties.

QGL uncertainties: The most important uncertainty contribution to gluon cross-section measurements is the uncertainties created by the QGL scale factors (SF). Template Fit, which we use to better define the data, calculates gluons by applying these scale factors obtained from Z+jets and Dijet measurements to the gluon QGL distributions. For this reason, the uncertainty affecting the calculations essentially depends on the QGL scale factors for gluons. These uncertainties were defined as half the difference in the template

fit results obtained using SF-applied and unapplied gluon QGL. These differences were used as up-and-down uncertainties.

$$\sigma_{QGL} = \frac{|\, fit_{wgluon} - fit \,|}{2\, fit_{wgluon}} \tag{5.11}$$

QGL Uncertainties are obtained by using the equation 5.11 shown as yellow shaded areas in the Figure 5.25. for each QGL bin on the template fit. Then, the gluon fractions were measured for these maximum and minimum uncertainties of the template fit. Thus, the uncertainties affecting the Gluon cross-section, QGL Uncertainties, were calculated.

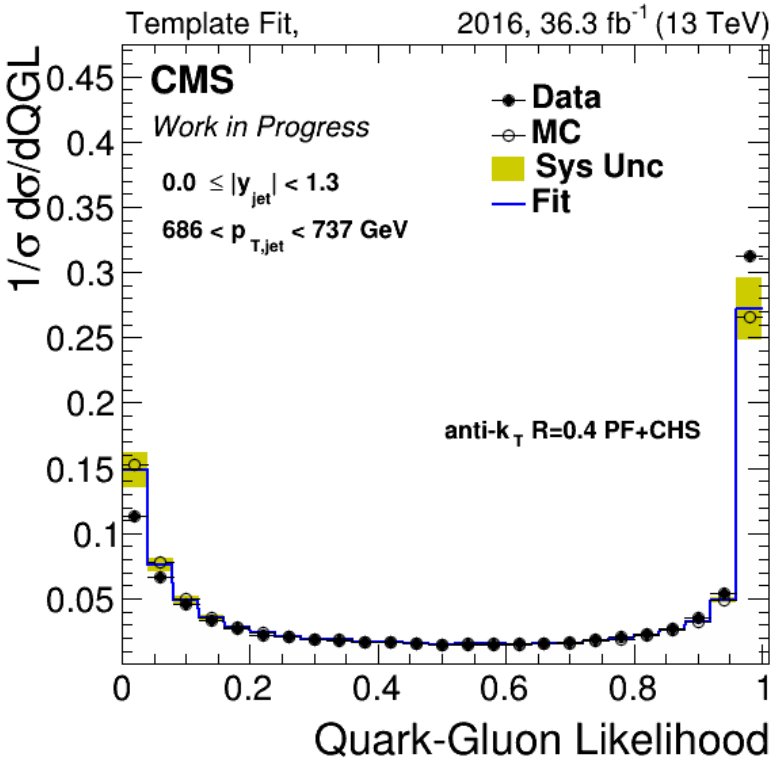


Figure 5.25. Template Fit with Systematic Uncertainties

Jet energy scale uncertainties: The next greatest uncertainties in jet measurements come from JES. The products that create these uncertainties are divided into 4 groups as absolute jet energy, relative jet energy, pile-up jet energy and jet-flavor energy products. The uncertainties brought by these multiplications were calculated for each and calculated as the JES uncertainty.

Jet energy resolution uncertainties: Another major measurement uncertainty arises from the unfolding calculation based on detector resolution. Unfolding calculations

introduce uncertainty into the measurement as much as the JER resolution, as it is basically the approximation of the measurements to their true value. Unfolding calculation is changed by the value of JER and the maximum and minimum contributions are calculated and uncertainties are removed.

Luminosity uncertainties: During the data acquisition process, the luminosity values may differ, and these values are shared with the groups together with their uncertainties. We also used these uncertainties in our analysis because we made cross-section calculations.

Total experimental uncertainties: QGL, JES, JER and Luminosity uncertainties are calculated by summing them all as follows.

$$\sigma^{total} = \sqrt{\sigma^2_{QGL} + \sigma^2_{JES} + \sigma^2_{JER} + \sigma^2_{lumi}} \tag{5.12}$$

These uncertainties calculated for the inclusive jets in the analysis are given in Figure 5.26.

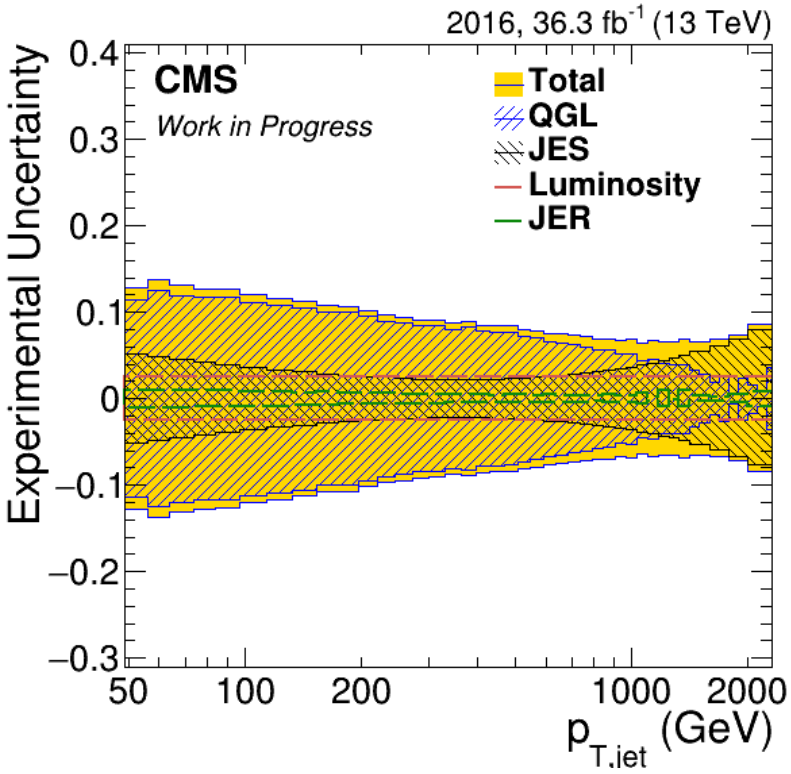


Figure 5.26. Total uncertainties for the cross section of the inclusive jets

The purple dashed line is the Luminosity uncertainty and is 2.5% [36]. The green dashed color indicates JER uncertainty and is about 1%. The black shaded region indicates the JES uncertainties, which is dominant in the analysis around higher p_T values and is approximately 8.5%. The blue shaded region indicates the QGL uncertainties dominating lower p_T values and is approximately 12-14%.

6. CONCLUSIONS

We measured the gluon jets from inclusive multi jets and applied unfolding routines for the first time in this thesis. The measured gluon-initiated jets having p_T bigger than 49 GeV were searched for the barrel region of CMS corresponding rapidity bin y < |1.3|. While performing these measurements, inclusive multi jets were also measured for the rapidity bins up to |2.0|. However, its details were not included as it was not the main subject of this thesis. This study was conducted with data from proton-proton collisions with 13TeV energy generated by the LHC and collected by the CMS detector. The corresponding luminosity to this data is 36.3 inverse femtobarn.

To obtain the gluon jets, a likelihood discriminator QGL was developed and used to differentiate the jets originating from quarks and gluons, since the quark and gluon jet shapes are well defined at the detector level as they are shown in the thesis. Systematic uncertainties were calculated, including the uncertainties arising from the QGL discrimination method. Comparisons were performed with the results obtained from the Pythia8 simulation at the NLO level.

This Gluon jet measurement, with lower uncertainties at higher jet p_T, marks the process towards a better understanding of jets which will enhance searches for novel physics as well as the assessment of standard-model signs and backgrounds.

7. REFERENCES

[1] Griffiths, D. (2008) Introduction to Elementary Particles. 2nd Edition, Wiley-VCH, Weinheim.

[2] Klaus, R. (2017) Jet Physics at the LHC The Strong Force beyond the TeV Scale, Springer International Publishing. Volume 268.

[3] Luciano Maiani and Luigi Rolandi, (2016) The Standard Theory of Particle Physics Essays to Celebrate CERN's 60th Anniversary. Volume 26.

[4] R.L. Workman et al. (Particle Data Group), (2022) Prog. Theor. Exp. Phys., 083C01.

[5] William Gary, J., (1999), Determination of the QCD color factor ratio CA/CF from the scale dependence of multiplicity in three jet events, Physical Review D, 61, 114007.

[6] https://www.nobelprize.org/prizes/physics/2004/summary/, Accessed in 2022.

[7] R. Keith Ellis, (2016) Quantum Chromodynamics and Deep Inelastic Scattering, Adv. Ser. Direct. High Energy Phys. 26 (2016) 61-78

[8] C.J. Maxwell (2006). Perturbative and non-perturbative QCD. Institute for Particle Physics Phenomenology (IPPP), Durham University, U.K.

[9] H. David Politzer (1973). Reliable Perturbative Results for Strong Interactions. Physical Review Letters, 30 (1973) 1346-1349.

[10] A.D. Martin, W.J. Stirling, R.S. Thorne, G. Watt, (2019). Parton distributions for the LHC, Eur.Phys.J.C63:189-285.

[11] Lyndon Evans, and Philip Bryant (2008). LHC Machine, THE CERN Large Hadron Collider: Accelerator and Experiments, JINST 3 S08001.

[12] https://lhc-commissioning.web.cern.ch/schedule/LHC-long-term.htm, Accessed in 2023.

[13] https://twiki.cern.ch/twiki/bin/view/CMSPublic/LumiPublicResults, Accessed in 2023.

[14] G. Aad et al., (2008). The ATLAS Experiment at the CERN Large Hadron Collider, JINST, vol. 3, p.8003.

[15] S. Chatrchyan et al., (2008). The CMS Experiment at the CERN LHC, JINST, vol. 3, p. S08004.

[16] Anellietal., (2008). The TOTEM experiment at the CERN Large HadronCollider, JINST, vol. 3, p. S08007.

[17] A. A. Alves, Jr. et al., (2008). The LHCb Detector at the LHC, JINST, vol. 3, p. S08005.

[18] K. Aamodt et al., (2008) "The ALICE experiment at the CERN LHC," JINST, vol. 3, p. S08002.

[19] C. De Melis, "The CERN accelerator complex. Complexe des accélérateurs du CERN," Jul 2016. General Photo, https://cds.cern.ch/record/ 2684277, Accessed in 2023.

[20] CMS detector figures: https://cms.cern/detector, Accessed in 2023.

[21] V. Karimaki, M. Mannelli, P. Siegrist, H. Breuker, A. Caner, R. Castaldi, K. Freudenreich, G. Hall, R. Horisberger, M. Huhtinen, and A. Cattai (1997). The CMS tracker system project: Technical Design Report. Technical Design Report CMS, Geneva: CERN.

[22] The CMS Collaboration (2014). Alignment of the CMS tracker with LHC and cosmic ray data. Journal of Instrumentation, 9(06): P06009.

[23] https://cms.cern/detector/measuring-energy/ energy-electrons-and-photons-ecal, Accessed in 2023.

[24] The CMS Collaboration (1997). The CMS electromagnetic calorimeter project: Technical Design Report. Technical Design Report CMS, Geneva: CERN.

[25] The CMS Collaboration (2012). Observation of a new boson at a mass of 125 GeV with the CMS experiment at the LHC, Phys. Lett. B 716 (2012) 30.

[26] The CMS Collaboration (1997). The CMS Hadron Calorimeter project: Technical Design Report. Technical Design Report CMS, Geneva: CERN.

[27] Bayatian et al., (2008). Design, performance and calibration of the CMS forward calorimeter wedges, Eur. Phys. J., vol. C53, pp. 139–166.

[28] G. Acquistapace et al., (1997). CMS, The Magnet Project: Technical Design Report.

[29] The CMS Collaboration (1997). The CMS muon project: Technical Design Report. Technical Design Report CMS, Geneva: CERN.

[30] The CMS Collaboration (2000). CMS. The TriDAS project. Technical Design Report, vol. 1: The trigger systems.

[31] Cittolin, Sergio, Rácz, Attila, Sphicas, Paris (2002). CMS The TriDAS Project: Technical Design Report, Volume 2: Data Acquisition and High-Level Trigger.

[32] The CMS Collaboration (2008). The CMS experiment at the CERN LHC JINST 3 S08004.

[33] The CMS Collaboration (2017). Particle-flow reconstruction and global event description with the CMS detector JINST 12 P10003

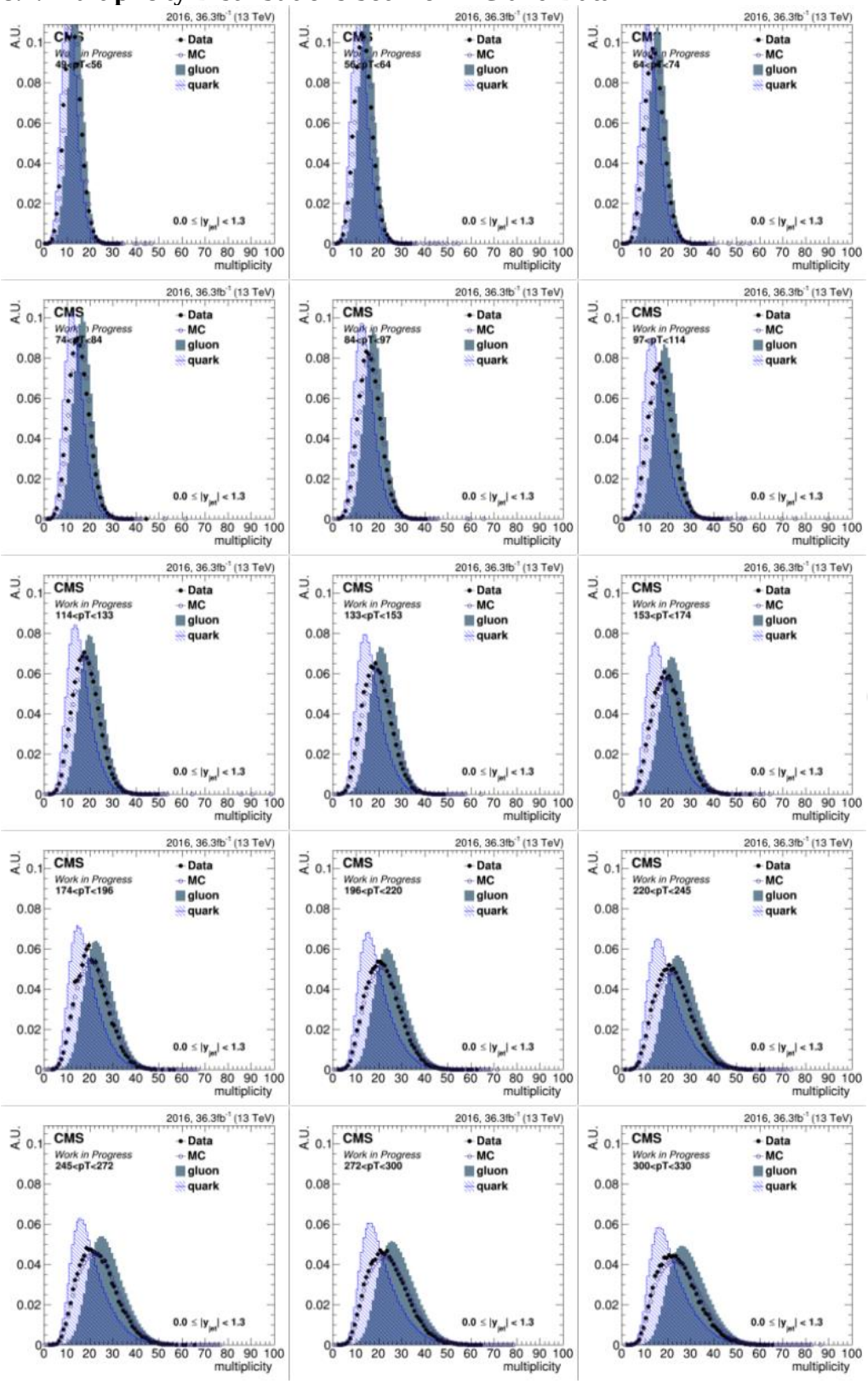
[34] https://twiki.cern.ch/twiki/bin/viewauth/CMS/JECDataMC#Jet_veto_maps, Accessed in 2023.

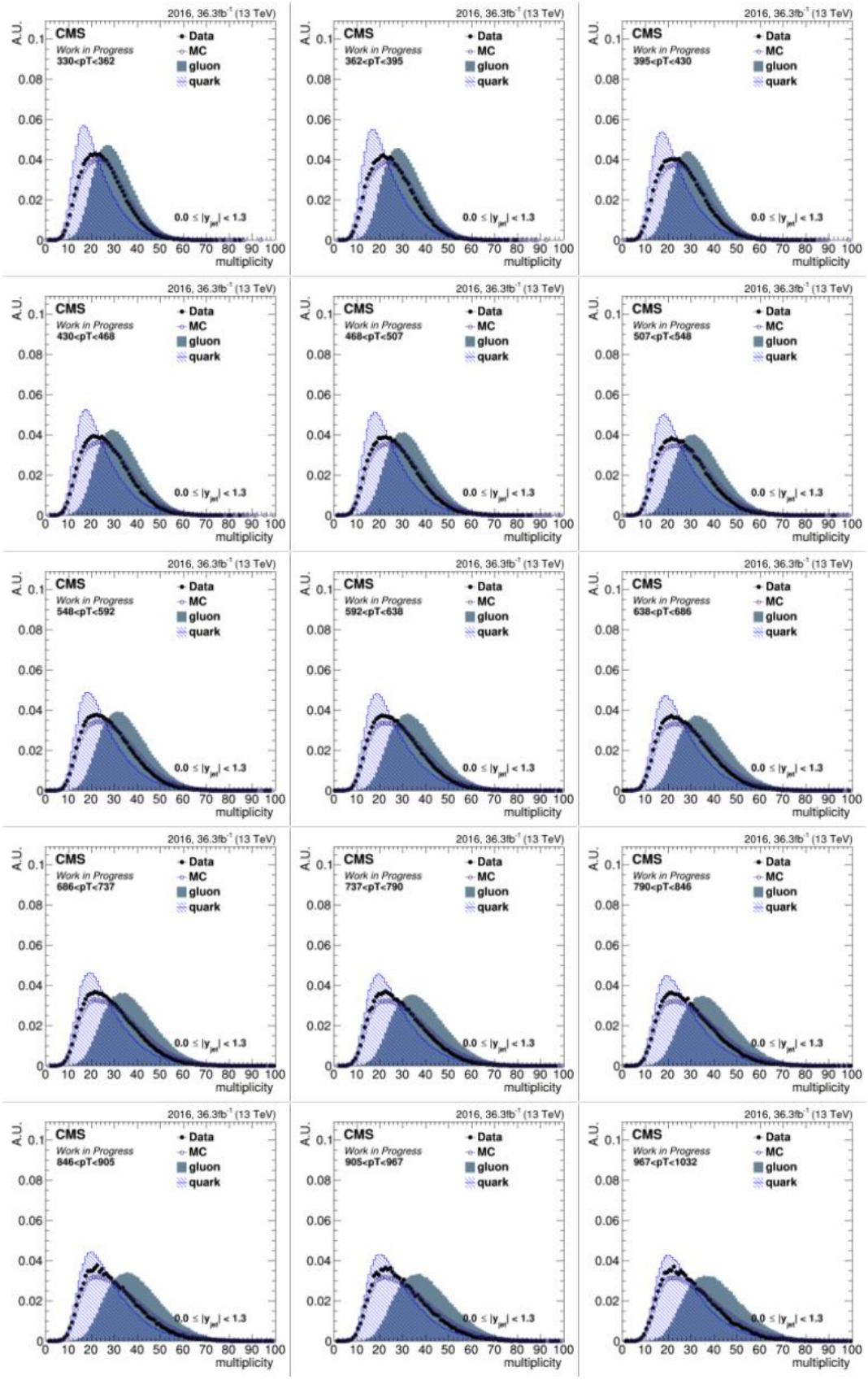
[35] https://twiki.cern.ch/twiki/bin/viewauth/CMS/L1PrefiringWeightRecipe#Jet_prefiring_maps_per_IOV_E_AN1, Accessed in 2023.

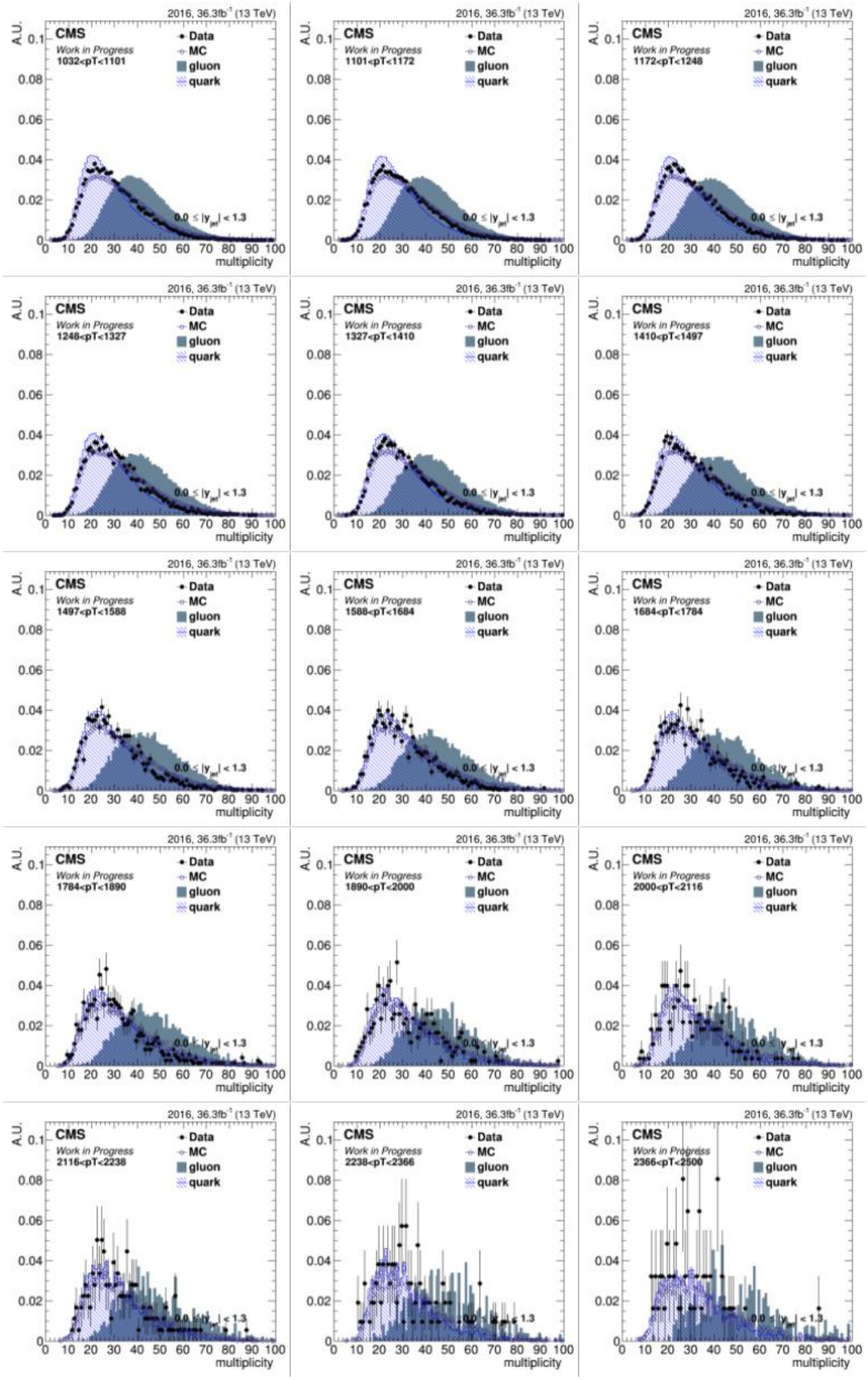
[36] CMS Collaboration. (2017). CMS Luminosity Measurements for the 2016 Data Taking Period. CMS-PAS-LUM-17-001

8. APPENDIX

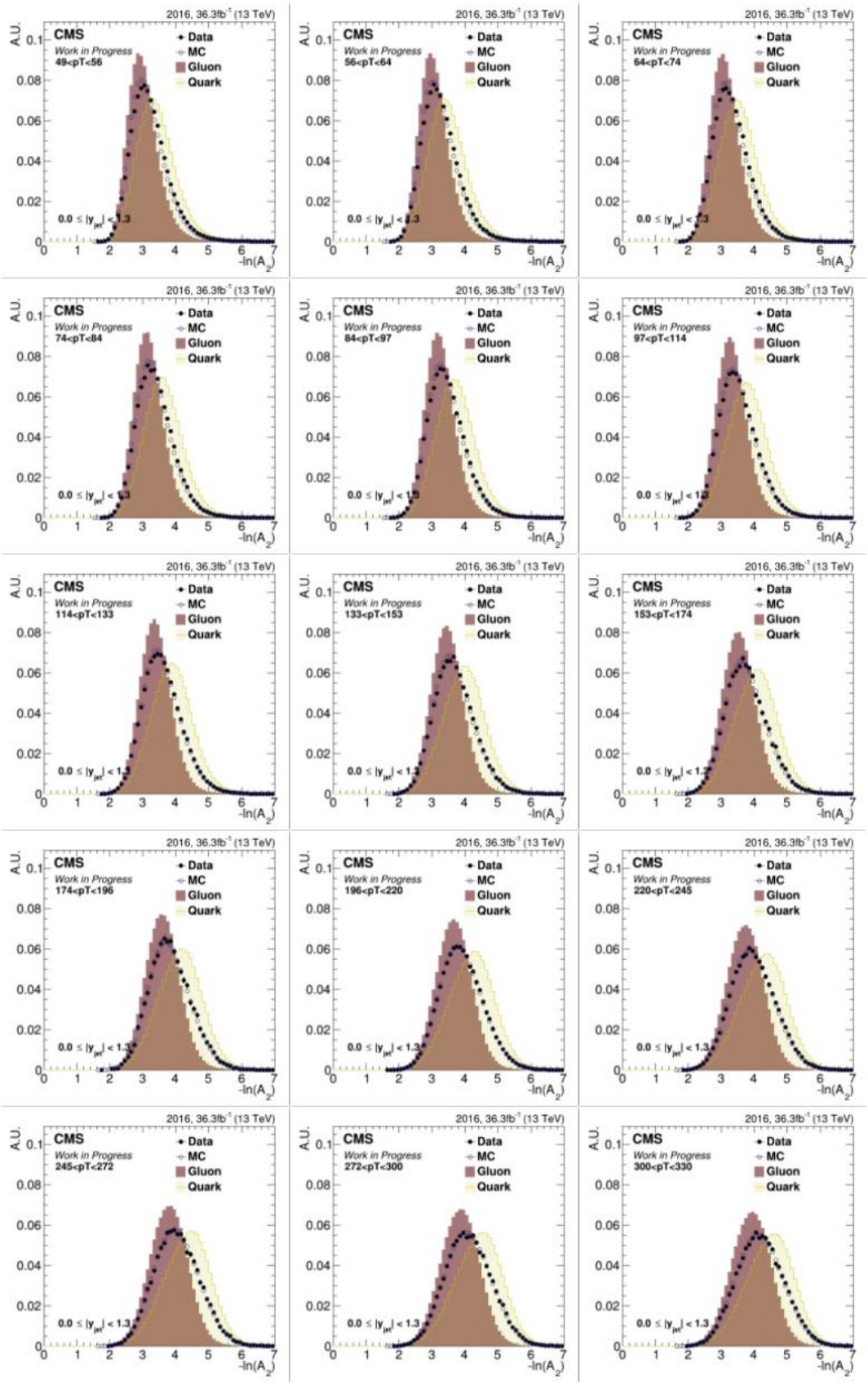
8.1. Multiplicity Distributions both for MC and Data

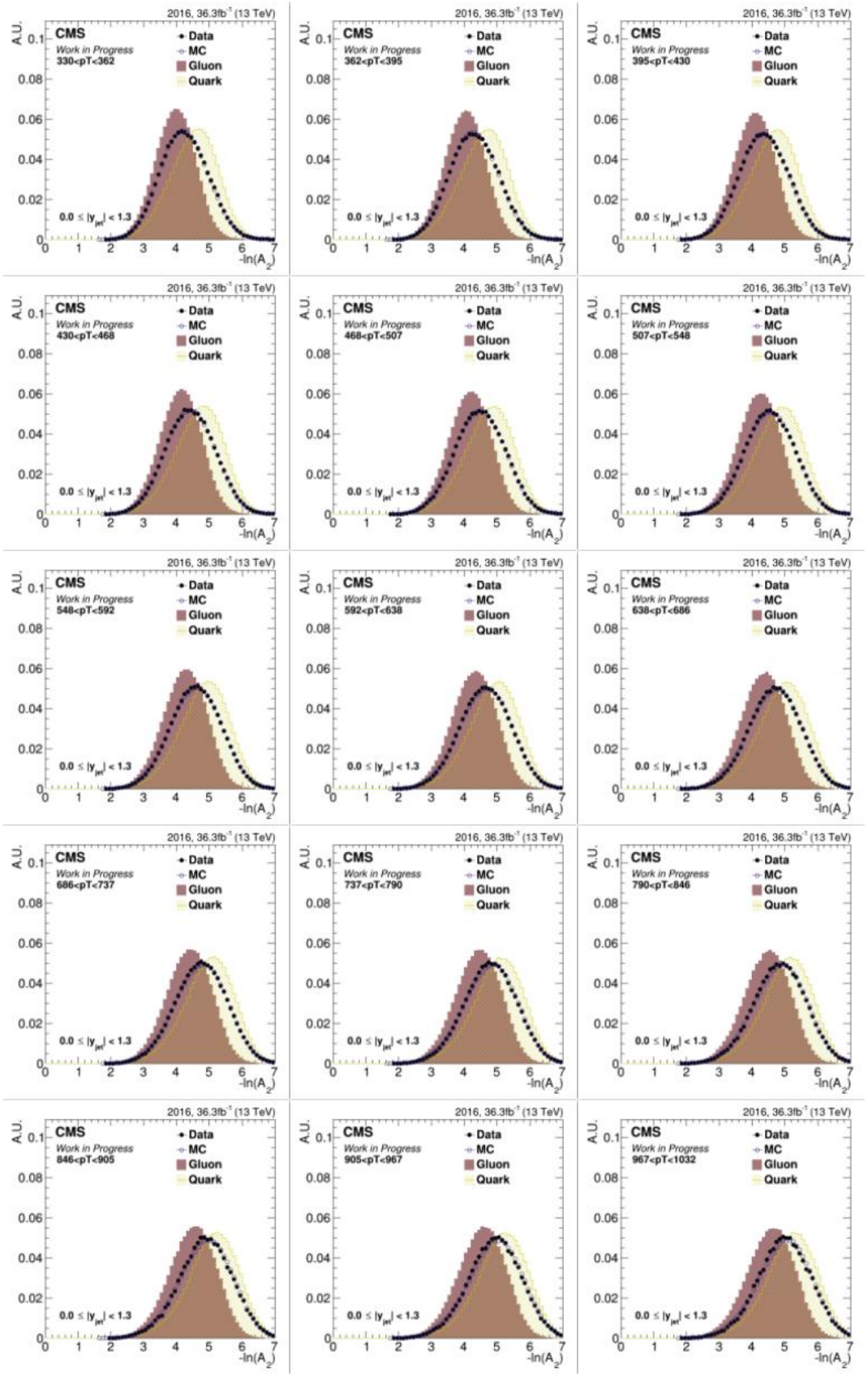


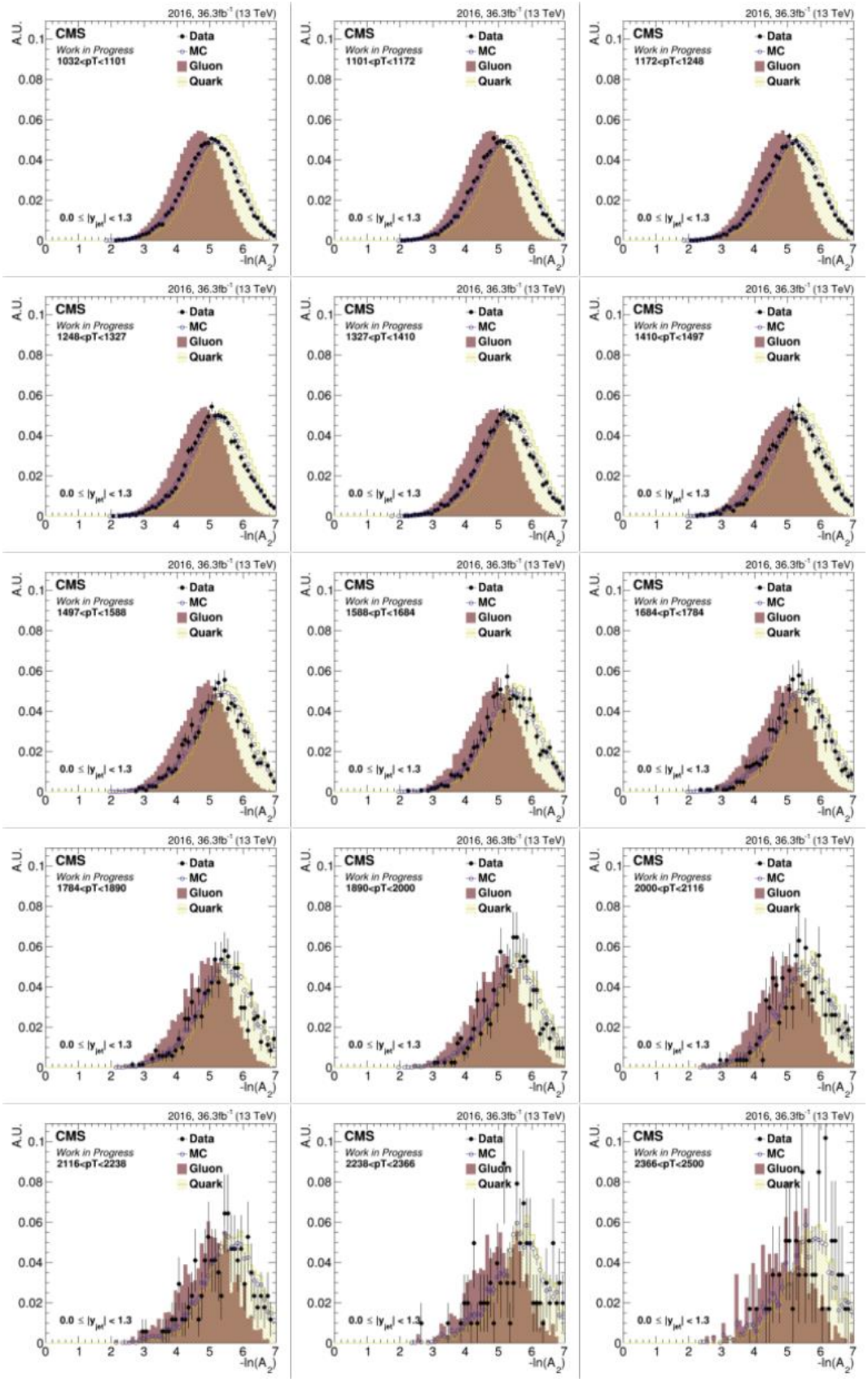

2016, 36.3fb^{-1} (13 TeV)
CMS
Work in Progress
330<pT<362
362<pT<395
395<pT<430
430<pT<468
468<pT<507
507<pT<548
548<pT<592
592<pT<638
638<pT<686
686<pT<737
737<pT<790
790<pT<846
846<pT<905
905<pT<967
967<pT<1032
Data
MC
gluon
quark
0.0 ≤ |y$_{jet}$| < 1.3
A.U.
multiplicity


2016, 36.3fb^{-1} (13 TeV)
CMS
Work in Progress
1032<pT<1101
1101<pT<1172
1172<pT<1248
1248<pT<1327
1327<pT<1410
1410<pT<1497
1497<pT<1588
1588<pT<1684
1684<pT<1784
1784<pT<1890
1890<pT<2000
2000<pT<2116
2116<pT<2238
2238<pT<2366
2366<pT<2500
Data
MC
gluon
quark
A.U.
multiplicity
0.0 ≤ |y$_{jet}$| < 1.3

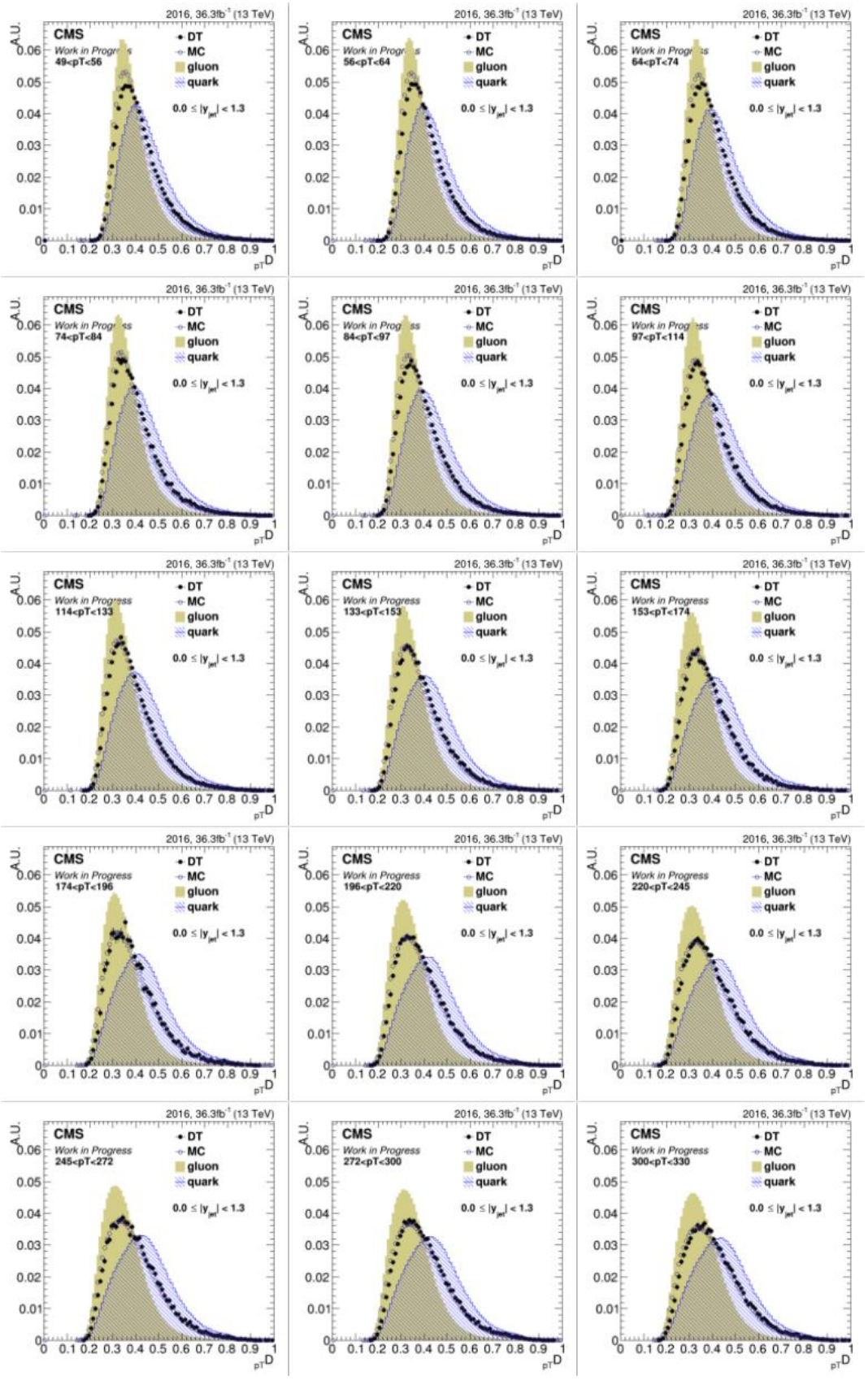
8.2. Minor Axis 2 Distributions both for MC and Data

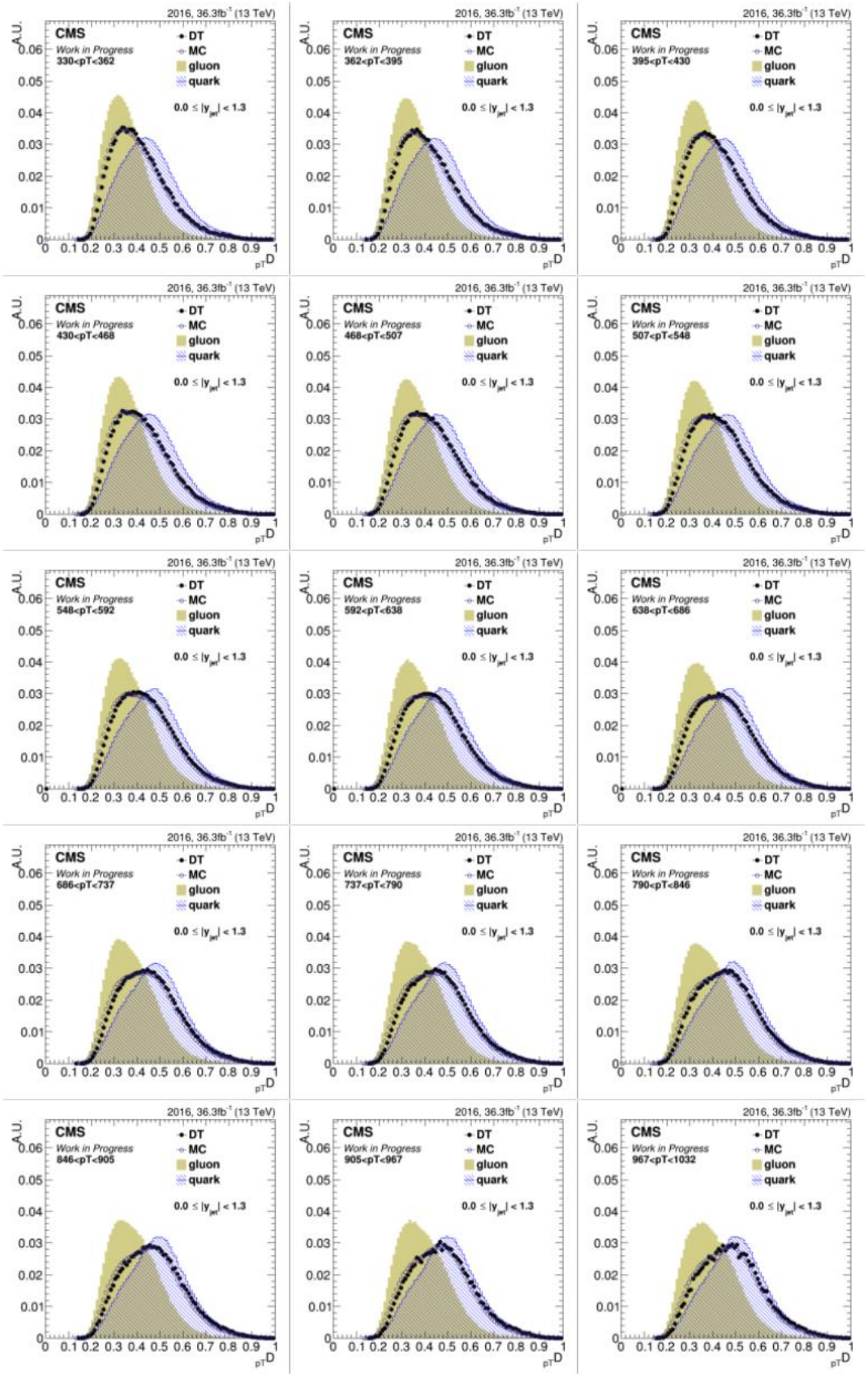


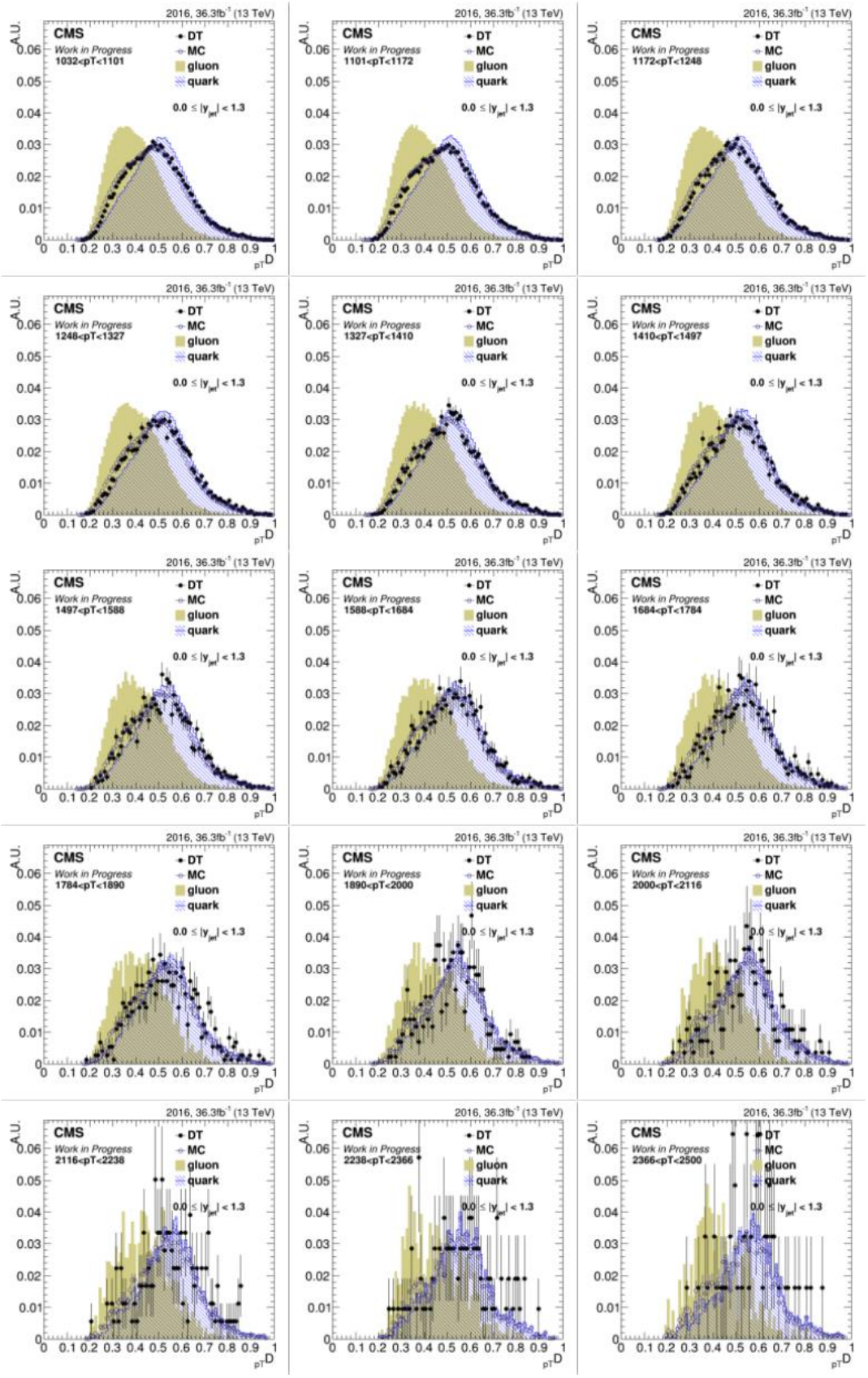

2016, 36.3fb^{-1} (13 TeV)
CMS
Work in Progress
330<pT<362
362<pT<395
395<pT<430
430<pT<468
468<pT<507
507<pT<548
548<pT<592
592<pT<638
638<pT<686
686<pT<737
737<pT<790
790<pT<846
846<pT<905
905<pT<967
967<pT<1032
Data
MC
Gluon
Quark
0.0 ≤ |y$_{jet}$| < 1.3
A.U.
-ln(A$_2$)


2016, 36.3fb^{-1} (13 TeV)
CMS
Work in Progress
1032<pT<1101
1101<pT<1172
1172<pT<1248
1248<pT<1327
1327<pT<1410
1410<pT<1497
1497<pT<1588
1588<pT<1684
1684<pT<1784
1784<pT<1890
1890<pT<2000
2000<pT<2116
2116<pT<2238
2238<pT<2366
2366<pT<2500
Data
MC
Gluon
Quark
0.0 ≤ |y$_{jet}$| < 1.3
A.U.
-ln(A$_2$)

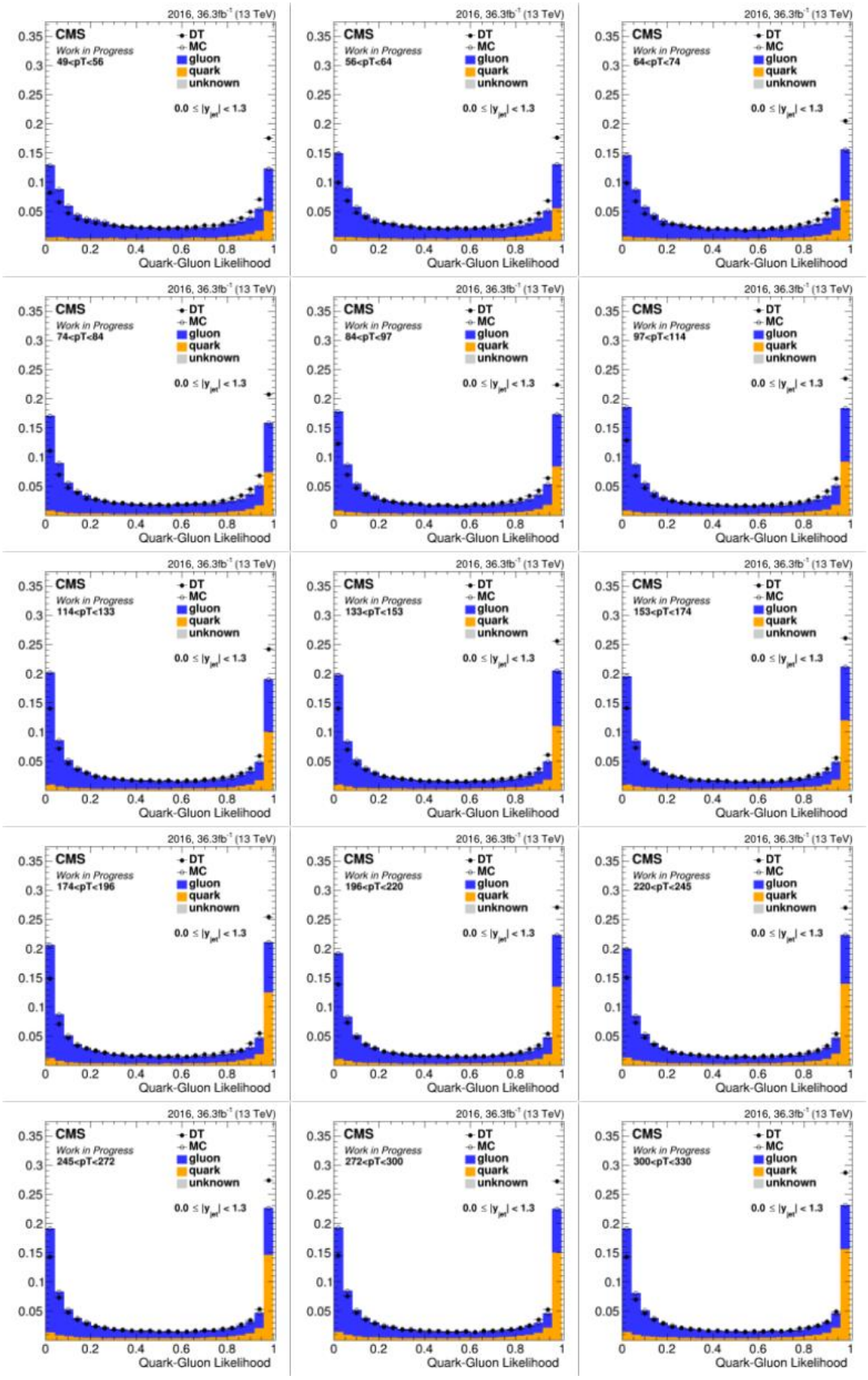
8.3. $p_T D$ Distributions both for MC and Data

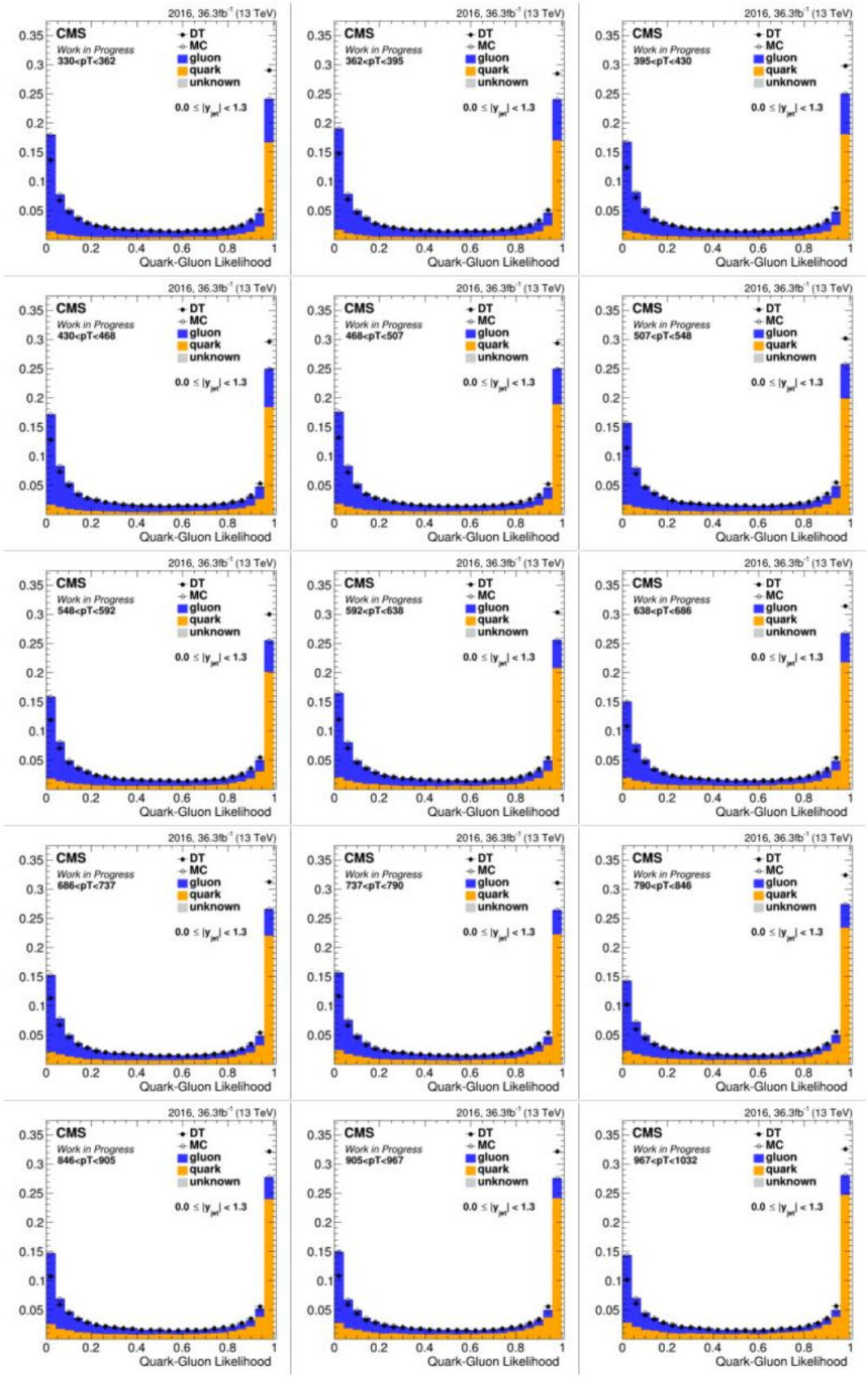


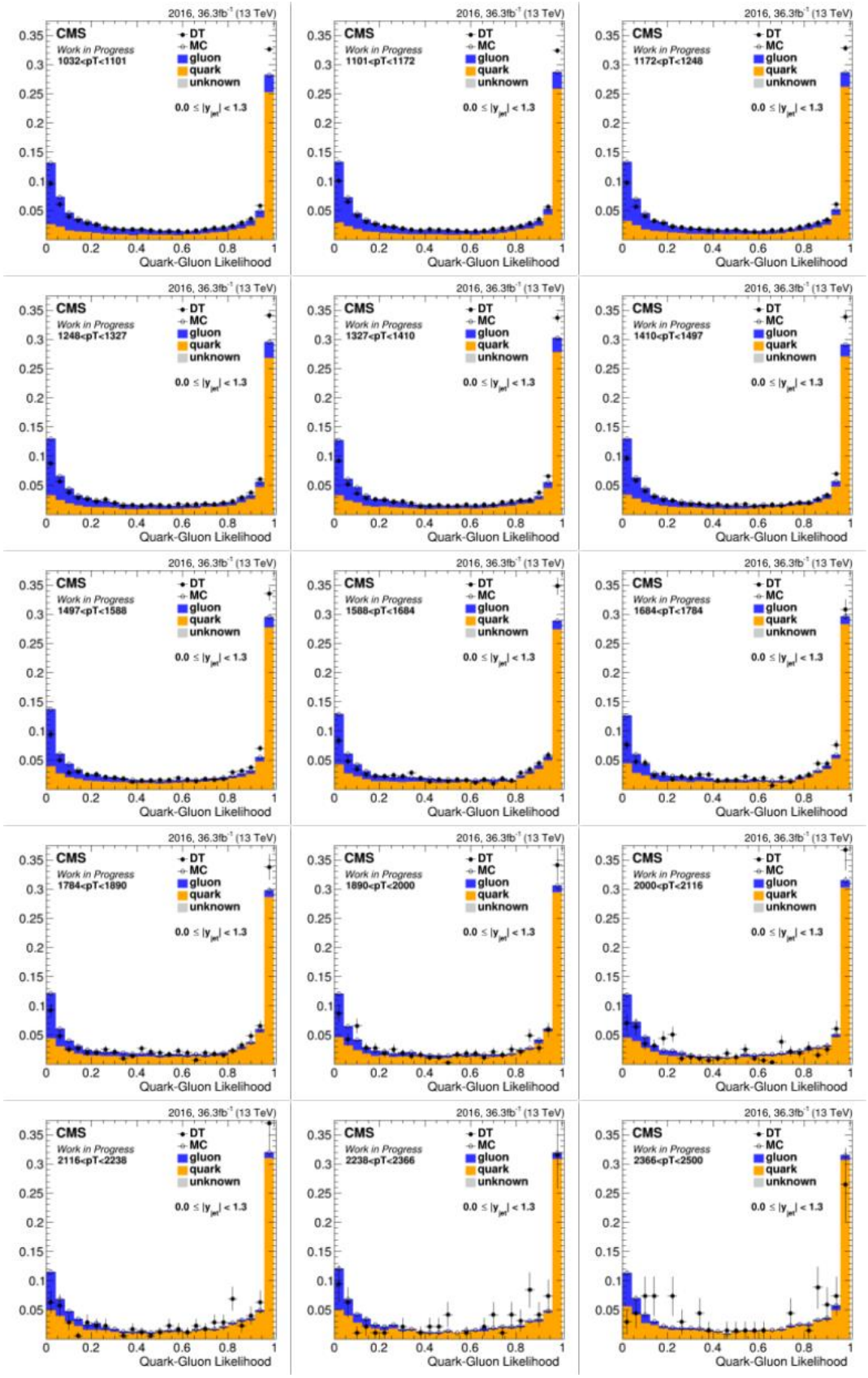

2016, 36.3fb^{-1} (13 TeV)
CMS
Work in Progress
330<pT<362
362<pT<395
395<pT<430
430<pT<468
468<pT<507
507<pT<548
548<pT<592
592<pT<638
638<pT<686
686<pT<737
737<pT<790
790<pT<846
846<pT<905
905<pT<967
967<pT<1032
DT
MC
gluon
quark
0.0 ≤ |y$_{jet}$| < 1.3
A.U.
$_{pT}$D


2016, 36.3fb^{-1} (13 TeV)
CMS
Work in Progress
1032<pT<1101
1101<pT<1172
1172<pT<1248
1248<pT<1327
1327<pT<1410
1410<pT<1497
1497<pT<1588
1588<pT<1684
1684<pT<1784
1784<pT<1890
1890<pT<2000
2000<pT<2116
2116<pT<2238
2238<pT<2366
2366<pT<2500
DT
MC
gluon
quark
0.0 ≤ |y$_{jet}$| < 1.3
A.U.
p_T^D

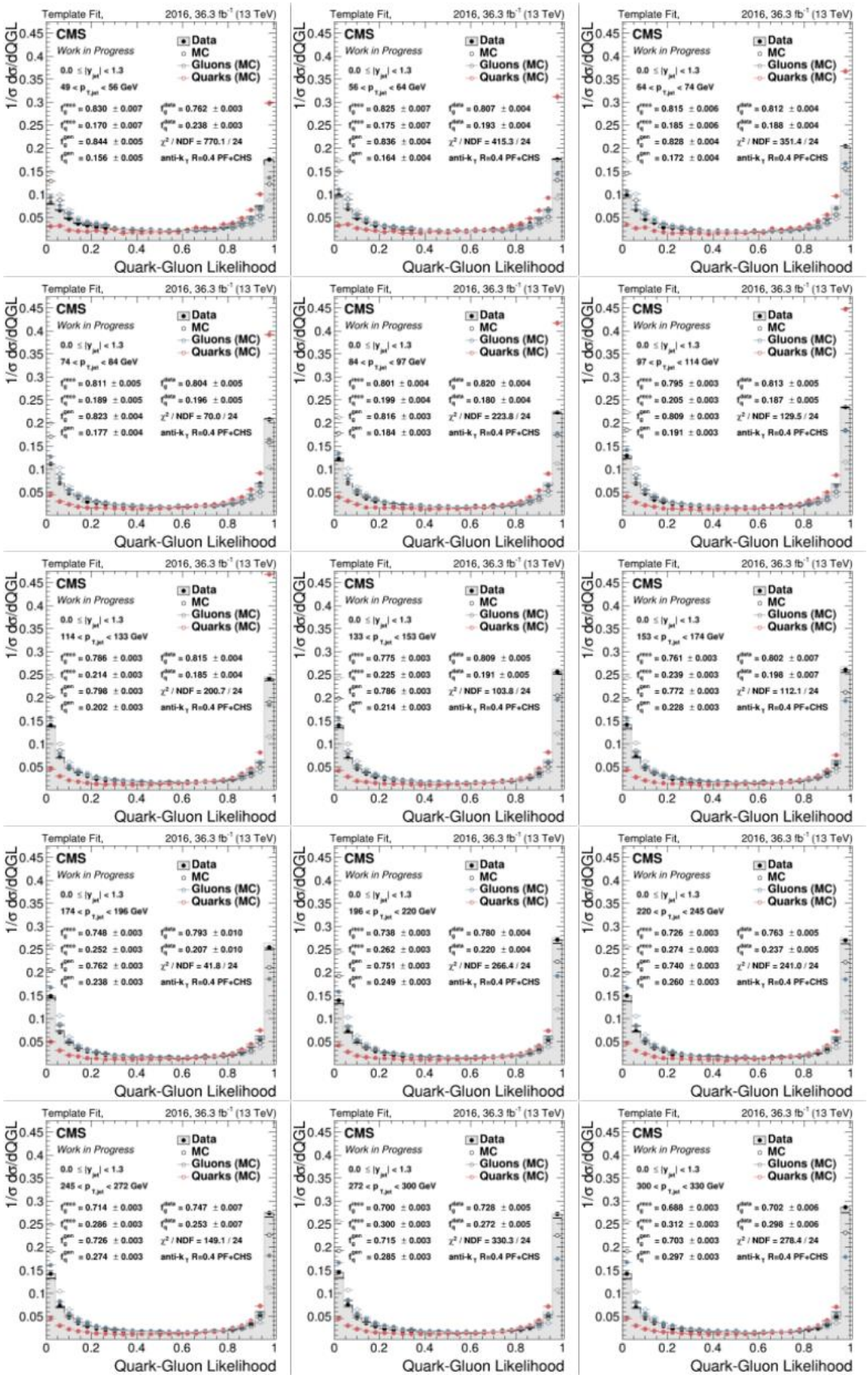
8.4. QGL Distributions both for MC and Data

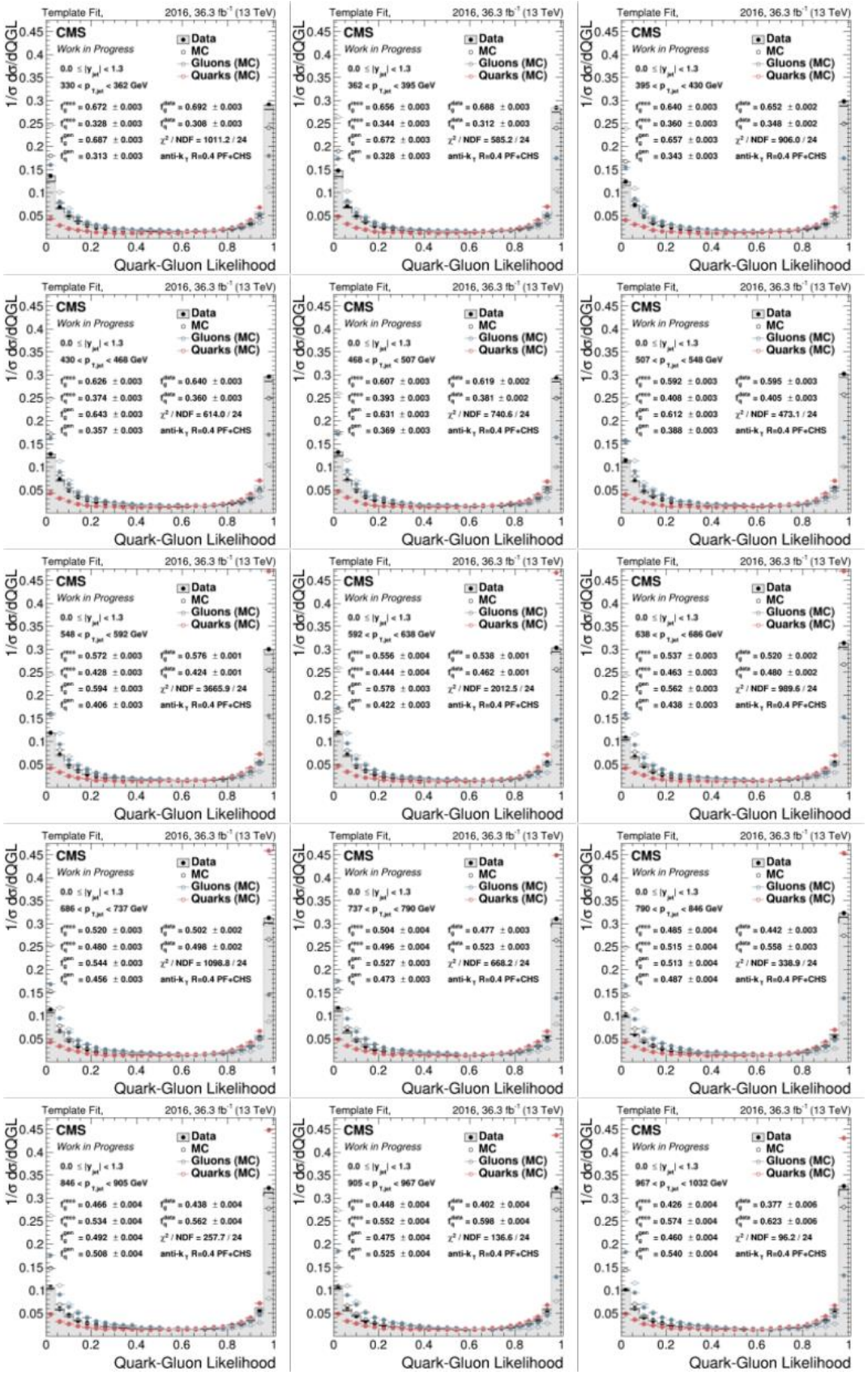


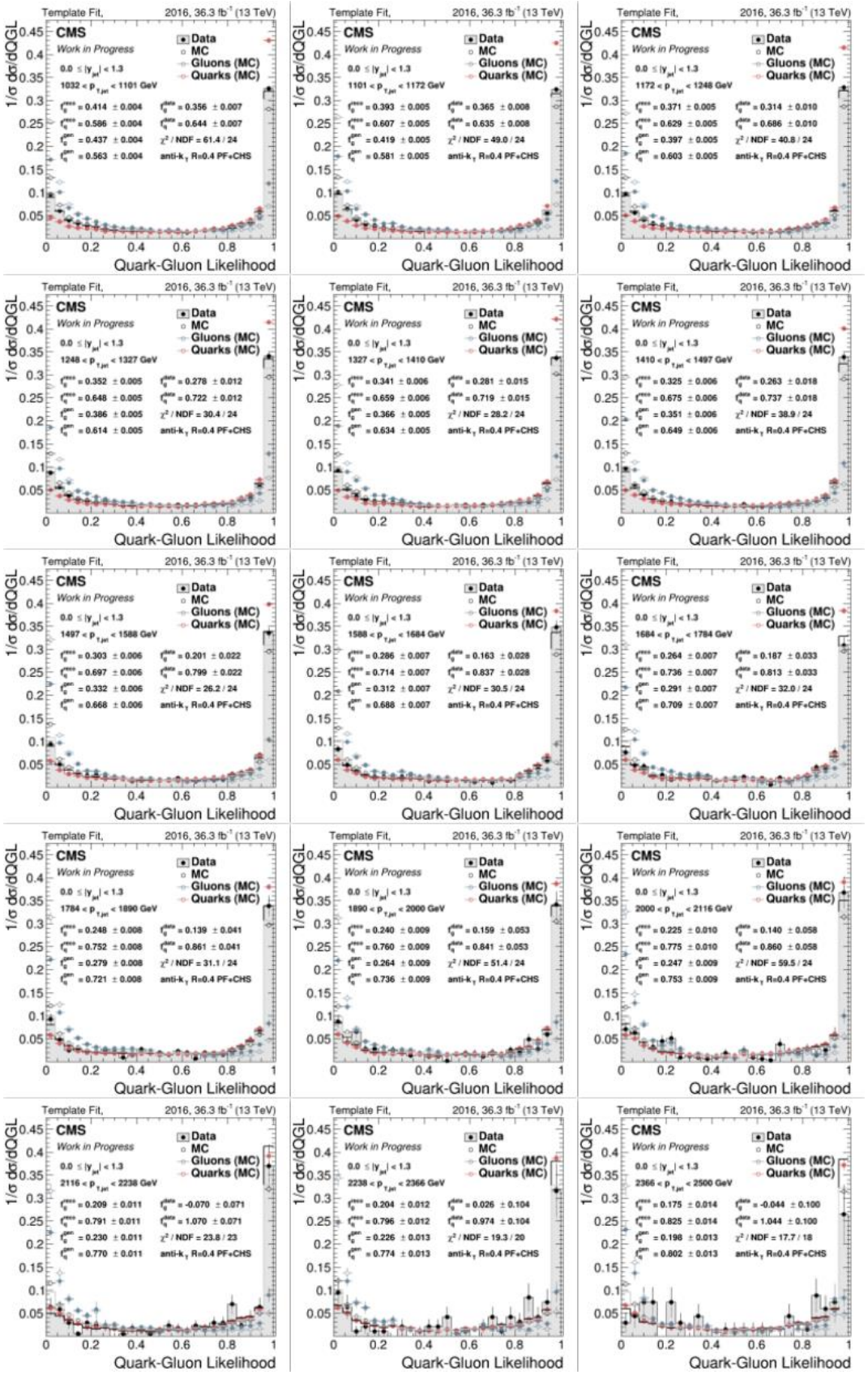

2016, 36.3fb^{-1} (13 TeV)
CMS
Work in Progress
330<pT<362
362<pT<395
395<pT<430
430<pT<468
468<pT<507
507<pT<548
548<pT<592
592<pT<638
638<pT<686
686<pT<737
737<pT<790
790<pT<846
846<pT<905
905<pT<967
967<pT<1032
DT
MC
gluon
quark
unknown
0.0 ≤ |y$_{jet}$| < 1.3
Quark-Gluon Likelihood


2016, 36.3fb^{-1} (13 TeV)
CMS
Work in Progress
1032<pT<1101
1101<pT<1172
1172<pT<1248
1248<pT<1327
1327<pT<1410
1410<pT<1497
1497<pT<1588
1588<pT<1684
1684<pT<1784
1784<pT<1890
1890<pT<2000
2000<pT<2116
2116<pT<2238
2238<pT<2366
2366<pT<2500
DT
MC
gluon
quark
unknown
0.0 ≤ |y$_{jet}$| < 1.3
Quark-Gluon Likelihood

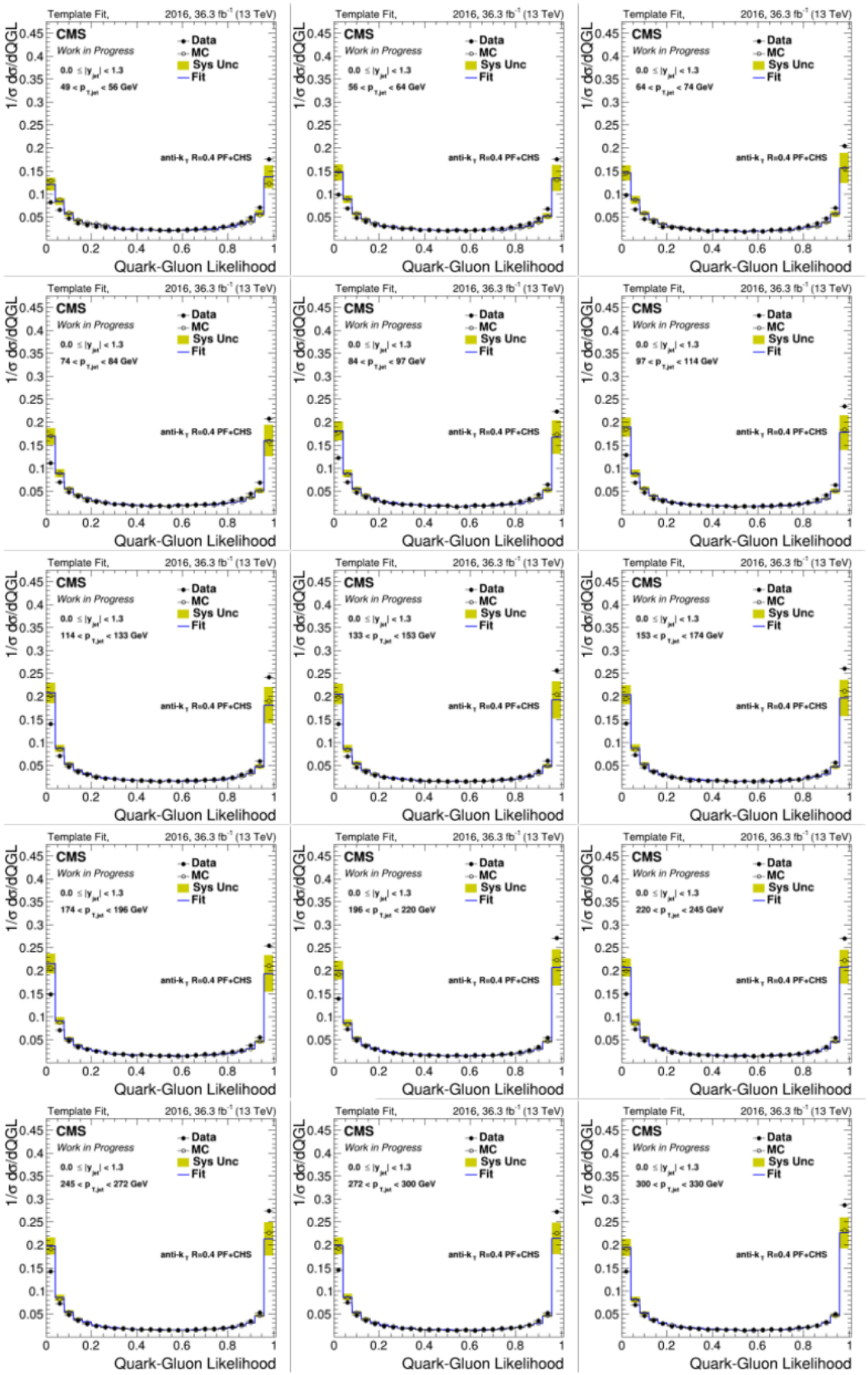
8.5. Template Fit both for MC and Data

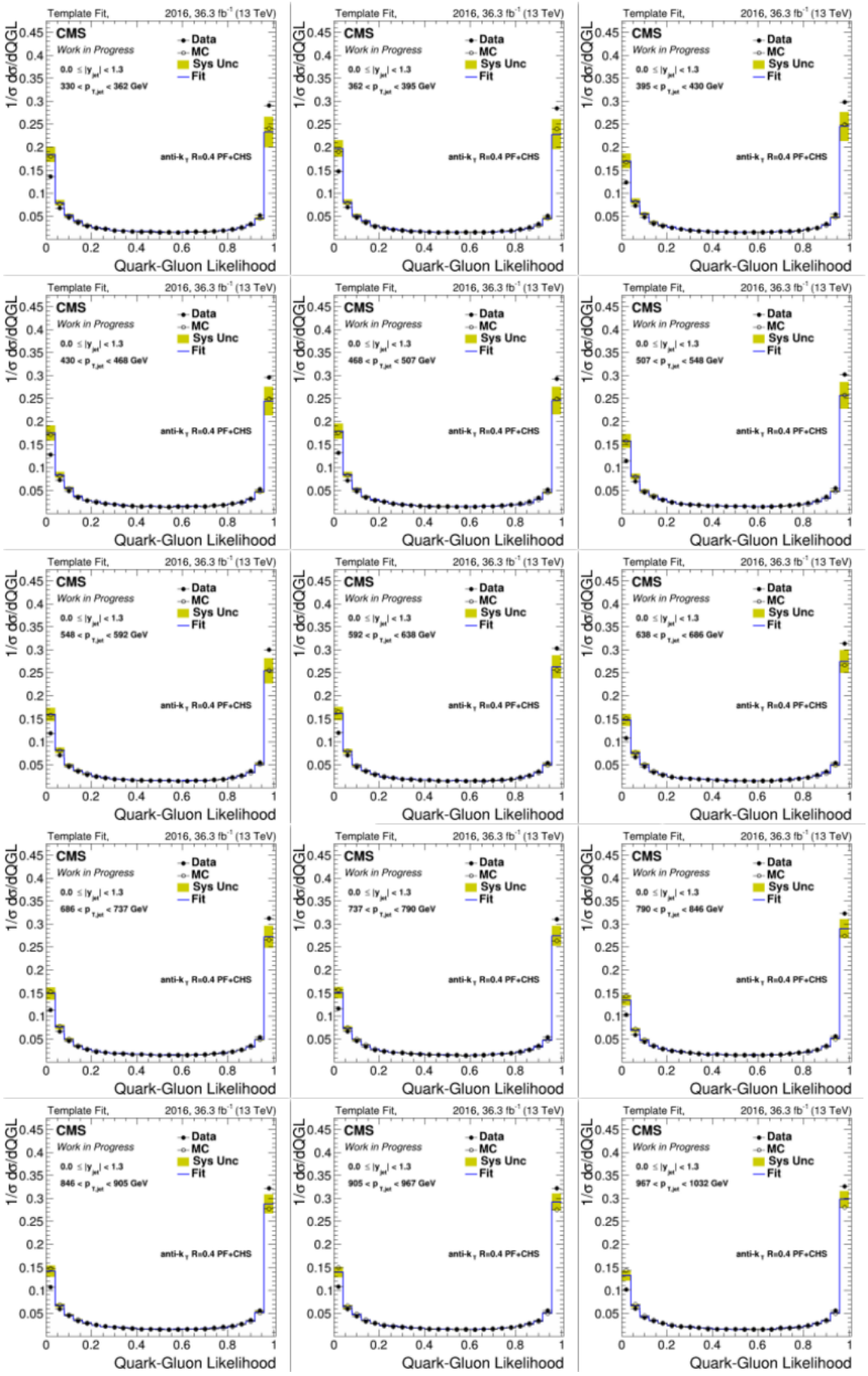


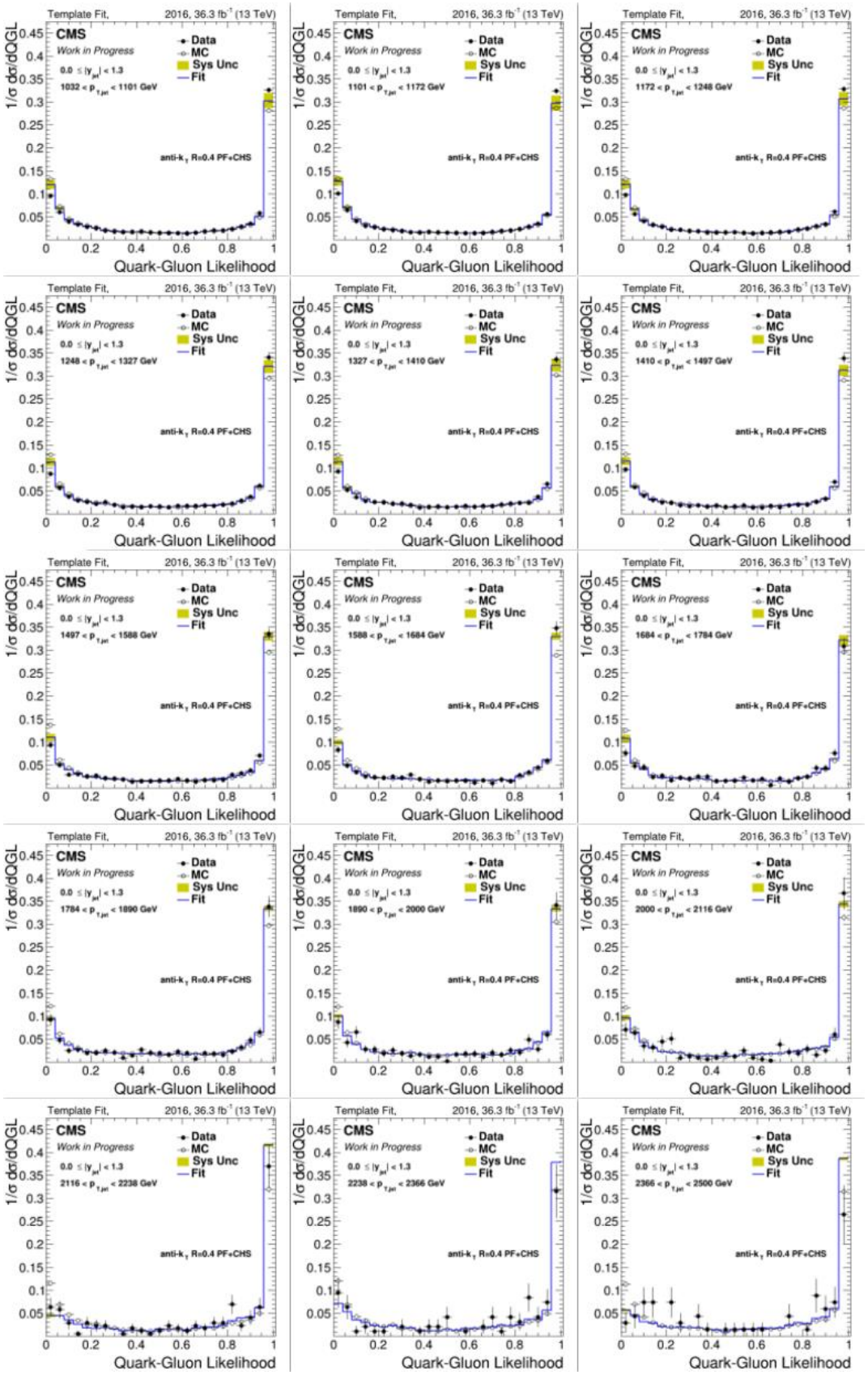

Template Fit, 2016, 36.3 fb^{-1} (13 TeV)
CMS
Work in Progress
Data
MC
Gluons (MC)
Quarks (MC)
0.0 ≤ |y$_{jet}$| < 1.3
330 < p$_{T,jet}$ < 362 GeV
f_g^{data} = 0.672 ± 0.003
f_q^{data} = 0.328 ± 0.003
f_g^{MC} = 0.687 ± 0.003
f_q^{MC} = 0.313 ± 0.003
f_g^{data} = 0.692 ± 0.003
f_q^{data} = 0.308 ± 0.003
χ^2 / NDF = 1011.2 / 24
anti-k$_T$ R=0.4 PF+CHS
362 < p$_{T,jet}$ < 395 GeV
f_g^{data} = 0.656 ± 0.003
f_q^{data} = 0.344 ± 0.003
f_g^{MC} = 0.672 ± 0.003
f_q^{MC} = 0.328 ± 0.003
f_g^{data} = 0.688 ± 0.003
f_q^{data} = 0.312 ± 0.003
χ^2 / NDF = 585.2 / 24
anti-k$_T$ R=0.4 PF+CHS
395 < p$_{T,jet}$ < 430 GeV
f_g^{data} = 0.640 ± 0.003
f_q^{data} = 0.360 ± 0.003
f_g^{MC} = 0.657 ± 0.003
f_q^{MC} = 0.343 ± 0.003
f_g^{data} = 0.652 ± 0.002
f_q^{data} = 0.348 ± 0.002
χ^2 / NDF = 906.0 / 24
anti-k$_T$ R=0.4 PF+CHS
430 < p$_{T,jet}$ < 468 GeV
f_g^{data} = 0.626 ± 0.003
f_q^{data} = 0.374 ± 0.003
f_g^{MC} = 0.643 ± 0.003
f_q^{MC} = 0.357 ± 0.003
f_g^{data} = 0.640 ± 0.003
f_q^{data} = 0.360 ± 0.003
χ^2 / NDF = 614.0 / 24
anti-k$_T$ R=0.4 PF+CHS
468 < p$_{T,jet}$ < 507 GeV
f_g^{data} = 0.607 ± 0.003
f_q^{data} = 0.393 ± 0.003
f_g^{MC} = 0.631 ± 0.003
f_q^{MC} = 0.369 ± 0.003
f_g^{data} = 0.619 ± 0.002
f_q^{data} = 0.381 ± 0.002
χ^2 / NDF = 740.6 / 24
anti-k$_T$ R=0.4 PF+CHS
507 < p$_{T,jet}$ < 548 GeV
f_g^{data} = 0.592 ± 0.003
f_q^{data} = 0.408 ± 0.003
f_g^{MC} = 0.612 ± 0.003
f_q^{MC} = 0.388 ± 0.003
f_g^{data} = 0.595 ± 0.003
f_q^{data} = 0.405 ± 0.003
χ^2 / NDF = 473.1 / 24
anti-k$_T$ R=0.4 PF+CHS
548 < p$_{T,jet}$ < 592 GeV
f_g^{data} = 0.572 ± 0.003
f_q^{data} = 0.428 ± 0.003
f_g^{MC} = 0.594 ± 0.003
f_q^{MC} = 0.406 ± 0.003
f_g^{data} = 0.576 ± 0.001
f_q^{data} = 0.424 ± 0.001
χ^2 / NDF = 3665.9 / 24
anti-k$_T$ R=0.4 PF+CHS
592 < p$_{T,jet}$ < 638 GeV
f_g^{data} = 0.556 ± 0.004
f_q^{data} = 0.444 ± 0.004
f_g^{MC} = 0.578 ± 0.003
f_q^{MC} = 0.422 ± 0.003
f_g^{data} = 0.538 ± 0.001
f_q^{data} = 0.462 ± 0.001
χ^2 / NDF = 2012.5 / 24
anti-k$_T$ R=0.4 PF+CHS
638 < p$_{T,jet}$ < 686 GeV
f_g^{data} = 0.537 ± 0.003
f_q^{data} = 0.463 ± 0.003
f_g^{MC} = 0.562 ± 0.003
f_q^{MC} = 0.438 ± 0.003
f_g^{data} = 0.520 ± 0.002
f_q^{data} = 0.480 ± 0.002
χ^2 / NDF = 989.6 / 24
anti-k$_T$ R=0.4 PF+CHS
686 < p$_{T,jet}$ < 737 GeV
f_g^{data} = 0.520 ± 0.003
f_q^{data} = 0.480 ± 0.003
f_g^{MC} = 0.544 ± 0.003
f_q^{MC} = 0.456 ± 0.003
f_g^{data} = 0.502 ± 0.002
f_q^{data} = 0.498 ± 0.002
χ^2 / NDF = 1098.8 / 24
anti-k$_T$ R=0.4 PF+CHS
737 < p$_{T,jet}$ < 790 GeV
f_g^{data} = 0.504 ± 0.004
f_q^{data} = 0.496 ± 0.004
f_g^{MC} = 0.527 ± 0.003
f_q^{MC} = 0.473 ± 0.003
f_g^{data} = 0.477 ± 0.003
f_q^{data} = 0.523 ± 0.003
χ^2 / NDF = 668.2 / 24
anti-k$_T$ R=0.4 PF+CHS
790 < p$_{T,jet}$ < 846 GeV
f_g^{data} = 0.485 ± 0.004
f_q^{data} = 0.515 ± 0.004
f_g^{MC} = 0.513 ± 0.004
f_q^{MC} = 0.487 ± 0.004
f_g^{data} = 0.442 ± 0.003
f_q^{data} = 0.558 ± 0.003
χ^2 / NDF = 338.9 / 24
anti-k$_T$ R=0.4 PF+CHS
846 < p$_{T,jet}$ < 905 GeV
f_g^{data} = 0.466 ± 0.004
f_q^{data} = 0.534 ± 0.004
f_g^{MC} = 0.492 ± 0.004
f_q^{MC} = 0.508 ± 0.004
f_g^{data} = 0.438 ± 0.004
f_q^{data} = 0.562 ± 0.004
χ^2 / NDF = 257.7 / 24
anti-k$_T$ R=0.4 PF+CHS
905 < p$_{T,jet}$ < 967 GeV
f_g^{data} = 0.448 ± 0.004
f_q^{data} = 0.552 ± 0.004
f_g^{MC} = 0.475 ± 0.004
f_q^{MC} = 0.525 ± 0.004
f_g^{data} = 0.402 ± 0.004
f_q^{data} = 0.598 ± 0.004
χ^2 / NDF = 136.6 / 24
anti-k$_T$ R=0.4 PF+CHS
967 < p$_{T,jet}$ < 1032 GeV
f_g^{data} = 0.426 ± 0.004
f_q^{data} = 0.574 ± 0.004
f_g^{MC} = 0.460 ± 0.004
f_q^{MC} = 0.540 ± 0.004
f_g^{data} = 0.377 ± 0.006
f_q^{data} = 0.623 ± 0.006
χ^2 / NDF = 96.2 / 24
anti-k$_T$ R=0.4 PF+CHS
1/σ dσ/dQGL
Quark-Gluon Likelihood


Template Fit, 2016, 36.3 fb^{-1} (13 TeV)
CMS
Work in Progress
Data
MC
Gluons (MC)
Quarks (MC)
1/σ dσ/dQGL
Quark-Gluon Likelihood
0.0 ≤ |y_jet| < 1.3
1032 < p_T,jet < 1101 GeV
f_g^pythia = 0.414 ± 0.004
f_g^herwig = 0.356 ± 0.007
f_q^pythia = 0.586 ± 0.004
f_q^herwig = 0.644 ± 0.007
f_g^pythia = 0.437 ± 0.004
χ² / NDF = 61.4 / 24
f_g^gen = 0.563 ± 0.004
anti-k_T R=0.4 PF+CHS
1101 < p_T,jet < 1172 GeV
f_g^pythia = 0.393 ± 0.005
f_g^herwig = 0.365 ± 0.008
f_q^pythia = 0.607 ± 0.005
f_q^herwig = 0.635 ± 0.008
f_g^pythia = 0.419 ± 0.005
χ² / NDF = 49.0 / 24
f_g^gen = 0.581 ± 0.005
anti-k_T R=0.4 PF+CHS
1172 < p_T,jet < 1248 GeV
f_g^pythia = 0.371 ± 0.005
f_g^herwig = 0.314 ± 0.010
f_q^pythia = 0.629 ± 0.005
f_q^herwig = 0.686 ± 0.010
f_g^pythia = 0.397 ± 0.005
χ² / NDF = 40.8 / 24
f_g^gen = 0.603 ± 0.005
anti-k_T R=0.4 PF+CHS
1248 < p_T,jet < 1327 GeV
f_g^pythia = 0.352 ± 0.005
f_g^herwig = 0.278 ± 0.012
f_q^pythia = 0.648 ± 0.005
f_q^herwig = 0.722 ± 0.012
f_g^pythia = 0.386 ± 0.005
χ² / NDF = 30.4 / 24
f_g^gen = 0.614 ± 0.005
anti-k_T R=0.4 PF+CHS
1327 < p_T,jet < 1410 GeV
f_g^pythia = 0.341 ± 0.006
f_g^herwig = 0.281 ± 0.015
f_q^pythia = 0.659 ± 0.006
f_q^herwig = 0.719 ± 0.015
f_g^pythia = 0.366 ± 0.005
χ² / NDF = 28.2 / 24
f_g^gen = 0.634 ± 0.005
anti-k_T R=0.4 PF+CHS
1410 < p_T,jet < 1497 GeV
f_g^pythia = 0.325 ± 0.006
f_g^herwig = 0.263 ± 0.018
f_q^pythia = 0.675 ± 0.006
f_q^herwig = 0.737 ± 0.018
f_g^pythia = 0.351 ± 0.006
χ² / NDF = 38.9 / 24
f_g^gen = 0.649 ± 0.006
anti-k_T R=0.4 PF+CHS
1497 < p_T,jet < 1588 GeV
f_g^pythia = 0.303 ± 0.006
f_g^herwig = 0.201 ± 0.022
f_q^pythia = 0.697 ± 0.006
f_q^herwig = 0.799 ± 0.022
f_g^pythia = 0.332 ± 0.006
χ² / NDF = 26.2 / 24
f_g^gen = 0.668 ± 0.006
anti-k_T R=0.4 PF+CHS
1588 < p_T,jet < 1684 GeV
f_g^pythia = 0.286 ± 0.007
f_g^herwig = 0.163 ± 0.028
f_q^pythia = 0.714 ± 0.007
f_q^herwig = 0.837 ± 0.028
f_g^pythia = 0.312 ± 0.007
χ² / NDF = 30.5 / 24
f_g^gen = 0.688 ± 0.007
anti-k_T R=0.4 PF+CHS
1684 < p_T,jet < 1784 GeV
f_g^pythia = 0.264 ± 0.007
f_g^herwig = 0.187 ± 0.033
f_q^pythia = 0.736 ± 0.007
f_q^herwig = 0.813 ± 0.033
f_g^pythia = 0.291 ± 0.007
χ² / NDF = 32.0 / 24
f_g^gen = 0.709 ± 0.007
anti-k_T R=0.4 PF+CHS
1784 < p_T,jet < 1890 GeV
f_g^pythia = 0.248 ± 0.008
f_g^herwig = 0.139 ± 0.041
f_q^pythia = 0.752 ± 0.008
f_q^herwig = 0.861 ± 0.041
f_g^pythia = 0.279 ± 0.008
χ² / NDF = 31.1 / 24
f_g^gen = 0.721 ± 0.008
anti-k_T R=0.4 PF+CHS
1890 < p_T,jet < 2000 GeV
f_g^pythia = 0.240 ± 0.009
f_g^herwig = 0.159 ± 0.053
f_q^pythia = 0.760 ± 0.009
f_q^herwig = 0.841 ± 0.053
f_g^pythia = 0.264 ± 0.009
χ² / NDF = 51.4 / 24
f_g^gen = 0.736 ± 0.009
anti-k_T R=0.4 PF+CHS
2000 < p_T,jet < 2116 GeV
f_g^pythia = 0.225 ± 0.010
f_g^herwig = 0.140 ± 0.058
f_q^pythia = 0.775 ± 0.010
f_q^herwig = 0.860 ± 0.058
f_g^pythia = 0.247 ± 0.009
χ² / NDF = 59.5 / 24
f_g^gen = 0.753 ± 0.009
anti-k_T R=0.4 PF+CHS
2116 < p_T,jet < 2238 GeV
f_g^pythia = 0.209 ± 0.011
f_g^herwig = -0.070 ± 0.071
f_q^pythia = 0.791 ± 0.011
f_q^herwig = 1.070 ± 0.071
f_g^pythia = 0.230 ± 0.011
χ² / NDF = 23.8 / 23
f_g^gen = 0.770 ± 0.011
anti-k_T R=0.4 PF+CHS
2238 < p_T,jet < 2366 GeV
f_g^pythia = 0.204 ± 0.012
f_g^herwig = 0.026 ± 0.104
f_q^pythia = 0.796 ± 0.012
f_q^herwig = 0.974 ± 0.104
f_g^pythia = 0.226 ± 0.013
χ² / NDF = 19.3 / 20
f_g^gen = 0.774 ± 0.013
anti-k_T R=0.4 PF+CHS
2366 < p_T,jet < 2500 GeV
f_g^pythia = 0.175 ± 0.014
f_g^herwig = -0.044 ± 0.100
f_q^pythia = 0.825 ± 0.014
f_q^herwig = 1.044 ± 0.100
f_g^pythia = 0.198 ± 0.013
χ² / NDF = 17.7 / 18
f_g^gen = 0.802 ± 0.013
anti-k_T R=0.4 PF+CHS

8.6. Template Fit with Uncertainties




Template Fit, 2016, 36.3 fb^{-1} (13 TeV)
CMS
Work in Progress
Data
MC
Sys Unc
Fit
0.0 ≤ |y$_{jet}$| < 1.3
330 < p$_{T,jet}$ < 362 GeV
362 < p$_{T,jet}$ < 395 GeV
395 < p$_{T,jet}$ < 430 GeV
430 < p$_{T,jet}$ < 468 GeV
468 < p$_{T,jet}$ < 507 GeV
507 < p$_{T,jet}$ < 548 GeV
548 < p$_{T,jet}$ < 592 GeV
592 < p$_{T,jet}$ < 638 GeV
638 < p$_{T,jet}$ < 686 GeV
686 < p$_{T,jet}$ < 737 GeV
737 < p$_{T,jet}$ < 790 GeV
790 < p$_{T,jet}$ < 846 GeV
846 < p$_{T,jet}$ < 905 GeV
905 < p$_{T,jet}$ < 967 GeV
967 < p$_{T,jet}$ < 1032 GeV
anti-k$_T$ R=0.4 PF+CHS
1/σ dσ/dQGL
Quark-Gluon Likelihood


Template Fit, 2016, 36.3 fb^{-1} (13 TeV)
CMS
Work in Progress
Data
MC
Sys Unc
Fit
0.0 ≤ |y_jet| < 1.3
1032 < p_T,jet < 1101 GeV
1101 < p_T,jet < 1172 GeV
1172 < p_T,jet < 1248 GeV
1248 < p_T,jet < 1327 GeV
1327 < p_T,jet < 1410 GeV
1410 < p_T,jet < 1497 GeV
1497 < p_T,jet < 1588 GeV
1588 < p_T,jet < 1684 GeV
1684 < p_T,jet < 1784 GeV
1784 < p_T,jet < 1890 GeV
1890 < p_T,jet < 2000 GeV
2000 < p_T,jet < 2116 GeV
2116 < p_T,jet < 2238 GeV
2238 < p_T,jet < 2366 GeV
2366 < p_T,jet < 2500 GeV
anti-k_T R=0.4 PF+CHS
1/σ dσ/dQGL
Quark-Gluon Likelihood

Curriculum Vitae

İSMAİL OKAN ATAKİŞİ

Education:

- Marmara University Istanbul/Turkey(2015-2023)

Ph.D. student at High Energy and Particle Physics

- Kafkas University Graduate School of Natural and Applied Science Kars/Turkey

Master Student at High Energy and Particle Physics (2011-2014)

- Marmara University Istanbul/Turkey

Undergraduate Student at the Faculty of Arts and Sciences Physics (2005-2010)

- Marmara University School of Foreign Language Istanbul/Turkey

English preparatory school (2004-05)

Languages:

- Turkish Native Language
- English Advanced level

Computer Skills:

- C++
- ROOT
- Shell
- Python
- Geant4
- Mathematica
- CMSSW
- TensorFlow &Scikit Learn

School and Workshops Attended:

- 6th Yearly SMP-HAD Workshop, 11 Feb 2021, "Inclusive gluon jet" (presenter)¶
- CMS Data Analysis School Hamburg 2016
- Workshop MPGD Applications Beyond Fundamental Science Aveiro Portugal 2016
- HIZAL Workshop İstanbul (Marmara & Boğaziçi Üniversitesi) 2016
- Accelerator and Computer Application at High Energy Physics HPFBU-2012

Experience :

- Co-convener JetMET DQM&Validation for 3 years from 2018 to 2021
- Quartz Cherenkov Detectors studies for the FCD (old Totem) (2019)
- HF phase 1 upgrade at CERN both detector construction and test beam measurements.
- Member of JetMET trigger (JME HLT) 2016-2017
- Prof. Dr. M. Iori's laboratory at Rome La Sapienza University. 2012-2013

Scholarships:

- Visiting scientist, University of Helsinki (HIP) 2019-2019
- Scholar, Turkish Atomic Energy Authority (TAEK) 2015-2019.
- Scholar, Erasmus Student Mobility. University of Rome La Sapienza /Italy (Master Thesis) 2012-2013.

Projects:

- Autumatization of JetMet DQM for offline Data certification with ML
- Measurement of the inclusive gluon jet cross-section
- JetMET DQM DC/Validation and DQM Code maintaince
- HLT Trigger Performance Group.

- HF Phase 1 Upgradeof Qie-10 cards.
- (MSc) Investigation and Calibration SIPM Gain for Outside Astroparticle Detectors (master thesis):
- (MSc) Cosmic-ray flux and its Zenith Angle Dependencies at Region of Kars/Turkey:

Publications:

Selected publications:

- "Measurement and QCD analysis of double-differential inclusive jet cross" sections in proton-proton collisions at $\sqrt{s}$ = 13 TeV, JHEP 12 (2022)035
- "Performance of the CMS Jets and Missing Transverse Energy Trigger at LHC Run2" PoS ICHEP-2016/756 2017
- "Radioactive source calibration test of the CMS Hadron Endcap Calorimeter test wedge with Phase I upgrade electronics" Journal of Instrumentation(JINST) 12/12034 2017
- "SiPM application for a detector for UHE neutrinos tested at Sphinx station" Elsevier, Nuclear Inst. and Methods in Physics Research, A, http://dx.doi.org/10.1016/j.nima.2013.11.076
- "Measurement of Cosmic-ray flux at Region of Kars/Turkey" Turkish Physical Society 30'th International Physical Congress abstract book, page 204
- "Investigation and Calibration SIPM Gain for Outside Astroparticle Detectors" Turkish Physical Society 30'th International Physical Congress abstract book, page 205

Other publications:

- https://inspirehep.net/authors/1639175

Conference and Presentation:

- 3rd International Turkey-Iran Joint Conference on LHC Physics Istanbul 2019:" A study of Quartz Cherenkov Detectors in the Forward Region of CMS at LHC".co-writer.
- Roma International Conference on Astroparticle Physics(Ricap-13); SiPM application for a detector for UHE neutrinos tested at Sphinx Station as a co-writer.
- Turkish Physical Society 30'th International Physical Congress (TFD30);
  •(speaker) Investigation and Calibration SIPM Gain for Outside Astroparticle Detectors
  • Co-Writer of Cosmic-ray flux at Region of Kars/Turkey